Università degli Studi di Modena e Reggio Emilia

Dipartimento di Ingegneria "Enzo Ferrari"
Dottorato di Ricerca in Ingegneria Industriale e del Territorio
"Enzo Ferrari" - XXXII ciclo

Tesi di Dottorato
in Fisica Tecnica Industriale

Numerical studies of turbulent flows in mixed and natural convection regimes

Andrea Fregni

Relatore:
Chiar.mo Prof. Enrico Stalio

Coordinatore del Corso:
Prof. Paolo Tartarini

Anno accademico 2018/2019

a Giulia

That's how we know we're alive: we're wrong.

Philip Roth, *American Pastoral*

Ringraziamenti

I apologise to non-Italian speakers, acknowledgements are written in Italian. I am not good in writing non-technical texts and I will probably sound silly anyway.

Vorrei ringraziare tutti coloro che mi hanno aiutato, dentro e fuori l' Università, durante questo percorso triennale. Il professor Enrico Stalio, il mio tutor, si merita sicuramente il più sentito ringraziamento, maestri come lui sono rari da trovare e lavorare assieme è stato divertente e proficuo al tempo stesso. Grazie anche ai ricercatori Andrea Cimarelli e Diego Angeli, la loro passione per la ricerca è contagiosa e mettono un'energia invidiabile nel "fare scuola". E che dire del resto del gruppo LIFT? Di Marco, Levo, Betta, Roberto, Pietro, Adriano e Federica? Penso che siamo il gruppo di ricerca più eterogeneo che ci sia, ma siamo diventati ogni giorno più coesi. Grazie, mi avete insegnato tanto.

Ringrazio anche i ragazzi di Nottingham, Anna, Anahita e Marco, nonostante ci siamo conosciuti solo per poche settimane mi hanno fatto sentire parte della loro compagine fin da subito, accogliendomi come mai avevo sperimentato prima.

Sono grato anche alla mia famiglia e in particolar modo a mia madre e mio fratello, nonostante le differenze sono sempre stati presenti. Indispensabile è stata anche e soprattutto l'altra mia famiglia, quella dei "Ravaregaz", in particolar modo negli ultimi anni. Mi sento legato a doppio filo con loro e ai miei occhi sono i migliori insegnanti e compagni di vita. Grazie anche a Tommi, sempre pronto a condividere come me esperienze e ragionamenti sui più disparati temi, ai ragazzi della Formula e al gruppo degli "ingegneri" (per fortuna non solo tali), abbiamo condiviso esperienze e momenti che non dimenticherò.

Infine vorrei ringraziare colei cui questo lavoro è dedicato. Il suo amore e la sua cura sono stati fondamentali durante questo periodo, non riesco ad immaginare un affetto più intenso di quello che mi ha fatto provare.

Abstract

The aim of this work is to investigate turbulent flows and heat transfer phenomena where buoyancy forces are non-negligible. The studies are conducted by means of Direct Numerical Simulations performed in two configurations: a wall-bounded buoyancy-driven flow and a free-shear buoyancy-aided case. Calculations are conducted using a customised version of the open source code *Incompact3d* , where modifications include the addition of the Boussinesq's buoyancy term in the momentum equations and the implementation of an open outflow boundary condition suitable for buoyant and turbulent flows. In the text each novel implementation is presented together with a validation test.

Firstly buoyancy-driven convection is investigated in the Rayleigh-Bénard cell employing different fluids: mercury ($Pr = 0.025$), air ($Pr = 0.7$) and water ($Pr = 7$). Instead of the usual approach, where the Prandtl number is varied in constant-Rayleigh-number conditions, the three simulations are performed at constant Grashof number, $Gr = Ra/Pr = 5 \times 10^7$. This procedure allows the study of the Prandtl number influence while maintaining a constant ratio between the advective and diffusive terms in the momentum equations. The analysis of customarily and specifically developed statistics sheds light on the small-scale fluctuations and large-scale motions which are responsible for the energy transfer at different Prandtl numbers. Secondly, a non-canonical configuration which involves three planar jets vertically entering a pool at different temperature is studied. Beside the theoretical interest, this research is motivated by the study of temperature fluctuations induced by fuel rods cooling inside Liquid Metal Fast Reactors (LMFRs), which employ a liquid metal as coolant. This phenomenon is called *thermal striping* and might induce thermal-fatigue failures in the containment vessels. In order to infer about thermal striping the Prandtl number of Lead-Bismuth Eutectic at 220° C, *i.e.* a typical envisaged condition in LMFRs, is considered, $Pr = 0.031$. Reynolds number is set to $Re = 5000$ and the mixed convection regime is established at a Richardson number $Ri = 0.25$. Results show that jets undergo an intense mixing close to their inlets, while at distances larger than ten times the jets width they are coalesced in a single and almost isothermal stream. Here the flow displays some of the self-similar properties observed in canonical planar jets. An original formulation of the Coandă effect reveals the mechanism underlying jets coalescence. Finally, fields of turbulent viscosity and diffusivity, as well as kinetic and thermal dissipations, show behaviours which are unlikely to be reproduced by typical eddy-viscosity turbulence models.

In summary this study provides an original insight into the physics of turbulent heat transfer in wall-bounded and free-shear configurations where buoyancy forces are non-negligible. Results reported in this text might also be used for the development and validation of turbulence models to be employed in buoyant flows.

Sommario in lingua italiana

In questo testo è riportato uno studio degli aspetti termo-fluidodinamici di flussi turbolenti in regime di convezione naturale e mista. La ricerca è stata condotta mediante simulazioni numeriche ai principi primi eseguite in un flusso indotto dalle forze di galleggiamento tra due lastre piane e in uno caratterizzato da tre getti a diversa temperatura. I calcoli sono stati eseguiti impiegando una versione modificata del codice *open source Incompact3d* , dove le modifiche apportate prevedono l'introduzione del termine di galleggiamento secondo le ipotesi di Boussinesq e l'implementazione di una condizione al contorno di deflusso. Assieme alle modifiche apportate al codice vengono presentate le prove atte a validare le modifiche stesse.

La prima parte del testo riporta lo studio del moto all'interno della cella di Rayleigh-Bénard considerando diversi fluidi: mercurio ($Pr = 0.025$), aria ($Pr = 0.7$) ed acqua ($Pr = 7$). Invece di variare il numero Prandtl mantenendo costante il numero di Rayleigh, come spesso riscontrato in letteratura, le tre simulazioni vengono eseguite a pari numero di Grashof, $Gr = Ra/Pr = 5 \times 10^7$. Questo approccio permette lo studio dell'influenza del numero di Prandtl conservando un rapporto costante tra il termine advettivo e diffusivo nelle equazioni di bilancio della quantità di moto. Attraverso l'analisi delle consuete statistiche e di altre sviluppate appositamente per questo studio vengono caratterizzate le strutture di piccola e grande scala responsabili del trasporto di calore. In secondo luogo viene analizzata una configurazione composta da tre getti a diversa temperatura che sfociano all'interno di una piscina a forma di parallelepipedo. Oltre all'importanza in ambito di ricerca di base, questo flusso permette di indagare le fluttuazioni di temperatura indotte dal raffreddamento delle barre di combustibile all'interno di reattori nucleari che impiegano un metallo liquido come refrigerante, i cosiddetti *Liquid Metal Fast Reactors.* Il fenomeno descritto viene chiamato *thermal striping* e può provocare cedimenti per fatica termica nelle strutture di contenimento. Al fine di analizzare il *thermal striping* il numero di Prandtl scelto per la simulazione è $Pr = 0.031$, caratteristico della lega eutettica piombo-bismuto a 220° C, una tipica condizione prevista per questo tipo di reattori. Il numero di Reynolds del flusso vale $Re = 5000$ e l'intensità del

regime di convezione mista è data dal numero Richardson $Ri = 0.25$. I risultati mostrano che i getti si mescolano vigorosamente in prossimità del loro ingresso, mentre più a valle sono uniti in un'unica colonna di fluido, essenzialmente isoterma. In questa regione il flusso mostra alcune delle caratteristiche universali osservate nella configurazione canonica dei getti turbolenti. Inoltre il fenomeno responsabile dell'unione dei getti, il cosiddetto "effetto Coandă", viene spiegato in maniera originale attraverso l'analisi dei flussi di quantità di moto. Infine, i campi di viscosità e diffusività termica turbolenta, assieme alla dissipazione di energia cinetica turbolenta e varianza di temperatura, mostrano andamenti difficilmente riproducibili mediante i tradizionali modelli di turbolenza basati sull'approccio *eddy-viscosity*.

Riassumendo, questo studio fornisce un punto di vista originale sui meccanismi di trasporto del calore in circostanze in cui le forze di galleggiamento non possono essere trascurate, sia in configurazioni caratterizzate dalla presenza di pareti che in configurazioni prive di superfici solide. I risultati riportati potrebbero inoltre essere impiegati per lo sviluppo e la validazione di modelli di turbolenza specifici.

Contents

Notation

Latin letters

ℓ	Jet width defined for single and purely mechanical jets
Gr	Grashof number
Nu	Nusselt number
Pe	Péclet number
Pr	Prandtl number
Ra	Rayleigh number
Re	Reynolds number
Re_τ	Reynolds number based on friction velocity
Re_s	shear Reynolds number
Ri	Richardson number
Sc	Schmidt number
div_π	Divergence of the horizontal velocity field in Rayleigh-Bénard configurations
g	magnitude of gravitational acceleration
g_i	i-nth component of gravitational acceleration
H	Jet width in triple jet configuration, cell height in Rayleigh-Bénard convection
K	Kurtosis (fourth-order moment of fluctuating variables)
L	Length
L_x, L_y, L_z	extension of the computational domain in x, y, z directions
n_x, n_y, n_z	number of computational nodes along x, y, z directions
$N_{BL,\theta}$	Number of computational nodes inside the thermal boundary layer
$N_{BL,u}$	Number of computational nodes inside the velocity boundary layer

p	Pressure
R	Root-mean-squared error
S	Skewness (third-order moment of fluctuating variables)
S_{ij}	Element of the strain rate tensor
T	Temperature
t	Temporal coordinate
U	Velocity scale of large scale circulation
u, v, w	Velocity components, written also as u_i, u_j for $i, j = 1, 2, 3$
U_0	Average centreline velocity at jet inlets
u_τ	Friction velocity
U_c	Centreline velocity
U_M	Convective velocity in one-dimensional advection equation
U_p	Phase velocity in one-dimensional advective diffusive equation
U_s	Advective velocity in one-dimensional advective diffusive equation
U_{ff}	Free-fall velocity
x, y, z	Cartesian coordinates, written also as x_i, x_j for $i, j = 1, 2, 3$
$\boldsymbol{x}$	Position vector
$\boldsymbol{n}$	Surface-normal unity vector

Greek letters

α	Thermal diffusivity
α_t	Turbulent thermal diffusivity
β	Thermal expansion coefficient
χ	Diffusion coefficient
$\Delta\tau$	Time period
$\Delta\theta$	Non-dimensional temperature difference
ΔT	Temperature difference
Δt	Time step
$\Delta x, \Delta y, \Delta z$	Grid spacing in direction x_i
δ	Channel half-height or Kronecker delta

δ_θ	Thermal boundary layer thickness
δ_u	Velocity boundary layer thickness
η	Length scale of turbulent motion
Γ	Aspect ratio of the computational domain in Rayleigh-Bénard convection
λ	Taylor scale
ν	Kinematic viscosity
ν_t	Turbulent kinematic viscosity
Ω_E	Extended domain
Ω_N	Regular-size domain
Ω_R	Restricted domain
ϕ	Generic flow variable, it indicates either a velocity component or temperature
ψ	Generic passive scalar
ρ	Density or autocorrelation coefficient
τ	Time scale of turbulent motion
θ	Non-dimensional temperature
θ_j	Average, centreline, non-dimensional temperature of the hot jet
$\tilde{\varepsilon_\theta}'$	Dissipation rate of temperature
$\tilde{\varepsilon}$	Pseudo-dissipation rate of turbulent kinetic energy
$\tilde{\varepsilon}'$	Pseudo-dissipation rate of kinetic energy
ε	Dissipation rate of turbulent kinetic energy
ε_θ	Dissipation rate of temperature variance
φ_j	j-nth component of momentum flux per unit volume

Subscripts

θ	Relative to the temperature field
B	Batchelor scale
b	At domain boundaries
c	Cold

h	Hot
i and j	i-nth or j-nth Cartesian component of a vector
K	Kolmogorov scale
min	Minimum
p	Relative to the pressure field
ref	Reference value
rms	Root-mean-square value or standard deviation
u, v, w	Relative to one of the velocity component
w	At walls

Superscripts

(n)	Current time step
$+$	Scaled over the smallest turbulence scales
0	Quantity in reference thermodynamic conditions
$*$	Dimensional quantity
$'$	Turbulent fluctuation unless otherwise stated
E	Extended domain
N	Regular domain

Other symbols (• is a placeholder)

$\tilde{\bullet}$	Used for locally defined scales, unless otherwise stated
$\langle \bullet \rangle$	Averaged value
$\langle \bullet \rangle_V$	Volume-averaged statistics

Introduction

Turbulent heat transfer in mixed and natural convection regime occurs whenever temperature differences in fluids are large enough to originate density gradients and thus non-negligible buoyancy forces. Such flows are observed in numerous environmental fluid motions of interest, think for example to air circulation in the atmosphere, natural streams in the oceans and convection on Sun's outer layer. Beside environmental flows, countless technological applications rely on buoyancy-driven or buoyancy-aided heat transfer. Passive cooling of nuclear reactors and electronic devices are just two examples.

The non-trivial coupling between velocity and temperature fields introduced by buoyancy has been mainly studied for fluids with order-one Prandtl number. Other fluids received less attention despite their importance in applications and environmental flows. To provide sensible advancements in this field only experiments and Direct Numerical Simulations (DNSs) seem to be suitable tools, as turbulence models could affect the simulated physical phenomena. However, laboratory measurements inherently interfere with the flow and when opaque fluids are employed, such as liquid metals, local and global velocity measures are problematic and require unconventional techniques (Schulenberg and Stieglitz, 2010). On the contrary, DNSs allow to obtain fully tridimensional fields of velocity and temperature with spatial and temporal resolutions able to represent all the scales of turbulent motions. As turbulence models are not employed in DNSs, simulation errors lie exclusively in the selection of a suitable set of governing equations, in the truncation errors of numerical schemes adopted and in the specific algorithm employed, *e.g.* the pressure-velocity coupling. These errors can be easily calculated making DNSs a research tool where the accuracy of results is well under control.

In the present thesis turbulent flows in mixed and natural convection regimes are studied in two configurations, a wall-bounded buoyancy-driven one and a free-shear buoyancy-aided flow. The former configuration is represented by the canonical Rayleigh-Bénard Convection (RBC), which is studied in a rectangular and laterally unbounded domain with aspect ratio $\Gamma = 8$ employing different working fluids: liquid mercury ($Pr = 0.025$), air ($Pr = 0.7$) and water ($Pr = 7$).

Instead of the usual approach, where Pr is varied while maintaining a constant Rayleigh number, simulations presented here are performed in constant-Grashof-number conditions $Gr = Ra/Pr = 5 \times 10^7$, therefore Ra and Pr are varied together. Such approach, firstly used by Schumacher et al. (2015), allows to study turbulent natural convection by varying the ratio between the convective and diffusive terms in the energy equation, while momentum equations are left unchanged, *i.e.* advective and viscous terms have the same relative magnitude. Secondly, a non-conventional configuration is employed to study free-shear flows in mixed convection regime. This involves three planar jets of liquid metal vertically-discharged in a pool from the bottom, where the jets have the same average velocity but different temperature and are symmetrically arranged as cold-hot-cold. Beside the theoretical interest in buoyancy-aided mixing phenomena, the study of triple jet configuration is motivated by its relevance in nuclear engineering applications (Kimura et al., 2007). Indeed in the upper plenum of Liquid Metal Fast Reactors (LMFRs), *i.e.* nuclear reactors which employ liquid metals as fuel-rods coolants with the aim to be inherently safe in case of electric power failures, hot and cold streams are mixed in conditions where buoyancy forces are non-negligible. As thermal diffusivity of liquid metals is extremely high, temperature fluctuations originated by the mixing are quickly transmitted to the containment structures potentially leading to failures due to thermal fatigue; this phenomenon is called “thermal striping” (Brunings, 1982). In order to infer about thermal striping, Prandtl number $Pr = 0.031$ is set, representing Lead-Bismuth Eutectic (LBE) at 220°, a typical envisaged coolant in LMFRs. Reynolds number based on jets centreline velocity and their width is $Re = 5000$, Grashof number is $Gr = 6.25 \times 10^6$. Therefore the mixed convection regime is established at a Richardson number $Ri = Gr/Re^2 = 0.25$.

Simulations presented are performed using two different modified versions of the open-source and highly-parallel code *Incompact3d* (Laizet and Lamballais, 2009; Laizet and Li, 2011). The native version of the code solves the incompressible Navier-Stokes equations together with a passive-scalar transport equation on Cartesian grids by using the finite difference formalism. Modifications introduced by the author feature the addition of the Boussinesq’s buoyancy term in the momentum equations, the implementation of an open outflow boundary condition and the development of an inflow strategy to set at jet inlets velocity and temperature profiles recorded from a precursor channel DNS. Besides, to perform calculations in the precursor channel configuration and in RBC at low Prandtl number, a semi-implicit version of *Incompact3d* developed by Flageul et al. (2015)

has been used. This implements an implicit strategy along y direction in order to help numerical stability in configurations where the Péclet number $Pe = Re\,Pr$ is small and stretched grids are employed in y direction. All the code versions and modifications implemented are presented in the text along with a validation test.

The present document is organised as follows. In chapter 1 the main features of *Incompact3d* are briefly presented along with the in-house modifications and validation tests. The addition of the buoyancy term is assessed by comparing results on a Rayleigh-Bénard configuration against reference data by Togni et al. (2015), while precursor channel statistics are compared with well-known benchmarks by Moser et al. (1999) and Kawamura et al. (1999). The implementation of the open outflow boundary condition is validated by comparing results on two triple jet configurations, where the vertical extension of one domain is two times larger than the base case. The study of RBC at different Prandtl number is presented in chapter 2. In section 2.3 the spatio-temporal discretisation of each simulation is carefully assessed and the validity of the Boussinesq's approximation is checked by using validity maps constructed with the method by Gray and Giorgini (1976). Results presented are compared with analyses reported in literature and allow to compare heat transfer features at different Prandtl numbers. Chapter 3 reports the investigations on the triple jet configuration where, again, discretisation and applicability of Boussinesq's hypotheses are described in detail. Results show that the flow can be divided in two different regions, one close to the inlets, where turbulent activity is promoted by shear-layer instabilities and buoyancy production, and one far from the inlets where jets are coalesced in single, isothermal stream which recovers some of the self-similar properties of purely mechanical jets. Concluding remarks are collected in the last chapter.

Finally, it is worth to notice that RBC calculations have been made possible thanks to a PRACE (Partnership for Advanced Computing in Europe) grant of 65 million core hours, while several ISCRA (Italian SuperComputing Resource Allocation) grants supported the triple jet simulation. Studies aimed at producing a high-fidelity numerical benchmark in the triple jet configuration have received funding from the Euratom programme under grant agreement No 654935, acronym "SESAME". The author acknowledges the above mentioned research programmes.

1 Code development and validation tests

In this chapter the code *Incompact3d* is presented together with modifications implemented by the author. These include the addition of the Boussinesq's buoyancy term in the momentum equations, the implementation of an open outflow boundary condition and the development of an inflow strategy which allows to set inlet conditions using profiles recorded from a precursor simulation. Besides, validation tests aimed at assessing the accuracy of new implementations are reported.

1.1 Incompact3d

Incompact3d is an open source code developed by Sylvain Laizet and Eric Lamballais (Laizet and Lamballais, 2009). It solves the incompressible Navier-Stokes equations and a passive scalar transport equation using a direct or large eddy approach to turbulence. Computations are performed on a Cartesian mesh and sixth-order compact schemes are used for spatial discretisation, see Lele (1992) for an extensive discussion about the topic. Time advancement is performed employing one of the following explicit schemes: second- and third-order Adams-Bashforth, third- and fourth-order Runge-Kutta. The set of equations numerically solved by the original version of *Incompact3d* reads

$$\begin{gathered}
\frac{\partial u_i}{\partial x_i} = 0 \\
\frac{\partial u_i}{\partial t} + u_j \frac{\partial u_i}{\partial x_j} = -\frac{\partial p}{\partial x_i} + \frac{1}{Re} \frac{\partial^2 u_i}{\partial x_j \partial x_j} \\
\frac{\partial \psi}{\partial t} + u_j \frac{\partial \psi}{\partial x_j} = \frac{1}{ScRe} \frac{\partial^2 \psi}{\partial x_j \partial x_j}
\end{gathered} \tag{1.1}$$

where subscripts $i, j = 1, 2, 3$. x_i stands for the spatial coordinates in a Cartesian reference frame $x_1 = x$, $x_2 = y$ and $x_3 = z$, as well as u_i indicates velocity components, $u_1 = u$, $u_2 = v$ and $u_3 = w$; p represents pressure and ψ is a passively transported scalar. Re and Sc are respectively the Reynolds and Schmidt numbers. When the scalar considered is temperature the Prandtl number substitutes the more general Schmidt number.

The main originality of *Incompact3d* lies in the enforcement of the incompressibility constraint, which is done using a projection method and hence requires to solve a Poisson problem for the pressure field. The Poisson equation is fully solved in the spectral space via the use of Fast Fourier Transforms regardless of boundary conditions. This is shown to reduce the accuracy of the numerical scheme for example in near-wall regions, where Dirichlet conditions are imposed. However, as reported in the validation test by Laizet and Lamballais (2009), truncation errors are smaller than second order even close to such boundaries. Another key feature of *Incompact3d* is its excellent scalability, as reported in Laizet and Li (2011). Parallelism is implemented by the domain decomposition technique implemented in the *2Decomp&fft* open source library, which divide the computational domain in 2D *pencils* alternatively along x, y and z directions.

1.2 Buoyancy

The implementation of buoyancy forces in *Incompact3d* is done following the Boussinesq's hypotheses, the validity of which is discussed later for each configuration studied, see sections 2.3 and 3.2. Boussinesq's approximation assumes that density is constant and equal to a reference value ρ^0 in each term of the governing equations except for the gravitational term in the momentum equations. There density is considered to vary linearly with temperature. All other fluid properties are considered constant, see Tritton (1988) and Gray and Giorgini (1976) for a thorough discussion about the Boussinesq's approximation.

Including the Boussinesq's buoyancy term the set of non-dimensional governing equations is the following

$$
\begin{gathered}
\frac{\partial u_i}{\partial x_i} = 0 \\
\frac{\partial u_i}{\partial t} + u_j \frac{\partial u_i}{\partial x_j} = -\frac{\partial p}{\partial x_i} + \frac{1}{Re} \frac{\partial^2 u_i}{\partial x_j \partial x_j} + \frac{Gr}{Re^2} \theta g_i \\
\frac{\partial \theta}{\partial t} + u_j \frac{\partial \theta}{\partial x_j} = \frac{1}{Pr Re} \frac{\partial^2 \theta}{\partial x_j \partial x_j}
\end{gathered}
\tag{1.2}
$$

where variables are made non-dimensional by selecting specific reference quantities: a velocity u_{ref}, a length l_{ref} and a temperature difference ΔT_{ref}. With respect to equations (1.1) the gravitational term $Gr/Re^2 \, \theta g_i$ has been added, where Gr is the Grashof number, θ stands for the non-dimensional temperature and g_i is the i-nth component of the gravitational acceleration.

The implementation of the buoyancy term in *Incompact3d* simply require the addition of the term $\theta g_i \, Gr/Re^2$ to the right-hand side of the momentum equations. Beside this modification also a subroutine to impose Dirichelet boundary condition for the temperature field has been introduced in the code.

1.2.1 Validation test

The implementation of the Boussinesq's buoyancy term in *Incompact3d* has been assessed by performing a DNS of Rayleigh-Bénard convection in a rectangular and laterally unbounded cell, see figure 1.1. For conciseness the description of the flow configuration is reported only in chapter 2. The comparison is performed by reproducing physical and numerical parameters of the simulation reported by Togni et al. (2015), which employ a pseudo-spectral code relying on a Fourier representation on horizontal planes and Chebyshev polynomials in the wall-normal direction.

The problem is made non-dimensional by selecting as reference quantities the free-fall velocity (see equation (2.2)), the height of the cell H and the temperature difference between the walls $\Delta T_{ref} = T_h - T_c$. Rayleigh and Prandtl numbers are set to $Ra = 1.7 \times 10^5$ and $Pr = 0.7$. The rectangular computational domain has dimensions $L_x \times L_y \times L_z = 8 \times 1 \times 8$ and the computational grid accounts for $n_x \times n_y \times n_z = 128 \times 129 \times 128$ points. The third-order Runge-Kutta scheme is used for time integration and a non-dimensional time step $\Delta t = 0.0005$ is adopted. In the horizontal directions, x and z, periodic boundary conditions are applied,

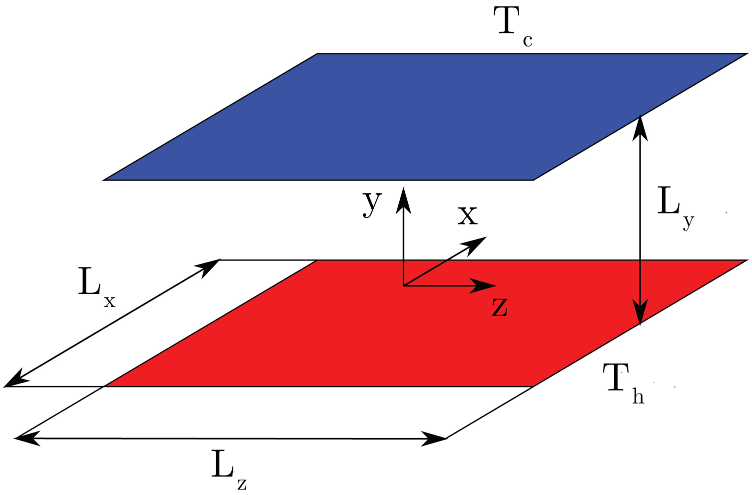

FIGURE 1.1: Sketch of the Rayleigh-Bénard cell considered.

while at the walls no-slip and constant temperature conditions are set respectively for the velocity and temperature field. The non-dimensional temperature of the bottom and top wall is respectively $\theta_h = 0.5$ and $\theta_c = -0.5$. The same numerical numerical parameters are employed in the reference simulation.

In figure 1.2 statistics computed using the modified version of *Incompact3d* are compared with reference data by Togni et al. (2015). To quantify errors on statistics presented the root-mean-square deviations between profiles are used. These are $R(\langle\theta\rangle) = 0.245\%$, $R(\theta_{\mathrm{rms}}) = 0.611\%$, $R(u_{\mathrm{rms}}) = 1.026\%$ and $R(v_{\mathrm{rms}}) = 0.522\%$ where relative errors are computed with respect to the maximum values. The comparison reported suggests that present results are not affected by implementation errors.

1.3 Open outflow boundary condition

To be resolvable a partial differential equations problem, such as the Navier-Stokes equations, require the definition of boundary conditions. In computational fluid dynamics boundary conditions for the velocity and temperature fields are specified at the domain boundaries. At boundaries where fluid may enter or leave the domain "open boundary" conditions have to be set. The aim of such conditions is to represent an unlimited space, as flows in reality are not bounded, through a limited computational domain. In particular when dealing with constant-density fluids the incompressibility constraint at permeable boundaries is difficult to meet because of the coupling between pressure and the velocity component normal to the boundary itself. This makes the definition of

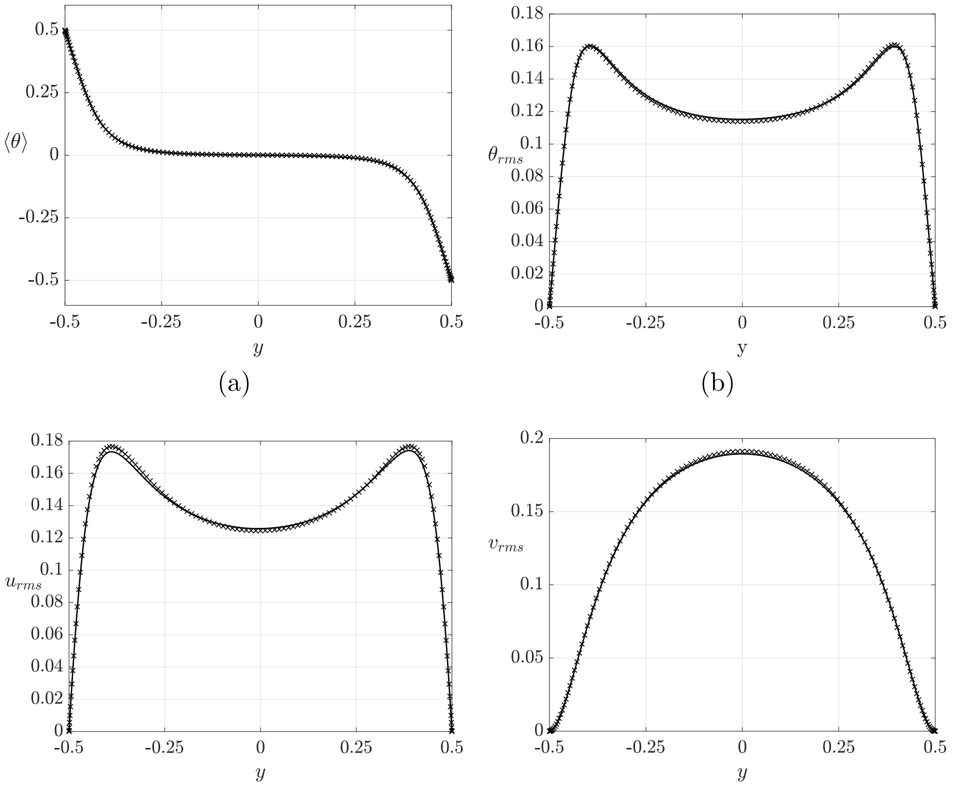

(a) (b) (c) (d)

FIGURE 1.2: Comparison of statistics in the Rayleigh-Bénard configuration used to validate the implementation of the buoyancy term: — present results, × reference data by Togni et al. (2015). (a) average temperature profile, (b) temperature fluctuations, (c) horizontal velocity fluctuations and (d) vertical velocity fluctuations.

open boundary conditions an “exercise in frustration” as defined by Sani and Gresho (1994) at the end of a symposium on that topic.

The outflow condition implemented in the original version of *Incompact3d* is one-dimensional convective equation along the direction normal to the outflow plane

$$\left.\frac{\partial u_i}{\partial t}\right|_b + U_M \left.\frac{\partial u_i}{\partial\left(\boldsymbol{x}\cdot\boldsymbol{n}\right)}\right|_b = 0 \tag{1.3}$$

In equation (1.3) U_M is a convective velocity computed as the mean value between the maximum and the minimum normal velocity on the boundary; $\boldsymbol{n}$ is the unit vector normal to the outflow boundary. Condition (1.3) has shown to be suitable in simulations where buoyancy forces are negligible or when passive scalars are not considered, see for example Gautier et al. (2014); Laizet et al. (2010); Lamballais et al. (2010). On the contrary in buoyant flow configurations it makes the solver algorithm unstable. For such type of flows Hattori et al. (2013) review the open outflow boundary conditions employed in literature and state that the most accurate one to deal with buoyant and turbulent flows is the condition proposed by Stevens (1990). This condition is based upon the following one-dimensional advection-diffusion equation defined at the outlet plane $x = L_x$

$$\frac{\partial \phi}{\partial t} + (U_p + U_s)\frac{\partial \phi}{\partial x} = \chi\frac{\partial^2 \phi}{\partial x^2} \tag{1.4}$$

where χ is the diffusion coefficient, *i.e.* kinematic viscosity ν or thermal diffusivity α, and the transport velocity is obtained by summing the advection velocity U_s to the phase velocity U_p, defined as

$$U_s \equiv \frac{u^{(n)}_{n_x} + u^{(n)}_{n_x-1}}{2}; \qquad U_p \equiv \frac{\phi^{(n)}_{n_x-1} - \phi^{(n-1)}_{n_x-1}}{\phi^{(n-1)}_{n_x-2} - \phi^{(n-1)}_{n_x-1}} \tag{1.5 a, b}$$

In equations (1.4) and (1.5) ϕ stands for a velocity component or temperature, n indicates the current time-step and n_x is the vertical grid index at which $x = L_x$. In addition, clipping is applied to the sum $U_p + U_s$ to ensure that $0 \leq U_p + U_s \leq U_0 + U_{ff}$, where U_0 is the average centreline velocity of jets and U_{ff} is the free-fall velocity, *i.e.* the velocity scale related to the buoyancy effect. In non-dimensional form $U_{ff} = Ri^{0.5}$.

1.3.1 Validation test

The outflow condition (1.4) is tested by comparing results obtained in two simulations on the triple jet configuration depicted in figure 1.3 (see chapter 3 for a more

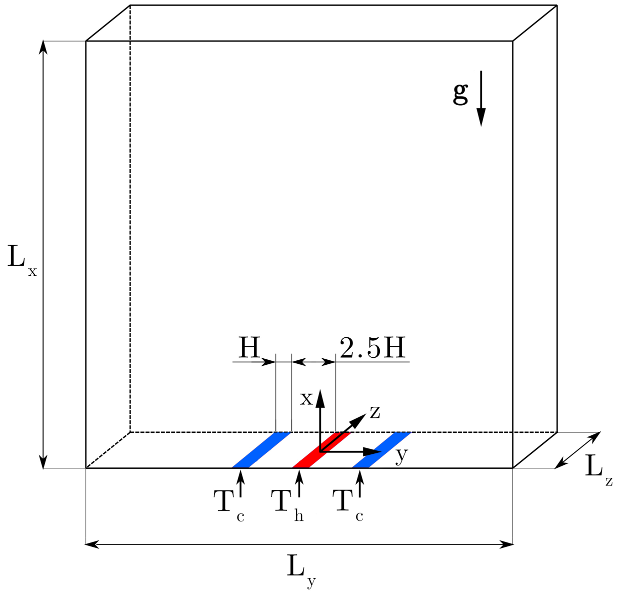

FIGURE 1.3: Sketch of the triple jet configuration.

extensive description of the flow), performed on computational domains of different vertical extension. The domain of regular size is $\Omega_N = [0, 30] \times [-15, 15] \times [0, 6]$ while the extended domain dimensions are $\Omega_E = [0, 60] \times [-15, 15] \times [0, 6]$. The two grids include $257 \times 256 \times 64$ and $513 \times 256 \times 64$ points, respectively, in order to maintain the same grid spacing. The physical case selected for the test is very close to the triple jet presented in section 3.2. In order to reduce the computational effort Reynolds number based on the jet width H is set to $Re = U_0\, H/\nu = 500$ instead of $Re = 5000$, while for simplicity velocity components and temperature at the jet inlets are specified using hyperbolic tangent profiles, as suggested by Stanley et al. (2002). For the central jet

$$\begin{aligned} u &= \frac{U_0}{2} + \frac{U_0}{2}\ \tanh\left[5\left(\frac{H}{2} - \sqrt{y^2}\right)\right] \\ \theta &= \frac{\theta_h}{2} + \frac{\theta_h}{2}\ \tanh\left[5\left(\frac{H}{2} - \sqrt{y^2}\right)\right] \end{aligned} \tag{1.6}$$

while cross-flow velocities are set to zero, $v = w = 0$. Temperature profiles of lateral jet are obtained by setting θ_c as the centreline temperature and substituting y by $y - 3.5H$ and $y + 3.5H$ for the right and left jet respectively.

Even at $Re = 500$ in both simulations the flow displays a turbulent behaviour. Figure 1.4 reports contours of percentage errors between statistics computed in the regular and extended computational domains. Errors are computed as

$$\frac{\left|\phi^N - \phi^E\right|}{\phi_{ref}} \times 100 \tag{1.7}$$

where ϕ is the statistic quantity considered and ϕ_{ref} is a reference value, U_0 for velocity-related statistics and $\Delta\theta$ for the average temperature field. As one may expect figure 1.4 shows that errors on statistics considered are larger close to the top and lateral boundaries. The only exception is u_{rms}.

Overall the errors introduced by the outflow condition on the regular domain Ω_N can be quantified by root-mean-square deviations of first-order statistics calculated in Ω_N with respect to statistics computed on the extended domain Ω_E taken as reference. Errors are defined similarly to the paper Hattori et al. (2013)

$$R(\phi) = \sqrt{\frac{\sum_{i,j}\left(\phi^N_{i,j} - \phi^E_{i,j}\right)^2}{N_{i,j}}} \tag{1.8}$$

In equation (1.8) the summation is performed only on indices i and j because statistics are obtained by averaging in time and along z-direction (k index). Table 1.1 shows deviations computed using equation 1.8 on domain $\Omega_N = [0,30] \times [-15,15] \times [0,6]$ and on the restricted portion $\Omega_R = [0,20] \times [-10,10] \times [0,6]$, see figure 1.5. This is in view of evaluating errors and locating regions where deviations induced by the vicinity of the outflow boundary are well under control. Results in table 1.1 should be read in comparison to the reference quantities: inlet velocity and temperatures ($U_0 = 1; \theta_h = 0.5; \theta_c = -0.25$) and the free-fall velocity $U_{ff} = 0.5$. It is apparent that deviations introduced by the outflow conditions are acceptable, especially when results in Ω_R are considered. As a consequence results in the triple jet simulation (section 3.4) are presented in the restricted sub-domain Ω_R.

1.4 Precursor channel

In order to set realistic inlet conditions at the jets entrance in the triple jet simulation a precursor simulation technique is employed. Inlet profiles of velocity components and temperature are specified using instantaneous bidimensional fields saved on a cross-flow plane in a DNS of a fully developed channel flow in which temperature is computed as a passive scalar. To match the flow regime in the triple jet configuration, the Reynolds number based on the channel height and

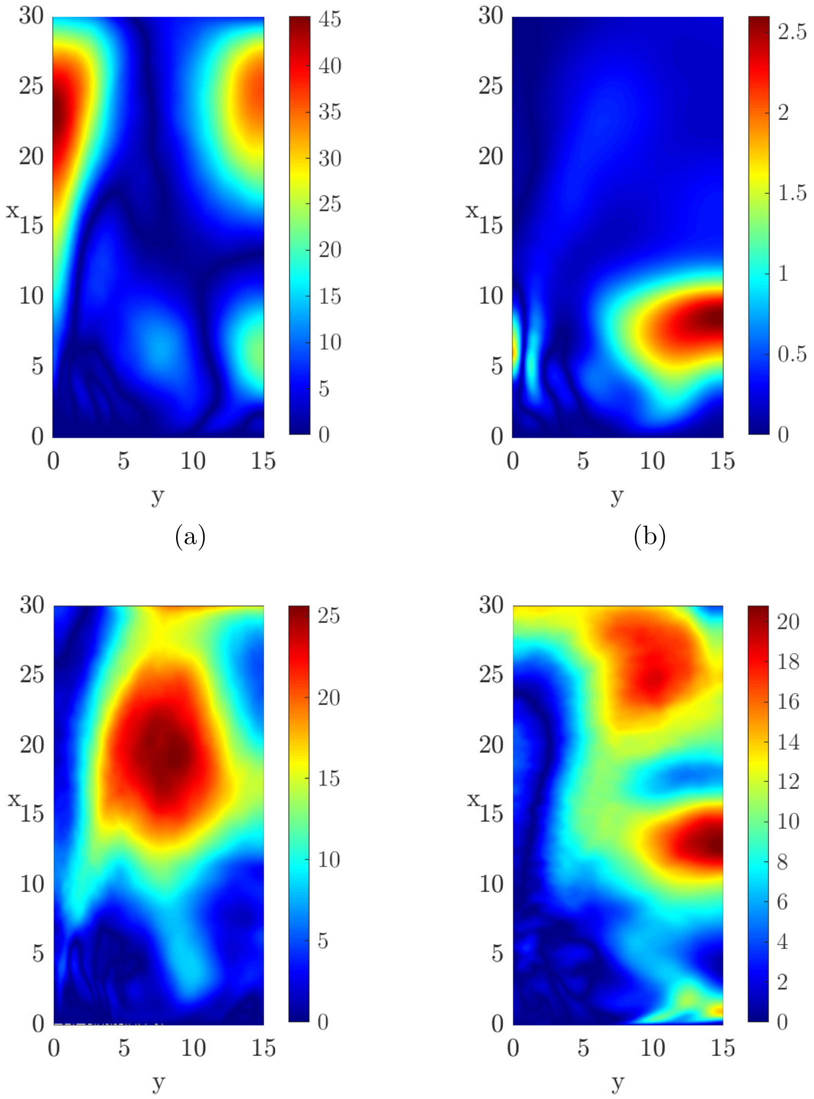

(a) (b)

(c) (d)

Figure 1.4: Contours of percentage errors defined by equation (1.7) on the fields of (a) average vertical velocity component, (b) average non-dimensional temperature, (c) and (d) root-mean-squared fluctuations of u and v respectively.

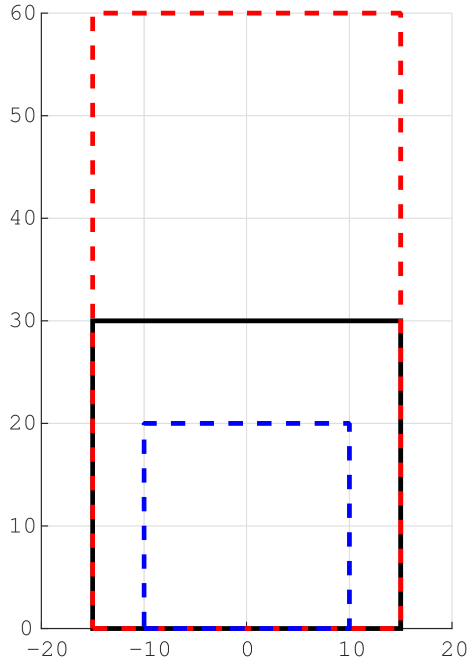

Figure 1.5: Two-dimensional domains on which statistics are defined. Black-solid square represents regular domain Ω_N, red-dashed rectangle indicates the extended domain Ω_E and blue-dashed square is the trace of Ω_R.

Domain	Ω_N	Ω_R
$R(\langle u \rangle)$	$8.43 \cdot 10^{-2}$	$4.77 \cdot 10^{-2}$
$R(\langle v \rangle)$	$6.67 \cdot 10^{-2}$	$5.85 \cdot 10^{-2}$
$R(\langle \theta \rangle)$	$3.97 \cdot 10^{-3}$	$3.27 \cdot 10^{-3}$
$R(u_{rms})$	$4.70 \cdot 10^{-2}$	$3.77 \cdot 10^{-2}$
$R(v_{rms})$	$4.07 \cdot 10^{-2}$	$1.75 \cdot 10^{-2}$
$R(w_{rms})$	$8.54 \cdot 10^{-3}$	$8.13 \cdot 10^{-3}$
$R(\theta_{rms})$	$1.65 \cdot 10^{-3}$	$1.58 \cdot 10^{-3}$

Table 1.1: Root-mean-square deviations used to compare results obtained in different domains. Errors are computed on statistics in two different sub-domains: Ω_N and Ω_R, considering solutions on Ω_E as reference.

the time averaged centreline velocity is set to $Re = 5000$, while Prandtl number is $Pr = 0.031$. The friction Reynolds number computed *a posteriori*, based on the channel half-height δ, is $Re_\tau = u_\tau \delta/\nu = 141$, falling in the weakly turbulent regime.

The computational domain dimensions are $L_x \times L_y \times L_z = 2\pi \times 1 \times 6$ and computations are performed on $256 \times 129 \times 256$ grid points, respectively in the streamwise x, wall-normal y and spanwise z direction. Boundary conditions impose periodicity along x and z directions, while at y-normal walls no-slip and constant heat flux conditions are applied. To simulate a fully-developed flow and thus apply periodic conditions in the streamwise direction the fluid excess temperature formalism is employed, see Kawamura et al. (1999). The computational time-step is the same of the triple jet simulation, $\Delta t = 0.0005$. It is worth to notice that to employ such time step the semi-implicit version of *Incompact3d* developed by Flageul et al. (2015) [1], in which the diffusive terms in y direction are treated implicitly, has been used. If the above-mentioned numerical parameters are set in the native and fully explicit version of *Incompact3d* the code will become unstable due to low Prandtl number considered and the grid spacing employed in proximity of walls.

In figure 1.6 statistics computed in the precursor channel simulation ($Re_\tau = 141$, $Pr = 0.031$) are compared against reference data by Moser et al. (1999) and Kawamura et al. (1999), obtained at $Re_\tau = 180$ and $Pr = 0.025$. Present results agree well with reference data, despite the small difference in Reynolds and Prandtl numbers.

---

[1] https://framagit.org/CFLAG/incompact3d

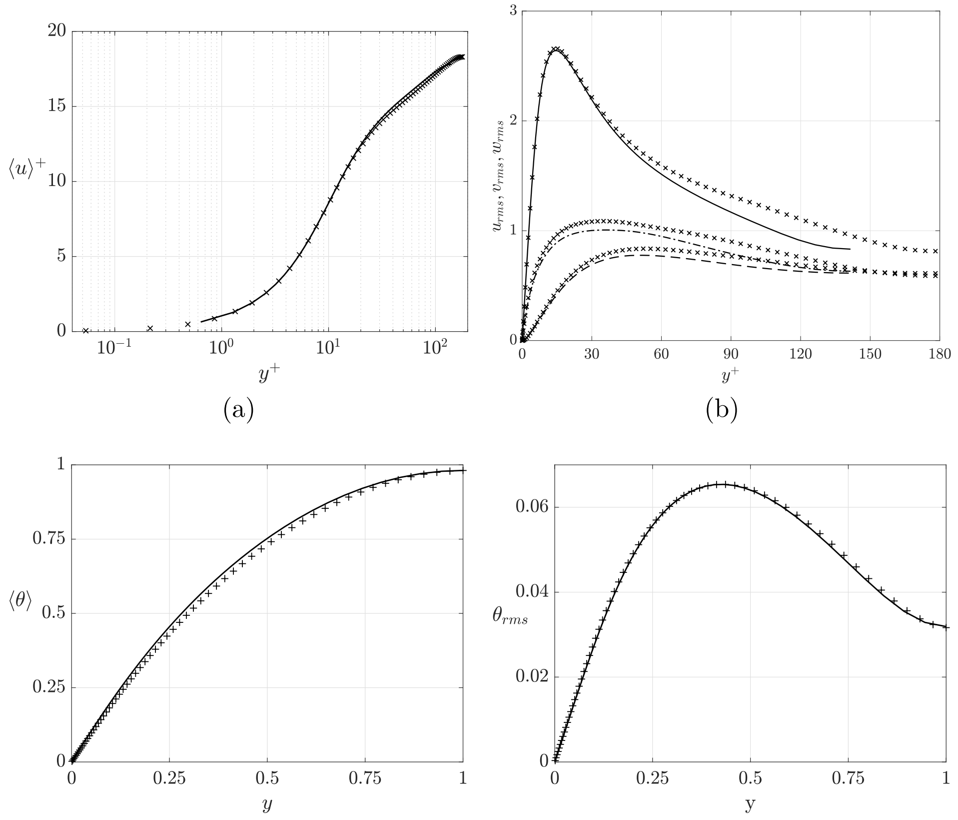

(a) (b)

(c) (d)

FIGURE 1.6: Comparison of precursor channel statistics obtained with *Incompact3d* at $Re_\tau = 141$ and $Pr = 0.031$ (lines) with reference data: Moser et al. (1999) ($Re_\tau = 180$, symbol ×) and Kawamura et al. (1999) ($Pr = 0.025$, symbol +). (a) average velocity and (b) velocity components fluctuations: u(——), v(−−) and w (− · −) in viscous units; (c) average temperature and (d) temperature fluctuations.

2 Rayleigh-Bénard convection

2.1 Introduction

Turbulent natural convection is observed in countless flows in Nature as well as in several engineering applications. Circulations in the oceans, air atmospheric cycle and overturning of liquid metal in Earth's outer core are just few examples of environmental fluid motions induced by density differences due to temperature gradients, see for example Marshall and Schott (1999), Hartmann et al. (2001) and Larson (1991). Outside the atmosphere thermally-driven turbulence occurs in the outer layer of the Sun (Nordlund et al., 2009) and other stars (Michel et al., 2008), while in the technological field it plays a prominent role in passengers cabins and buildings thermal comfort of (Wang et al., 2014), and also in the passive cooling of nuclear reactors (Ortiz et al., 2019).

Although natural convection occurs is a wide variety of flows its essential features are reproduced in the Rayleigh-Bénard configuration (Normand et al., 1977), which is essentially made by a confined fluid layer heated from below and cooled from above. Rayleigh-Bénard Convection (RBC) has been and is the subject of several studies, as proven by the following three extensive reviews: Ahlers et al. (2009), Lohse and Xia (2010) and Chillà and Schumacher (2012). As reported by Xia (2013) four main trends are followed in the study of turbulent RBC. The most important one is related to the scaling of the Nusselt (Nu) number, *i.e.* the non-dimensional parameter that quantifies heat-transfer enhancement with respect to a purely conductive layer, with parameters that regulate the flow regime, Rayleigh (Ra) and Prandtl (Pr) numbers. In this field the main advancements have been provided by Grossmann and Lohse (2000) and their subsequent works (Grossmann and Lohse, 2001, 2002, 2004), who proposed scaling laws $Nu = f(Ra, Pr)$ which have been found to predict, within a good approximation, the Nusselt number for a wide range of Ra and Pr. The second trend in RBC studies is the influence of buoyancy forces on statistical properties of turbulent flows, *i.e.* the occurrence of the Bolgiano-Obukhov cascade instead of the Kolmogorov one in a certain range of scales of the energy spectrum, see Bolgiano (1959) and Obukhov (1959). As reported for example by Calzavarini et al. (2002), Kunnen et al. (2008) and Sun et al. (2006) the observation of the Bolgiano-Obukhov scaling is still an open question. The last two topics of interest concern boundary layer dynamics and coherent structures and the way they affect the mechanics of heat and momentum transfers, being these fundamentals to develop accurate transport models. A few of the works about boundary layer and coherent structures are Grossmann and Lohse (2004), Stevens et al. (2010), van Reeuwijk et al. (2008a) and van Reeuwijk et al. (2008b).

Although numerous works have been published on RBC, most of them have been performed at Prandtl numbers $Pr \sim \mathcal{O}(1)$ or higher (Kadanoff, 2001). Little attention has been given to low-Prandtl-number convection despite it is observed in the Sun's outer layer and is exploited in nuclear reactor applications and liquid metal batteries, see Nordlund et al. (2009), Grötzbach (2013) and Kelley and Sadoway (2014). The limited number of studies in such conditions is also motivated by inherent difficulties encountered in both experiments and numerical simulations. As no optical access is possible due to opacity of liquid metals, laboratory measurements are made by taking advantage of the electrical conductivity of such fluids by means of complex electromagnetic flow meters and magnetic probes (Schulenberg and Stieglitz, 2010). On the other hand Direct Numerical Simulations (DNSs) allow to obtain fully tridimensional fields of velocity components and temperature but they require a higher computational effort with respect to fluids with order-one Prandtl number. This is because of by one side the presence of large-scale thermal structures requires larger computational domains, while on the other higher amounts of energy are injected in the velocity field reducing the Kolmogorov scale and, as a consequence, requiring finer computational grids, see for example Calkins et al. (2012) and Schumacher et al. (2015).

In the present chapter RBC is analysed by means of DNSs in three different configurations, which involve fluids at different Prandtl numbers: liquid mercury ($Pr = 0.025$), air ($Pr = 0.7$) and water ($Pr = 7$). Instead of comparing results at constant Rayleigh number but different Prandtl number, present simulations are performed by varying Pr at constant Grashof number $Gr = Ra/Pr$. This approach, developed by Schumacher et al. (2015), allow to study the influence of the ratio between kinetic and thermal diffusivities while keeping unchanged the weight of different terms in the momentum equations. Buoyancy forces are considered in the governing equations through the Boussinesq's approximation, the validity of which is carefully addressed in section 2.3. Moreover the spatio-temporal discretisation is meticulously analysed *a posteriori* both in the bulk and

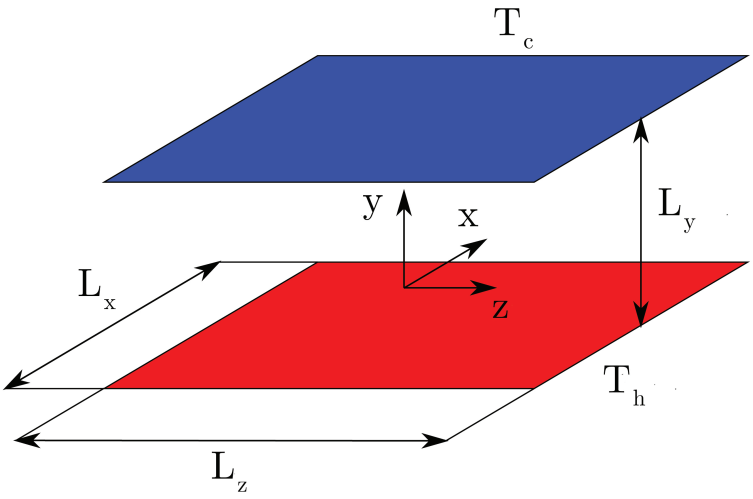

FIGURE 2.1: Sketch of the laterally unbounded Rayleigh-Bénard cell.

in the boundary layer regions. Attention is given also in the comparison between *a priori* estimations of the smallest scales of turbulence against values computed via statistics, see section 2.4. Results presented in section 2.5 are aimed to analyse different features of heat and momentum transfers in configuration studied. Instantaneous fields and spatial autocorrelations provide quantitative and qualitative information about plumes characteristics at different Prandtl number, while single-point statistics are aimed at comparing present results with published literature.

2.2 Flow configuration and numerical parameters

Turbulent natural convection is studied in the laterally unbounded Rayleigh-Bénard configuration, a sketch of it is reported in figure 2.1.

The flow regime in RBC is determined by Rayleigh and Prandtl numbers (Tritton, 1988), which are defined as

$$Ra = \frac{g\,\beta\,\Delta T\,H^3}{\nu\,\alpha} \qquad Pr = \frac{\nu}{\alpha} \tag{2.1}$$

In these definitions H is the height of the Rayleigh-Bénard cell, ΔT is the temperature difference between hot and cold walls, g is gravity and β, α and ν represent respectively thermal expansion coefficient, thermal diffusivity and kinematic viscosity of the operating fluid. When dealing with buoyancy driven flows there is no velocity scale directly imposed by boundary conditions, thus a velocity scale has to be derived from other quantities involved in the problem definition. In RBC it is usual to consider as velocity scale the free-fall velocity of thermals U_{ff} (Gray and Giorgini, 1976) defined as

$$U_{ff} = \sqrt{g\,\beta\,\Delta T\,H} \tag{2.2}$$

Then Reynolds number based on the free-fall velocity reads

$$Re = \frac{U_{ff}\,H}{\nu} \tag{2.3}$$

and Grashof number is

$$Gr = \frac{g\,\beta\,\Delta T\,H^3}{\nu^2} \tag{2.4}$$

From definitions (2.1), (2.3) and (2.4) it follows that

$$Gr = \frac{Ra}{Pr} = Re^2 \tag{2.5}$$

The system of non-dimensional governing equations in RBC has been introduced in section 1.2. This is rewritten here in a more convenient form by considering relation (2.5)

$$\begin{gathered}
\frac{\partial u_i}{\partial x_i} = 0 \\
\frac{\partial u_i}{\partial t} + \frac{\partial u_i u_j}{\partial x_j} = -\frac{\partial p}{\partial x_i} + \frac{1}{\sqrt{Gr}}\,\frac{\partial^2 u_i}{\partial x_j\,\partial x_j} + \theta\delta_{i2} \\
\frac{\partial \theta}{\partial t} + \frac{\partial \theta u_j}{\partial x_j} = \frac{1}{Pr\sqrt{Gr}}\,\frac{\partial^2 \theta}{\partial x_j\,\partial x_j}
\end{gathered} \tag{2.6}$$

In equations (2.6) variables are made non-dimensional by using H, U_{ff} and ΔT respectively as reference length, velocity and temperature; δ_{i2} is the Kronecker delta. This form of the governing equations clarifies that studying RBC at constant Grashof number but different Prandtl number allows to maintain the momentum equations unchanged. By varying Pr only the energy equation is directly modified, the dynamical field is indirectly affected through the buoyancy term, see the paper by Schumacher et al. (2015) where this approach has been introduced.

Case	Ra	Pr	$L_x \times L_y \times L_z$	$n_x \times n_y \times n_z$	Δt	$\Delta\tau$
LME	1.25×10^6	0.025	$8 \times 1 \times 8$	$1458 \times 513 \times 1458$	5×10^{-5}	100
AIR	3.5×10^7	0.7	$8 \times 1 \times 8$	$1024 \times 513 \times 1024$	5×10^{-5}	125
WAT	3.5×10^8	7	$8 \times 1 \times 8$	$2592 \times 513 \times 2592$	5×10^{-5}	110

TABLE 2.1: Parameters of the simulations. $L_x \times L_y \times L_z$ and $n_x \times n_y \times n_z$ are the domain dimensions and computational grid, Δt is the time step and $\Delta\tau$ is the time period over which statistics are gathered.

Numerical parameters of the simulations are summarised in table 2.1. Boundary conditions impose periodicity along x and z directions while at y-normal walls no-slip conditions are applied for the velocity field. Temperature is set to $\theta_h = 0.5$ and $\theta_c = -0.5$, respectively on the lower and upper wall. The time advancement scheme is the second-order Adams-Bashforth in every configuration. For simulations AIR and WAT the fully explicit code has been used, while for LME case the semi-implicit code by Flageul et al. (2015) has been employed due to stability problems arose because of the low Prandtl number and the small grid spacing employed in y-direction, as already mentioned in section 1.4. After an initial transient, statistics have been gathered for a time period $\Delta\tau$. Statistical convergence is assessed later in section 2.4.

2.3 Validity of the Boussinesq's approximations

The sets of non-dimensional governing equations (1.2) and (2.6) underlies a series of assumptions named after Boussinesq (Boussinesq, 1903) and firstly used by Oberbeck (1879). The applicability of these assumptions has to be carefully assessed in order to correctly represent the problem addressed by keeping simulation errors under control.

The Boussinesq's approximation consider the following hypotheses (Gray and Giorgini, 1976; Tritton, 1988):

- density is constant in every term of the governing equations except for the gravitational term, where density is linearly variable with temperature;
- all the other fluid properties are considered constant;

- viscous dissipation and hydrostatic effects are negligible in the energy equation.

Given a fluid at a thermodynamic condition defined by temperature T^0 and pressure p^0, the validity of above assumptions can be checked by validity maps constructed using the method by Gray and Giorgini (1976), as done in paper by Angeli et al. (2019). These maps are regions of the bidimensional space $\Delta T_{ref} - L_{ref}$ (reference temperature difference and reference length) where assumptions listed above are verified within a given tolerance. Usually 10% variations of thermophysical properties around their reference values, observed in reference conditions (T^0, p^0), are permitted.

Figures 2.2, 2.3 and 2.4 display the validity region of the Boussinesq approximation in LME, AIR and WAT configurations. Reference conditions and permitted variations on thermophysical properties are reported in the figure captions. In addition red dashed lines which represent non-dimensional parameters of configurations studied are drawn. In LME configuration the operating fluid considered is liquid mercury and its thermophysical properties have been taken from Engineering ToolBox (2005), while in AIR and WAT cases, where the operating fluid is respectively air and water, properties are gathered from Eckert and Drake (1987) and Holmgren (2006).

It appears that in LME and WAT configurations the validity region is widely extended around the line representing actual conditions, thus the Boussinesq formulation is deemed to be suitable to describe natural convection phenomena in such configurations, see figures 2.2 and 2.4. For liquid mercury the reference length (*i.e.* the cell height in RBC) is limited by hydrostatic effects, while the limiting temperature difference ΔT_{ref} is about 20.3° C and is related to the variations of specific heat with temperature. Specific heat is indeed the most sensitive property to temperature of liquid mercury. The maximum temperature difference in WAT at which the Boussinesq's approximation is valid is instead defined by the variations of viscosity with temperature. Besides, L_{ref} is limited by hydrostatic effects (inclined line) and by variations of thermal conductivity with pressure (horizontal line). On the other hand the operating conditions in AIR configuration are included in the Boussinesq's validity region only in a small portion, whilst a 15% tolerance on variations of air thermophysical properties is considered. For this fluid the most limiting conditions are dictated by the variations of density with pressure and the variations of thermal conductivity with temperature, which respectively limit the characteristic length and temperature difference. Although the intersection between the validity region and the line

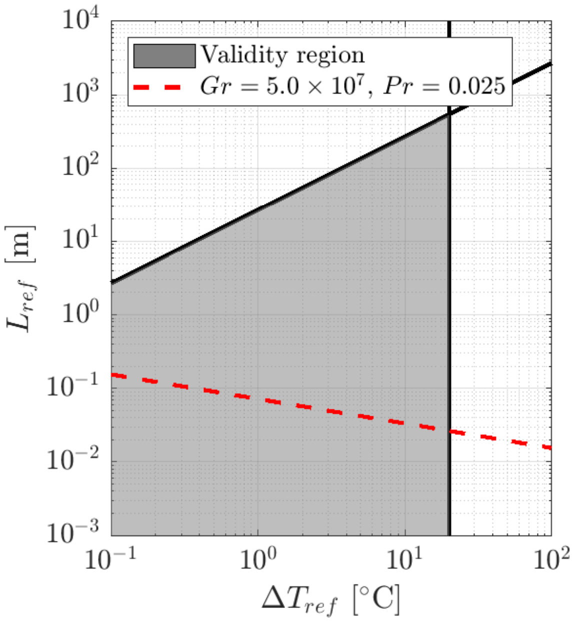

FIGURE 2.2: Validity region of the Boussinesq's approximation for liquid mercury (LME case) constructed using the method by Gray and Giorgini (1976). Reference conditions are $T^0 = 20°$ C and $p^0 = 1$ atm, and 10% relative variations of thermophysical properties around reference values are allowed.

representing actual conditions is small, the Boussinesq's formulation is considered to hold in this study. For example when $\Delta T_{ref} = 60°\mathrm{C}$ and $L_{ref} = 0.39$ m errors are below 15%.

2.4 Assessment of the spatio-temporal discretisation

2.4.1 Consistency relations

The accuracy of the numerical procedure in RBC can be assessed by checking if the consistency relations hold. These are exact relations proposed by Shraiman and Siggia (1990) and Siggia (1994) which are derived from the set of governing

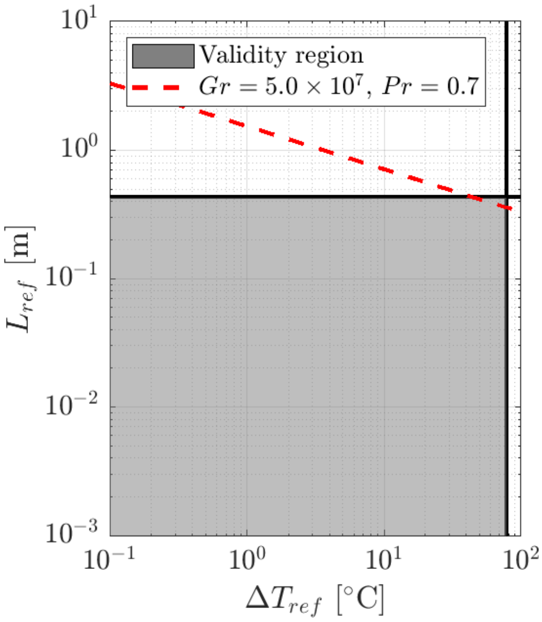

FIGURE 2.3: Validity region of the Boussinesq's approximation for air (AIR case) constructed using the method by Gray and Giorgini (1976). Reference conditions are $T^0 = 70°$ C and $p^0 = 1$ atm, and 15% relative variations of thermophysical properties around reference values are allowed.

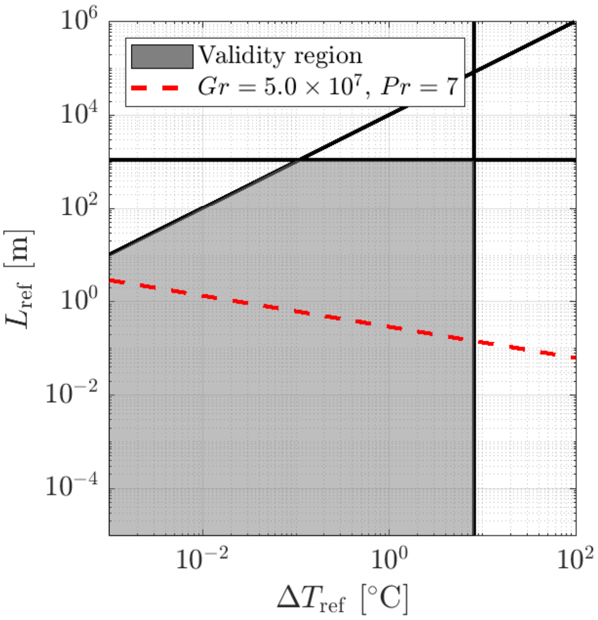

FIGURE 2.4: Validity region of the Boussinesq's approximation for water (WAT case) constructed using the method by Gray and Giorgini (1976). Reference conditions are $T^0 = 20°$ C and $p^0 = 1$ atm, and 10% relative variations of thermophysical properties around reference values are allowed.

equations (2.6)

$$Nu = 1 + \sqrt{RaPr}\,\langle v'\theta'\rangle_V$$
$$Nu = 1 + \sqrt{RaPr}\,\langle \tilde{\varepsilon}'\rangle_V \tag{2.7}$$
$$Nu = \sqrt{RaPr}\,\langle \tilde{\varepsilon_\theta}'\rangle_V$$

where $\langle\,\rangle_V$ indicates values averaged over the entire computational domain and $\tilde{\varepsilon}'$ is the pseudo-dissipation rate of kinetic energy defined as

$$\tilde{\varepsilon}' = \frac{1}{\sqrt{Gr}}\left(\frac{\partial u_i}{\partial x_j}\frac{\partial u_i}{\partial x_j}\right) \tag{2.8}$$

and $\tilde{\varepsilon_\theta}'$ is the dissipation rate of temperature

$$\tilde{\varepsilon_\theta}' = \frac{1}{\sqrt{Gr}\,Pr}\left(\frac{\partial \theta}{\partial x_i}\frac{\partial \theta}{\partial x_i}\right) \tag{2.9}$$

Note that in definitions (2.8) and (2.9) velocity components and temperature are considered, not only their turbulent fluctuations as done in equations (2.27) and (2.35) to compute the turbulent dissipation rates.

In table 2.2 the Nusselt numbers computed using the consistency relations (2.7) are compared with Nusselt number calculated through the wall-normal first derivative of temperature at the walls. In non-dimensional form

$$Nu = \left.\frac{\partial\langle\theta\rangle}{\partial y}\right|_w \tag{2.10}$$

where $\langle\,\rangle$ indicates the ensemble average in general. In the flow under investigation average values are computed considering that the flow is statistically homogeneous in time and along the horizontal directions, x and z. Also symmetry or antisymmetry about the mid-channel plane $y = 0$ is exploited. The comparison in table 2.2 shows a very good agreement, thus numerical procedure employed is deemed to be accurate in each configuration.

2.4.2 Turbulence micro-scales

The discretisation in space and time has been checked *a posteriori* by comparing grid spacing and time step against the turbulence micro-scales. In $Pr < 1$ fluids, such as in LME and AIR configurations, the smallest scales observed in the flow are the Kolmogorov length η_K and time τ_K scales (Kolmogorov, 1941), defined

Case	Nu	$\dfrac{1+\sqrt{RaPr}\langle v'\theta'\rangle_V}{Nu}$	$\dfrac{1+\sqrt{RaPr}\langle \tilde{\varepsilon}'\rangle_V}{Nu}$	$\dfrac{\sqrt{RaPr}\langle \tilde{\varepsilon_\theta}'\rangle_V}{Nu}$
LME	5.33	1.0006	0.9991	1.0002
AIR	22.33	1.0006	1.0005	0.9989
WAT	44.12	0.9981	1.0006	0.9991

TABLE 2.2: Comparison of Nusselt number computed using equation (2.10) with consistency relations (2.7).

as

$$\eta_K^* = \left(\frac{\nu^{*3}}{\varepsilon^*}\right)^{1/4} \qquad \tau_K^* = \left(\frac{\nu^*}{\varepsilon^*}\right)^{1/2} \tag{2.11}$$

where the asterisk marks dimensional quantities. On the other hand when $Pr > 1$ as in the WAT case Batchelor (1959) states that the scalar energy spectrum is extended beyond the cut-off wavenumber of the turbulent kinetic energy spectrum. Diffusive effects in the scalar field become important at a wavenumber corresponding to the Batchelor scale η_B

$$\eta_B^* = \left(\frac{\nu^*\,\alpha^{*2}}{\varepsilon^*}\right)^{1/4} = \frac{\eta_K^*}{Pr^{1/2}} \tag{2.12}$$

The smallest time scale of temperature fluctuations is derived by considering η_B and the Kolmogorov velocity $u_K = \eta_K/\tau_K$

$$\tau_B^* = \frac{\eta_B^*}{u_K^*} = \left(\frac{\alpha^*}{\varepsilon^*}\right)^{1/2} \tag{2.13}$$

A short digression on the smallest length scale of the scalar field is worth here. Obukhov (1949) and Corrsin (1951) found that the smallest length scale in the temperature spectrum is

$$\eta_T^* = \left(\frac{\alpha^{*3}}{\varepsilon^*}\right)^{1/4} = \frac{\eta_K^*}{Pr^{3/4}} \tag{2.14}$$

However, as stated by Batchelor (1959), for $Pr > 1$ the velocity field at scales $\eta_K > \eta > \eta_B$ is smoothed out by viscous effects while the scalar field still exhibits fluctuations. This affects the scale at which the advective term balances the diffusive one in the energy equation, which is the Batchelor scale η_B defined in equation (2.12).

Case	Δx^+ and Δz^+	$\Delta y^+\|_{wall}$	$\Delta y^+\|_{centre}$	Δt^+
LME	3.039	0.696	0.904	0.129
AIR	2.766	0.275	0.923	0.053
WAT	1.866	0.340	2.227	0.058

TABLE 2.3: Discretisation in space and time expressed in terms of the smallest scales (+ superscript) of the velocity field (LME and AIR configurations) or temperature field (WAT case).

In non-dimensional form the Kolmogorov length and time scales write

$$\langle \eta_K \rangle = \left(\frac{Gr^{-3/2}}{\langle \varepsilon \rangle} \right)^{1/4} \qquad \langle \tau_K \rangle = \left(\frac{Gr^{-1/2}}{\langle \varepsilon \rangle} \right)^{1/2} \tag{2.15}$$

while Batchelor scales are

$$\langle \eta_B \rangle = \left(\frac{Gr^{-3/2}\, Pr^{-2}}{\langle \varepsilon \rangle} \right)^{1/4} \qquad \langle \tau_B \rangle = \left(\frac{Gr^{-1/2}\, Pr^{-1}}{\langle \varepsilon \rangle} \right)^{1/2} \tag{2.16}$$

where the angular brackets indicate averaged values. Dissipation of turbulent kinetic energy ε is defined as

$$\varepsilon = \frac{2}{\sqrt{Gr}} \left(s_{ij}\, s_{ij} \right) \tag{2.17}$$

where $s_{ij} = 0.5\,(\partial u_i'/\partial x_j + \partial u_j'/\partial x_i)$ for $i, j = 1, 2, 3$ is the strain rate tensor. Table 2.3 reports the ratio between grid spacings and time step employed in present simulations and the smallest scales computed *a posteriori* using relations (2.15) for LME and AIR cases, and relations (2.16) for WAT configuration. Spatial and temporal discretisations employed meet the requirements for state-of-the-art DNSs, see Moin and Mahesh (1998).

2.4.3 Boundary layers discretisation

In addition to the requirements in terms of the smallest turbulence scales, the computational grid in a well-resolved DNS must also be suited to correctly represent the flow inside the thermal and velocity boundary layers. According to Shishkina et al. (2010) the number of grid points needed to correctly resolve the thermal and velocity boundary layers are respectively

$$N_{BL,\theta} \geq \begin{cases} \sqrt{2}\, a\, Nu^{1/2}\, Pr^{-3/4}\, A^{3/2}\, \pi^{3/4} & Pr < 3 \times 10^{-4} \\ \sqrt{2}\, a\, Nu^{1/2}\, Pr^{(-0.5355+0.033 log\, Pr)} & 3 \times 10^{-4} \leq Pr \leq 1 \\ \sqrt{2}\, a\, Nu^{1/2}\, Pr^{(-0.0355+0.033 log\, Pr)} & 1 < Pr \leq 3 \\ \sqrt{2}\, a\, Nu^{1/2}\, E^{3/2} & Pr > 3 \end{cases} \tag{2.18}$$

and

$$N_{BL,u} \geq \begin{cases} \sqrt{2}\, a\, Nu^{1/2}\, Pr^{-1/4}\, A^{1/2}\, \pi^{1/4} & Pr < 3 \times 10^{-4} \\ \sqrt{2}\, a\, Nu^{1/2}\, Pr^{(-0.1785+0.011 log\, Pr)} & 3 \times 10^{-4} \leq Pr \leq 1 \\ \sqrt{2}\, a\, Nu^{1/2}\, Pr^{(0.3215+0.011 log\, Pr)} & 1 < Pr \leq 3 \\ \sqrt{2}\, a\, Nu^{1/2}\, Pr^{1/3}\, E^{1/2} & Pr > 3 \end{cases} \tag{2.19}$$

where $a = 0.482$, $A = 0.332$ and $E = 0.982$ are constants derived when approximating the Prandtl-Blasius boundary layer theory, see Shishkina et al. (2010).

In this study the thermal boundary layer thickness δ_θ is derived by assuming that δ_θ is the height of a quiescent fluid layer subject to a temperature difference $\Delta T/2$, where heat is solely diffused throughout the layer with a temperature gradient equal to the average temperature derivative at walls, see Chillà and Schumacher (2012). Mathematically this means

$$\frac{\Delta T}{2\, \delta_\theta^*} = \left. \frac{\partial T}{\partial y^*} \right|_w \tag{2.20}$$

where the asterisk marks dimensional quantities. Considering equation (2.10) the non-dimensional boundary layer thickness becomes

$$\delta_\theta = \frac{H}{2\, Nu} \tag{2.21}$$

On the other hand the velocity boundary layer thickness δ_u is computed as in Shishkina et al. (2010)

$$\delta_u = \begin{cases} 0.5\, Nu^{-1}\, Pr^{1/2}\, A^{-1}\, \pi^{-1/2}\, H & Pr < 3 \times 10^{-4} \\ 0.5\, Nu^{-1}\, Pr^{(0.357-0.022\, log\, Pr)}\, H & 3 \times 10^{-4} \leq Pr \leq 3 \\ 0.5\, Nu^{-1}\, Pr^{1/3}\, E^{-1}\, H & Pr > 3 \end{cases} \tag{2.22}$$

To develop equations (2.22) the boundary layer is assumed to be *scalingwise* laminar, which means that boundary layer characteristics scale as predicted by

Case	δ_θ	δ_u
LME	0.0938	0.0221
AIR	0.0224	0.0197
WAT	0.0113	0.0221

TABLE 2.4: Thicknesses of the thermal (δ_θ) and kinetic (δ_u) boundary layers in investigated configurations.

the Prandtl-Blasius theory for laminar boundary layers, as reported by Sun et al. (2008). As stated by Landau and Lifshitz (1987) this assumption does not hold when the shear Reynolds number Re_s is above 420. Re_s is defined as

$$Re_s = \frac{U\,\delta_u}{\nu} \sim \sqrt{\frac{UH}{\nu}} \tag{2.23}$$

where U is the velocity scale of large-scale motions. The calculation of the Reynolds number relative to the large-scale circulation UH/ν as reported in Grossmann and Lohse (2000) indicates that configurations LME, AIR and WAT are characterised by shear Reynolds number respectively of 25.7, 16.9 and 12.0, well below the threshold $Re_s = 420$.

In table 2.4 are reported the thicknesses of thermal and velocity boundary layers for the three cases considered. As one may expect, because of the different Prandtl numbers, the thermal boundary layer thicknesses are quite different from one case to the others. Instead δ_u is similar among the configurations studied and deviations of δ_u with respect to the mean value $\bar{\delta_u} = 0.0213$ are within 7.5%. This suggests that configurations with constant Grashof number exhibit a large scale motion of similar intensity, as the existence of a velocity boundary layer is related to the mean wind, see also Grossmann and Lohse (2000).

The comparison between the boundary layers resolution in present configurations and requirements calculated by equations (2.18) and (2.19) is reported in table 2.5. Actual computational grids largely exceed the requirements which are obtained by comparing the Nusselt number in simulations with increasing mesh density, see Shishkina et al. (2010). The usage of coarser resolutions has not been taken into account as it leads to rough statistics, this may be observed in the profiles of turbulent kinetic energy and temperature variance balance equations reported section 2.5.3.

The above statement regarding the thickness of the velocity boundary layer

Case	$N'_{BL,\theta}/N_{BL,\theta}$	$N'_{BL,u}/N_{BL,u}$
LME	72/13.8	18/3.2
AIR	29/3.9	26/3.4
WAT	21/4.4	39/8.6

TABLE 2.5: Comparison between the number of grid points actually placed within the thermal and velocity boundary layers (primed values) and discretisation suggested by Shishkina et al. (2010). Requirements are largely met.

have to be considered carefully as the definition of such a quantity is still discussed by the scientific community. For example van Reeuwijk et al. (2008a) define δ_u as the wall-normal distance at which the intensity of horizontal fluctuations peaks, while Stevens et al. (2010) compute the velocity boundary layer thickness as twice the wall distance at which the kinetic energy dissipation rate ε''_u reach a maximum value, where

$$\varepsilon''_u = \langle u_i \frac{\partial^2 u_i}{\partial x_j \, \partial x_j} \rangle \tag{2.24}$$

Figure 2.5 shows the profiles of ε''_u in the configurations considered, as well as the peak positions and the boundary layer thickness according to Stevens et al. (2010). To summarise, table 2.6 reports the velocity boundary layer thicknesses following the different definitions presented. Although Shishkina et al. (2010) report that equations (2.22) provide results similar to the criterion by Stevens et al. (2010), this is not the case in present simulations. Differences may be due to the aspect ratio of the domain (1 in Shishkina et al. (2010), 8 in present studies) and the Rayleigh number set when $Pr = 0.7$, which in Shishkina et al. (2010) is two orders of magnitude higher than in present AIR configuration. Criterion by van Reeuwijk et al. (2008a) results in similar thicknesses between each others, but values are about three times larger than predictions by Shishkina et al. (2010). Finally, the method by Stevens et al. (2010) provides δ_u values quite different in configurations studied. Only in case AIR the result is similar with respect to the calculation by Shishkina et al. (2010).

2.4.4 *A priori* assessment of discretisation

Approximated forms of equations (2.11), (2.12) and (2.14) are usually employed in order to assess the spatio-temporal discretisation at the stage of simulation

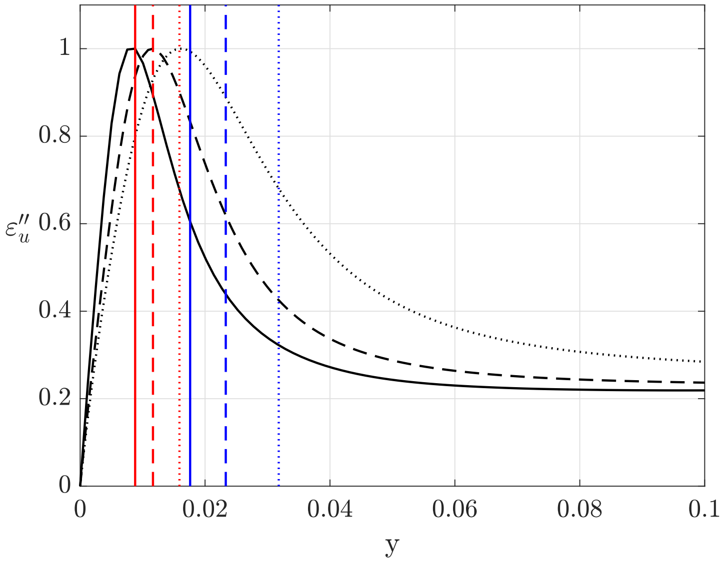

FIGURE 2.5: Profiles of kinetic energy dissipation rate ε''_u (equation (2.24)) in configurations studied. Solid, dashed and dotted lines represent respectively LME, AIR and WAT cases. Black curves represent the profiles of ε''_u, red and blue vertical lines indicate respectively the wall-normal distances at which maxima are observed and the boundary layer thicknesses according to Stevens et al. (2010).

δ_u	LME	AIR	WAT
Shishkina et al. (2010)	0.0221	0.0197	0.0221
Stevens et al. (2010)	0.0176	0.0233	0.0318
van Reeuwijk et al. (2008a)	0.0614	0.0573	0.0653

TABLE 2.6: Comparison between velocity boundary layer thicknesses computed using different criteria found in literature.

setup. As suggested by Shishkina et al. (2010) and Scheel et al. (2013), the smallest scales of turbulent fields can be predicted as

$$\eta_K'^* = \left(\frac{\nu^{*3}}{\tilde{\varepsilon}^*}\right)^{1/4} \qquad \tau_K'^* = \left(\frac{\nu^*}{\tilde{\varepsilon}^*}\right)^{1/2} \tag{2.25}$$

and

$$\eta_B'^* = \left(\frac{\nu^* \, \alpha^{*2}}{\tilde{\varepsilon}^*}\right)^{1/4} \qquad \tau_B'^* = \left(\frac{\alpha^*}{\tilde{\varepsilon}^*}\right)^{1/2} \tag{2.26}$$

With respect to equations (2.11), (2.12) and (2.14), in equations (2.25) and (2.26) the pseudo-dissipation rate of turbulent kinetic energy $\tilde{\varepsilon}$ defined as

$$\tilde{\varepsilon} = \frac{1}{\sqrt{Gr}} \left(\frac{\partial u_i'}{\partial x_j} \frac{\partial u_i'}{\partial x_j} \right) \tag{2.27}$$

is used instead of ε. The difference between these two quantities is

$$\varepsilon - \tilde{\varepsilon} = \frac{1}{\sqrt{Gr}} \frac{\partial^2 (u_i' \, u_j')}{\partial x_i \, \partial x_j} \tag{2.28}$$

and is seldom important in almost all circumstances, as stated by Pope (2001). To check this assumption figure 2.6 reports the ratio $\langle \varepsilon \rangle / \langle \tilde{\varepsilon} \rangle$ in the three cases considered. Difference (2.28) is well below 5% except for the region close to the walls.

In laterally unbounded RBC the averaged velocity components are zero, $\langle u_i \rangle$ for $i = 1, 2, 3$, therefore the pseudo-dissipation of turbulent kinetic energy $\tilde{\varepsilon}$ (equation (2.27)) equals the pseudo-dissipation of kinetic energy $\tilde{\varepsilon}'$ (equation (2.8)). Thus it is possible to introduce the consistency relations (2.7) in equations (2.25) and (2.26) to compute Kolmogorov and Batchelor scale in non-dimensional form as

$$\begin{aligned} \langle \eta_K' \rangle_V &= \left(\frac{Pr}{Gr \, (Nu - 1)} \right)^{1/4} & \qquad \langle \tau_K' \rangle_V &= \eta_K^2 \sqrt{Gr} \\ \langle \eta_B' \rangle_V &= \left(\frac{1}{Gr \, Pr \, (Nu - 1)} \right)^{1/4} & \qquad \langle \tau_B' \rangle_V &= \frac{\eta_B^2 \sqrt{Gr}}{Pr^{1/2}} \end{aligned} \tag{2.29}$$

where Nu can be estimated *a priori* using the unifying theory by Grossmann and Lohse (2000). A similar way to estimate mesh requirements in the bulk was first proposed by Grötzbach (1983).

Table 2.7 reports the comparison between the smallest scales of velocity and temperature fields computed *a priori*, using equations (2.29) (denoted by prime superscripts), and *a posteriori*, obtained by relations (2.15) and (2.16) with $\langle \varepsilon \rangle$

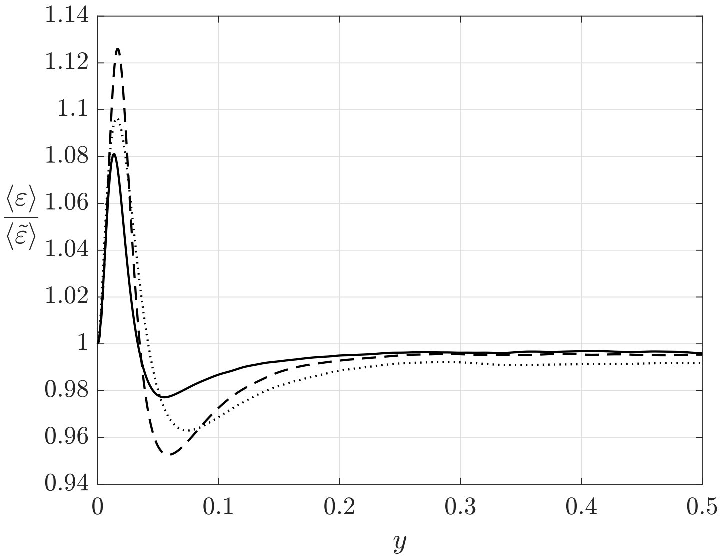

FIGURE 2.6: Ratio between turbulent kinetic energy dissipation $\langle\varepsilon\rangle$ and the average pseudo-dissipation of turbulent kinetic energy $\langle\tilde{\varepsilon}\rangle$. Solid, dashed and dotted lines indicate respectively LME, AIR and WAT configurations.

substituted by $\langle\varepsilon\rangle_V$. The comparison shows that equations (2.29) predict well Kolmogorov and Batchelor scales. The only notable difference lies in the Batchelor time scale in WAT configuration, where the value computed *a priori* is one order of magnitude smaller than the one computed from results. Previous comparisons should be considered carefully as they involve quantities which are averaged over the entire domain. Those comparisons still hold true in the bulk region, *i.e.* close to mid-channel height $y = 0$, but if one compares scales computed *a priori* against the minimum values computed at the walls, where $\langle\varepsilon\rangle$ is maximum and in general quite different from $\langle\varepsilon\rangle_V$, differences arise, see table 2.8. While length scales predicted are about twice the minimum values computed at the walls *a posteriori*, the predicted time scales are two order of magnitude larger than results in LME and AIR configurations, and almost 30 times larger in WAT case.

To summarise, equations (2.29) allow to compute within a good approximation the smallest length scales before the calculations both in the bulk region, where they are almost correct, and close to the walls, where error factors ~ 2 are found. On the contrary time scales computed *a priori* are almost 200 times larger than minimum values computed *a posteriori* when $Pr = 0.025$ and 30 times when $Pr = 7$. In the bulk also time scales predictions are correct or smaller than the outcomes.

Case	$\langle\eta'_K\rangle_V$ or $\langle\eta'_B\rangle_V$	$\langle\eta_K\rangle_V$ or $\langle\eta_B\rangle_V$	$\langle\tau'_K\rangle_V$ or $\langle\tau'_B\rangle_V$	$\langle\tau_K\rangle_V$ or $\langle\tau_B\rangle_V$
LME	3.21×10^{-3}	3.28×10^{-3}	7.30×10^{-2}	7.60×10^{-2}
AIR	5.22×10^{-3}	5.06×10^{-3}	1.93×10^{-1}	1.81×10^{-1}
WAT	2.96×10^{-3}	2.85×10^{-3}	2.34×10^{-2}	1.52×10^{-1}

Table 2.7: Comparison between the Kolmogorov and Batchelor scales (length η and time τ) computed *a priori* (prime superscripts) and volume-averaged values computed from the results.

Case	$\langle\eta'_K\rangle_V$ or $\langle\eta'_B\rangle_V$	$\langle\eta_K\rangle_m$ or $\langle\eta_B\rangle_m$	$\langle\tau'_K\rangle_V$ or $\langle\tau'_B\rangle_V$	$\langle\tau_K\rangle_m$ or $\langle\tau_B\rangle_m$
LME	3.21×10^{-3}	1.81×10^{-3}	7.30×10^{-2}	3.88×10^{-4}
AIR	5.22×10^{-3}	2.82×10^{-3}	1.93×10^{-1}	9.49×10^{-4}
WAT	2.96×10^{-3}	1.65×10^{-3}	2.34×10^{-2}	8.60×10^{-4}

Table 2.8: Comparison between the Kolmogorov and Batchelor scales (length η and time τ) computed *a priori* (prime superscripts) and minimum values at the walls calculated from the statistics.

2.5 Results

2.5.1 Flow structures

Figures 2.7 and 2.8 display the instantaneous fields of non-dimensional temperature and velocity magnitude on xy-planes in configurations studied. As observed by Schumacher et al. (2015) in constant-Grashof-number conditions the lower is the Pr number the wider is the range of scales exhibited by the velocity field and the more diffusive is the temperature field behaviour. In addition the instantaneous fields of θ show that thermal plumes behave very differently as the Prandtl number changes. Configuration LME is characterised by large and almost wall-to-wall coherent structures, while in cases AIR and WAT plumes are narrow and they do not reach the opposite wall. This is more evident in figures 2.9, 2.10 and 2.11 which report the isosurface $\theta = 0.2$ coloured by the vertical y coordinate in configurations studied. At $Pr = 0.025$ there are few large mushroom-like plumes and these impinge on the opposite wall. For instance the isosurface in figure 2.9 reaches y-coordinate of 0.96, which falls inside the upper thermal boundary layer, $0.96 > 1 - \delta_\theta$, see table 2.4. Figure 2.10 shows that in AIR configuration plumes are thinner and most of them do not cross the plane $y = 0$, while in WAT case thermals identified by $\theta = 0.2$ are so thin that they can be barely seen and they do not reach the opposite half-channel region, see figure 2.11.

Differences in plume behaviour are due to the different ratio between kinetic and thermal diffusivities. In low-Pr fluids thermal diffusivity is high with respect to kinematic viscosity, thus plumes moving away from walls effectively transfer heat to the surrounding fluid increasing the plumes width, and these can reach the opposite wall as they are subject to low friction forces because of the relatively low viscosity. However the morphological evolution studied by Zhou et al. (2007), where swirling mushroom-like structures are emitted as a result of the collision and convolution of sheet-like plumes, is observed in every configuration studied, see figures 2.9, 2.10 and 2.11.

Fields of instantaneous vertical velocity component v and temperature θ on horizontal cross sections at the edge of the thermal boundary layer substantiate the above statements about flow structures, see figures 2.12, 2.13 and 2.14. In configuration LME (figure 2.12) the temperature field shows four large regions of warm fluid, connected to each other through fluid filaments at high temperature. Beside these regions some very cold fluid portions indicate the presence of cold plumes even at the edge of the hot thermal boundary layer. The velocity field in figure 2.12(b) reflects the temperature distribution as it shows that warm fluid is rising while cold plumes are falling. The same apply to configurations AIR and WAT (figures 2.13 and 2.14), but instead of large coherent fluid regions the network of sheet-like plumes is very dense and chaotic. Emission of very thin mushroom-like plumes is indicated by red spots in fields of vertical velocity v, see figures 2.13(b) and 2.14(b).

In configurations AIR and WAT the Large Scale Circulation (LSC), which appears in every Rayleigh-Bénard cell (Krishnamurti and Howard, 1981) and is one of the fundamentals in the widely-accepted scaling theory by Grossmann and Lohse (2000), occurs in locations characterised by a cluster of plumes as stated for example by Sun et al. (2005) and Niemela et al. (2001). In configuration AIR this is visible mainly in the upper-left and lower-right regions in figure 2.13(a), while in case WAT four clusters where sheet-like plumes are more dense are observed in figure 2.14(a). From this analysis it can inferred that while in fluids with $Pr \sim 1$ or higher the LSC is made by several plumes, in configuration where $Pr \sim \mathcal{O}(10^{-2})$ it is composed by single plumes. Therefore the findings by Verzicco and Camussi (1999), which discriminate an heat transfer regime dominated by LSC for $Pr \leq 0.35$ while for $Pr > 0.35$ heat is mainly transported by thermal plumes, might be revised. At low-Prandtl-numbers plumes are essentially large scale structures and therefore should be regarded as the LSC themselves.

Although the definition of thermal plumes is widely accepted, *i.e.* they are fluid portions characterised by a temperature contrast with the background or in other words temperature fluctuations of the same sign, quantitative criteria to define plumes extensions are yet an open problem (Chillà and Schumacher, 2012). One of the possible solutions is to quantify plumes size by using the spatial autocorrelations as they correlate fluctuations in two points of the domain. The autocorrelation function ρ is defined as

$$\rho_\phi(r, y) = \frac{\langle \phi'\left(\boldsymbol{\pi}, y\right) \phi'\left(\boldsymbol{\pi} + \boldsymbol{r}, y\right)\rangle}{\langle \phi'^{\,2}\left(\boldsymbol{\pi}, y\right)\rangle} \tag{2.30}$$

where ϕ is a velocity component or θ, $\boldsymbol{\pi} = (x, z)$ is a two-element vector representing the coordinates on horizontal planes and $\boldsymbol{r} = (r_x, r_y)$ is the separation vector, again on xz-planes, which indicates the correlation distance. The angular brackets $\langle\,\rangle$ indicates that statistics are obtained by averaging in time and along x and z directions. Due to horizontal homogeneity of statistics ρ is not dependent from $\boldsymbol{\pi}$ but only from the vertical coordinate y and the magnitude of the separation vector $r = |\boldsymbol{r}|$. Figures 2.15, 2.16 and 2.17 display the spatial autocorrelation functions at selected vertical coordinates normalised by the thermal boundary

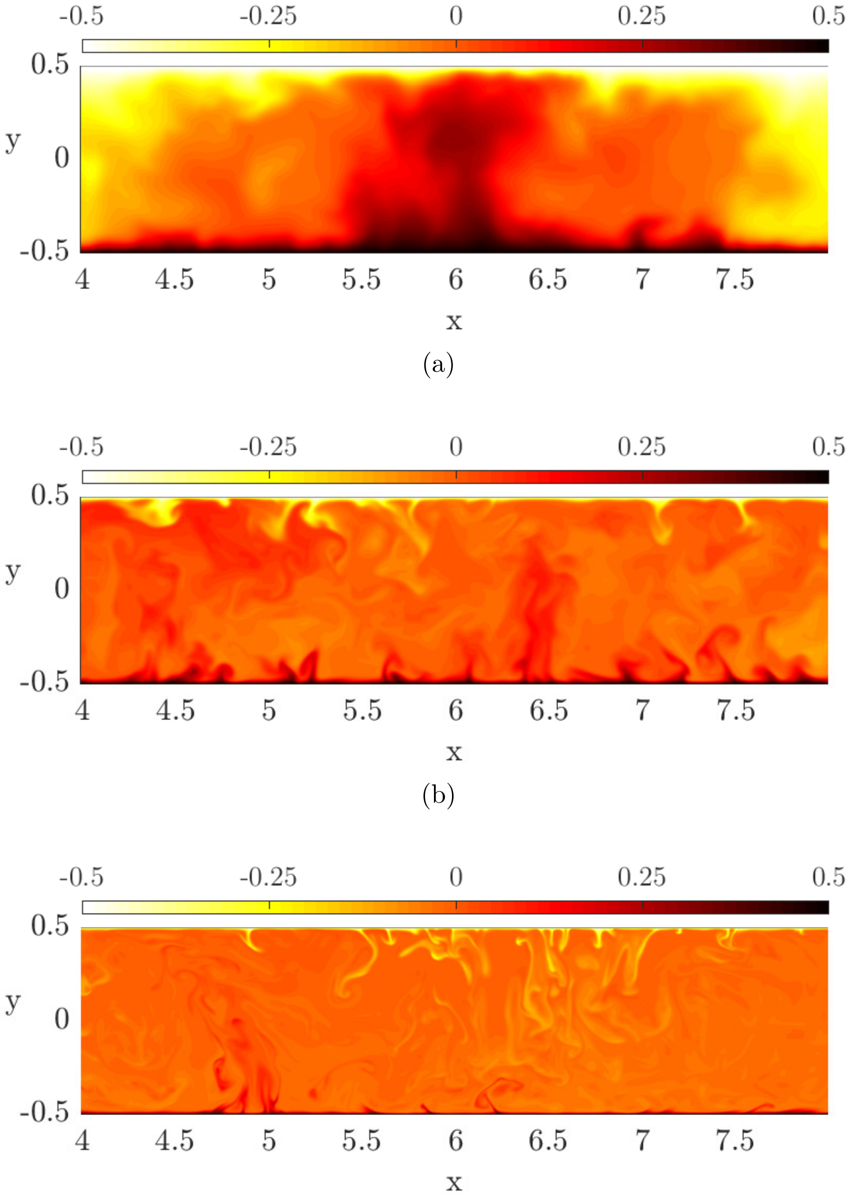

(a)

(b)

(c)

Figure 2.7: Instantaneous fields of non-dimensional temperature θ on a xy-plane in configurations (a) LME, (b) AIR and (c) WAT. Contours are limited to the region $x \in [L_x/2\ L_x]$ to compare flow details between different configurations.

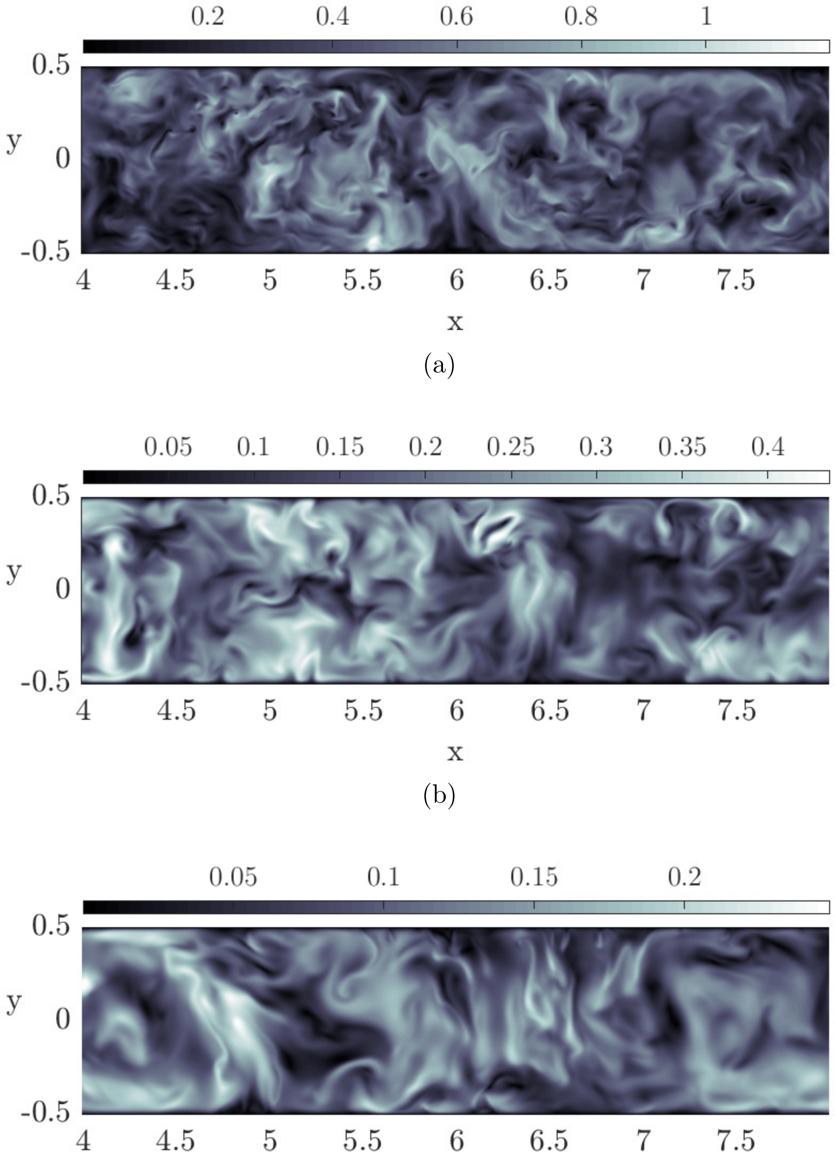

(a)

(b)

(c)

FIGURE 2.8: Instantaneous fields of velocity magnitude on a xy-plane in configurations (a) LME, (b) AIR and (c) WAT. Contours are limited to the region $x \in [L_x/2 \ \ L_x]$ to compare flow details between different configurations.

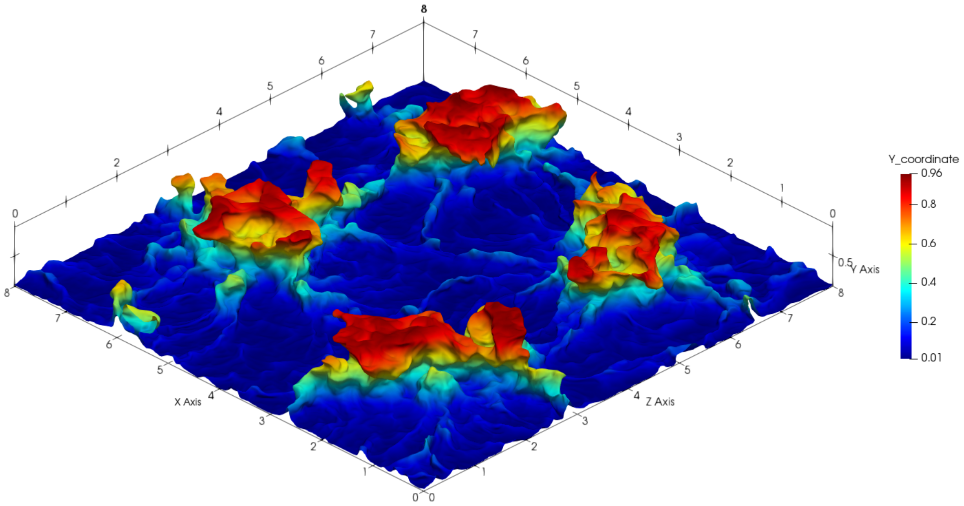

FIGURE 2.9: Isosurface $\theta = 0.2$ coloured by the vertical y coordinate, LME configuration.

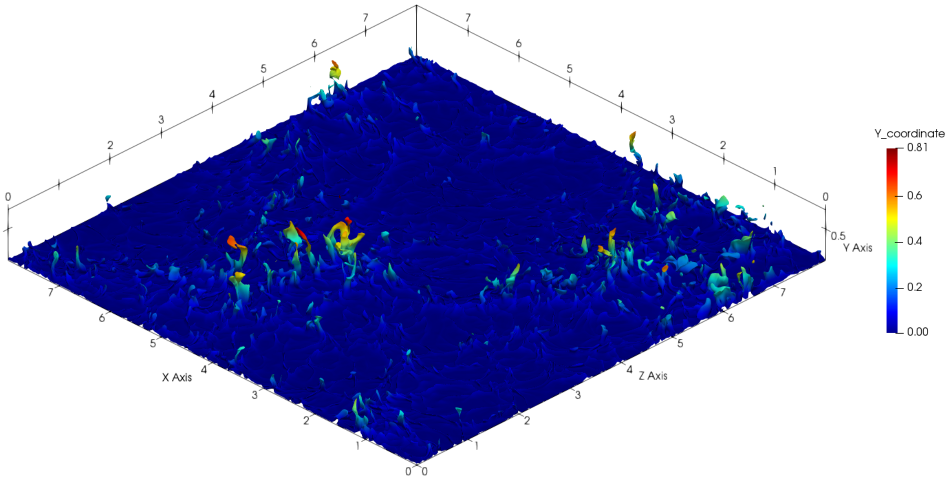

FIGURE 2.10: Isosurface $\theta = 0.2$ coloured by the vertical y coordinate, AIR configuration.

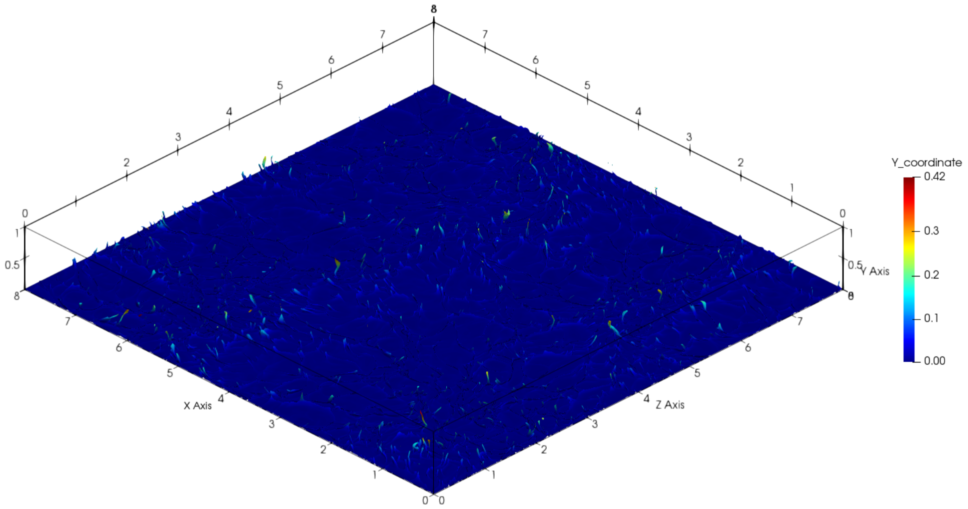

FIGURE 2.11: Isosurface $\theta = 0.2$ coloured by the vertical y coordinate, WAT configuration.

layer thickness. Due to statistical isotropy in xz plane, statistics involving the horizontal velocity components u and w are averaged together. In addition also the parabolas osculating $\rho_\theta(r = 0)$ are reported in the graphs. This geometric construction is made to clarify the concept of the Taylor scale (Pope, 2001) which is used here to quantify plumes width. The Taylor scale is defined as the abscissa at which the osculating parabola crosses the x-axis in the autocorrelation graphs. In mathematical form

$$\lambda = \sqrt{\frac{-2}{\rho_\theta''(r=0)}} \tag{2.31}$$

where $\rho_\theta''(r = 0)$ is the second-order derivative of the θ autocorrelation coefficient with respect to r, evaluated at $r = 0$. Plumes width can be considered to be equal to twice λ due to the symmetric behaviour of the autocorrelation function about $r = 0$. Table 2.9 reports plumes width at different heights in all the configurations considered. Data show that in LME configuration plumes have a minimum width inside the thermal boundary layer ($y = 0.5\,\delta_\theta$) and they increase their size while travelling towards the opposite wall. Plumes size computed through this criterion agrees with evaluations that can be made on the instantaneous temperature field, see figure 2.7(a). On the contrary in WAT case plumes have their maximum horizontal extension inside the thermal boundary layer, which in this case means very close to the walls, and reduce their width as moving away from the walls. In AIR configuration an almost constant width is observed at vertical coordinates

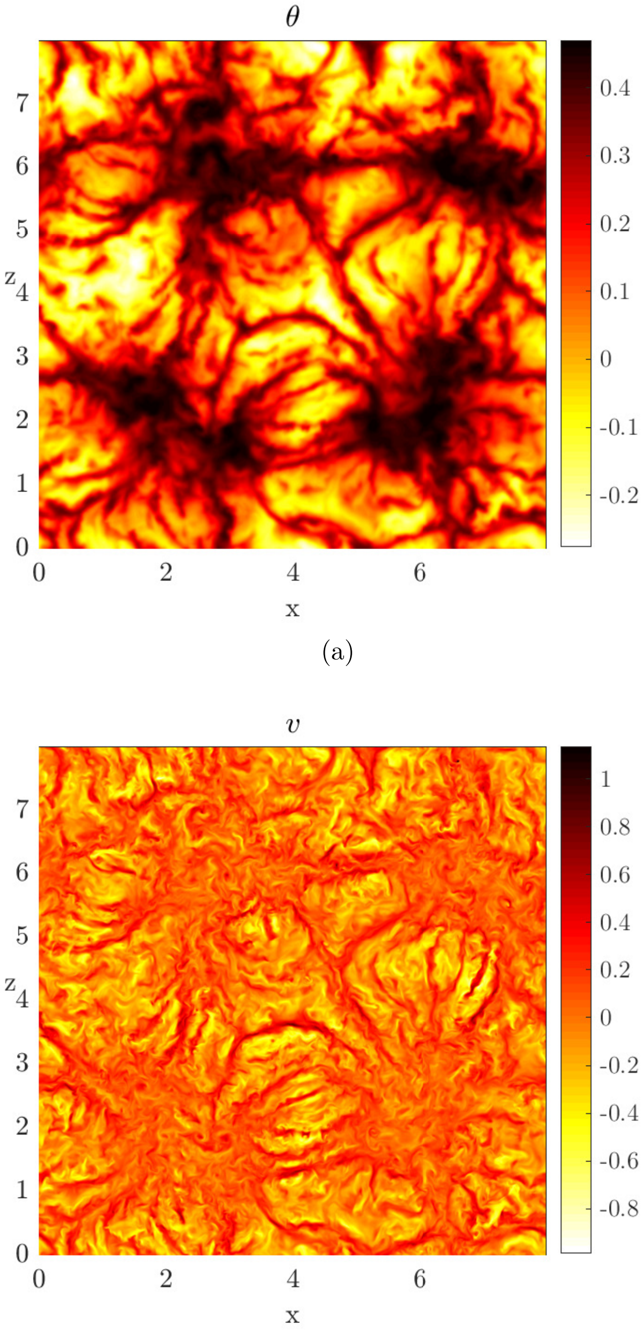

(a)

(b)

FIGURE 2.12: Instantaneous fields of non-dimensional temperature θ (a) and vertical velocity v (b) on the horizontal section at $y = \delta_\theta = 0.094$. Case LME.

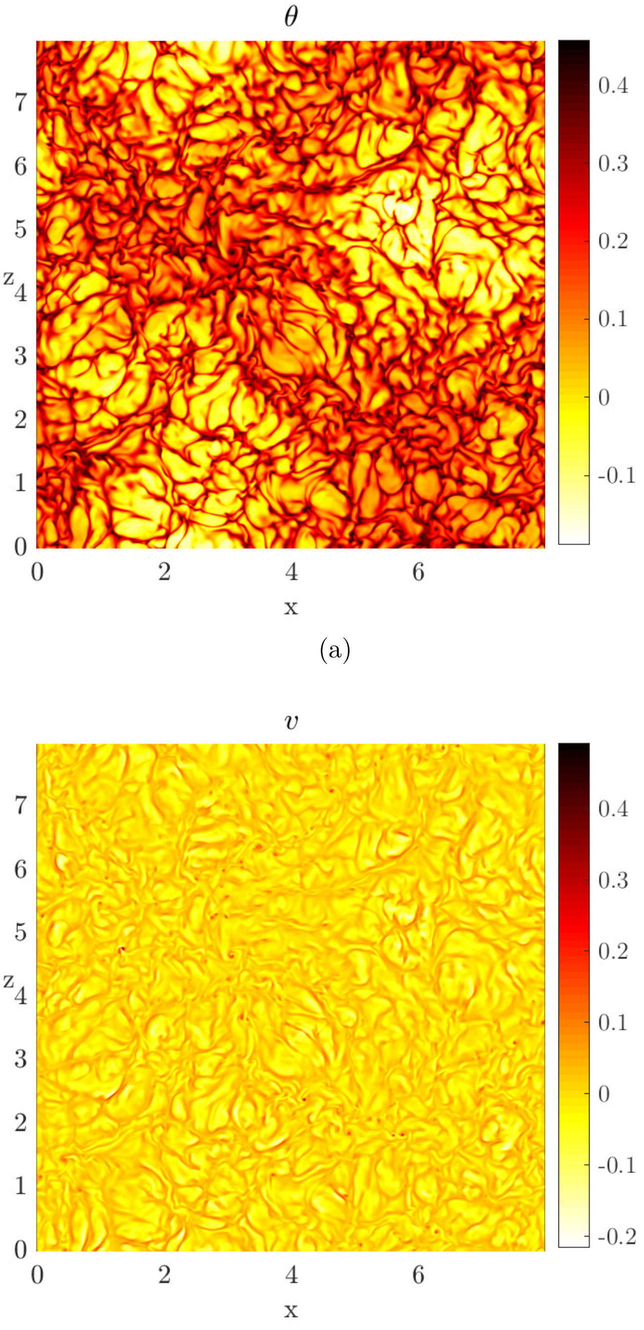

(a)

(b)

Figure 2.13: Instantaneous fields of non-dimensional temperature θ (a) and vertical velocity v (b) on the horizontal section at $y = \delta_\theta = 0.023$. Case AIR.

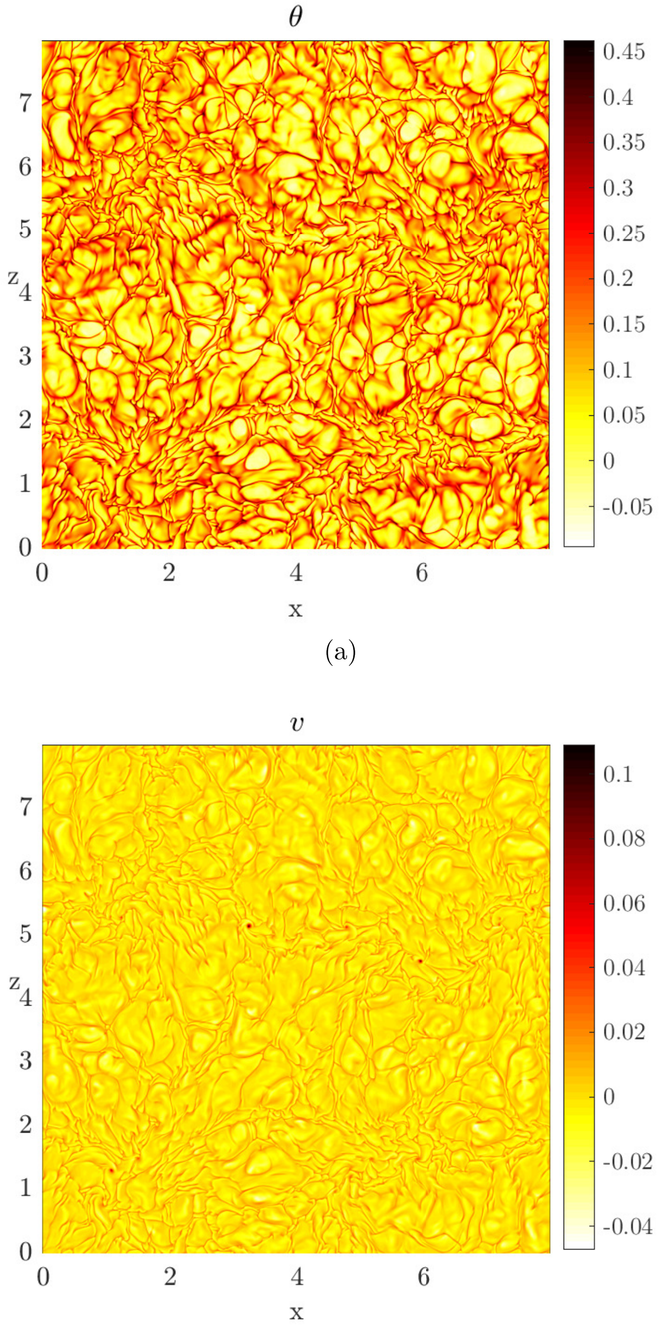

(a)

(b)

FIGURE 2.14: Instantaneous fields of non-dimensional temperature θ (a) and vertical velocity v (b) on the horizontal section at $y = \delta_\theta = 0.011$. Case WAT.

wall distance	LME	AIR	WAT
$0.5\,\delta_\theta$	0.384	0.127	0.102
δ_θ	0.503	0.117	0.056
$2\,\delta_\theta$	0.685	0.111	0.039
$3\,\delta_\theta$	0.805	0.117	0.038
$5\,\delta_\theta$	0.911	0.132	0.043

TABLE 2.9: Plumes width computed as two times λ (equation (2.31)) at vertical heights multiple of the thermal boundary layer thickness in the configurations studied.

considered.

The autocorrelation functions in AIR and WAT configurations (shown in figures 2.16 and 2.17) feature a sudden change in derivative. This is particularly evident in the autocorrelations of temperature fluctuations and suggests that the flow in these configurations has a dual behaviour. For small separations the flow features a high but fast-decaying correlation, while at large separations the slowly-decaying autocorrelation coefficients indicate the presence of large scale motions. Finally, it should be noted that figures 2.15, 2.16 and 2.17 indicate that fluctuations in velocity and temperature fields remain correlated along the homogeneous directions despite a correlation distance of four times the cell height. For future calculations enlargements of the computational domain should be considered.

Thermal plumes can be investigated by studying the divergence of the bidimensional velocity field in horizontal planes div_π

$$div_\pi = \frac{\partial u}{\partial x} + \frac{\partial w}{\partial z} \tag{2.32}$$

as proposed by Togni et al. (2015). Positive values of div_π indicate a divergence of the flow field parallel to the walls, *i.e.* plume impingement, while negative values denote the characteristic flow convergence of plume ejection. To analyse separately the contributions of impingement from those of ejection figure 2.18 shows profiles of the conditional statistics $\langle div_\pi \rangle^+ = \langle div_\pi \rangle$ if $div_\pi > 0$ and $\langle div_\pi \rangle^- = \langle div_\pi \rangle$ when $div_\pi < 0$, plotted as functions of the distance from the walls scaled by the thermal boundary layer thickness. It appears that in configurations LME and AIR the maximum impingement occurs slightly closer to the walls with respect to the distance of maximum ejection, as noted by Togni et al. (2015) at $Pr = 0.7$. On the other hand in configuration WAT the opposite

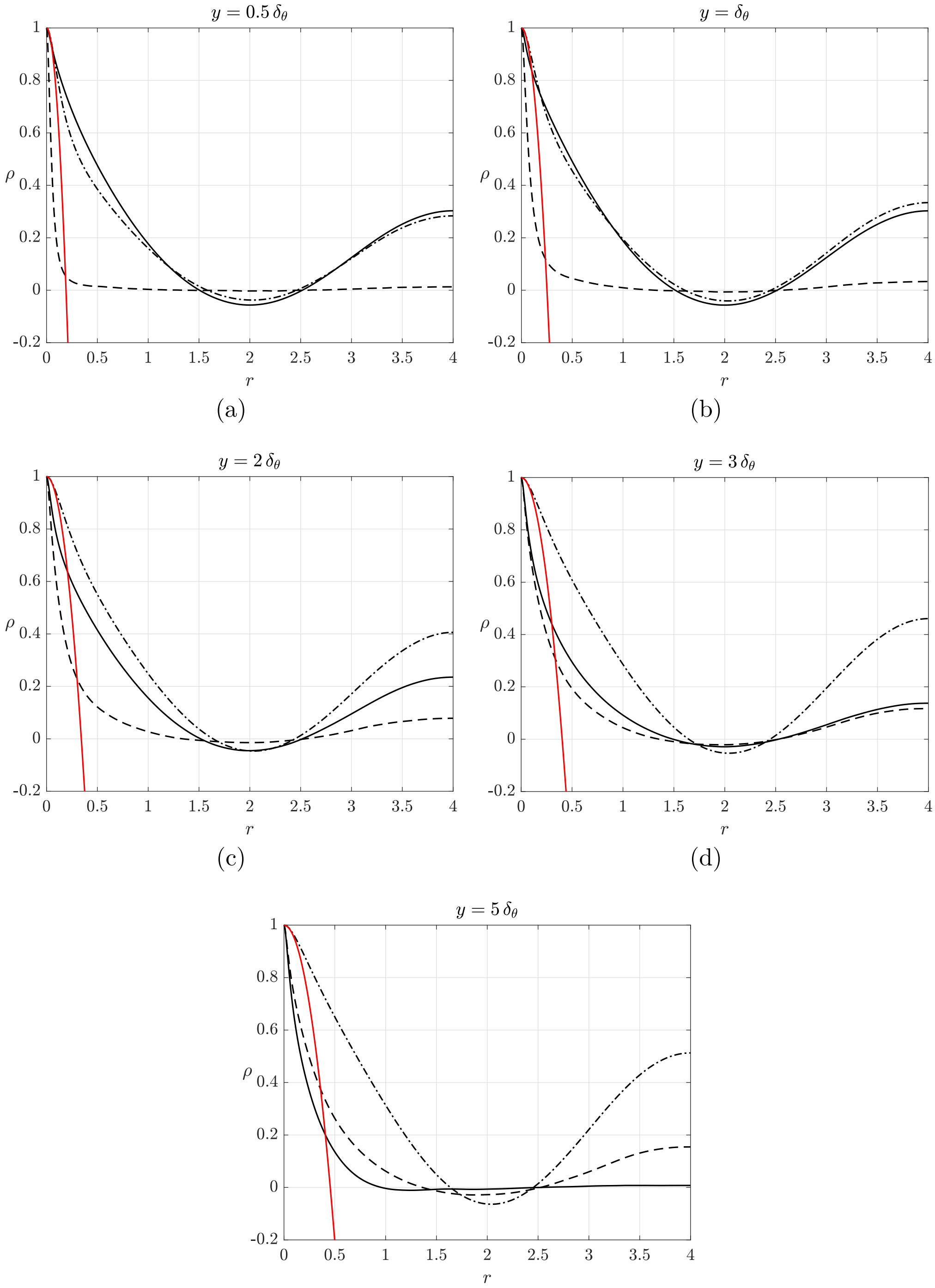

(a) (b)

(c) (d)

(e)

FIGURE 2.15: Spatial autocorrelation function of temperature fluctuations (− · −), horizontal (——) and vertical (− − −) velocity components at different vertical heights in configuration LME. The red line indicates the parabola osculating ρ_θ at $r = 0$.

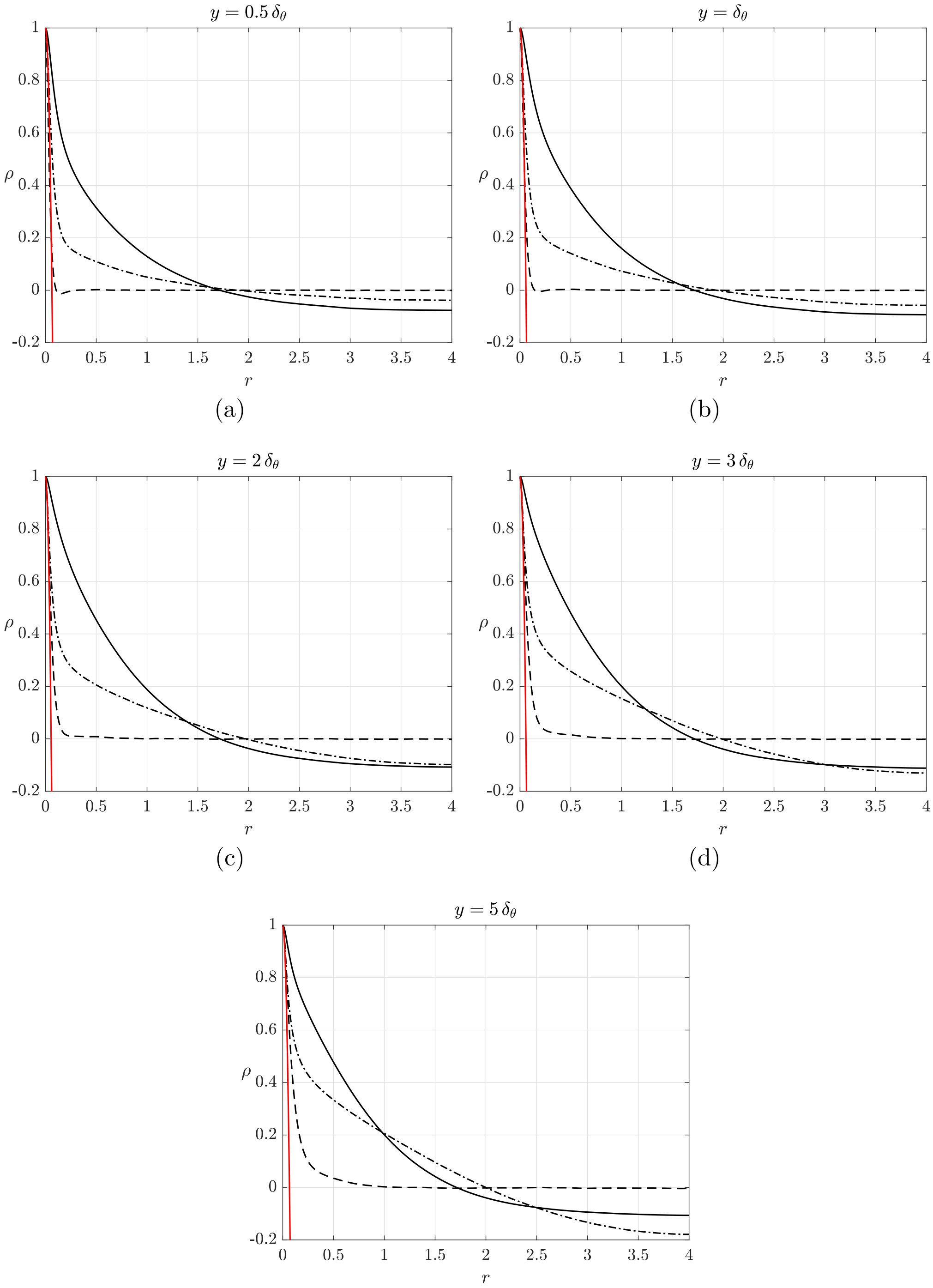

(a) (b) (c) (d) (e)

FIGURE 2.16: Spatial autocorrelation function of temperature fluctuations ($- \cdot -$), horizontal (——) and vertical ($- - -$) velocity components at different vertical heights in configuration AIR. The red line indicates the parabola osculating ρ_θ at $r = 0$.

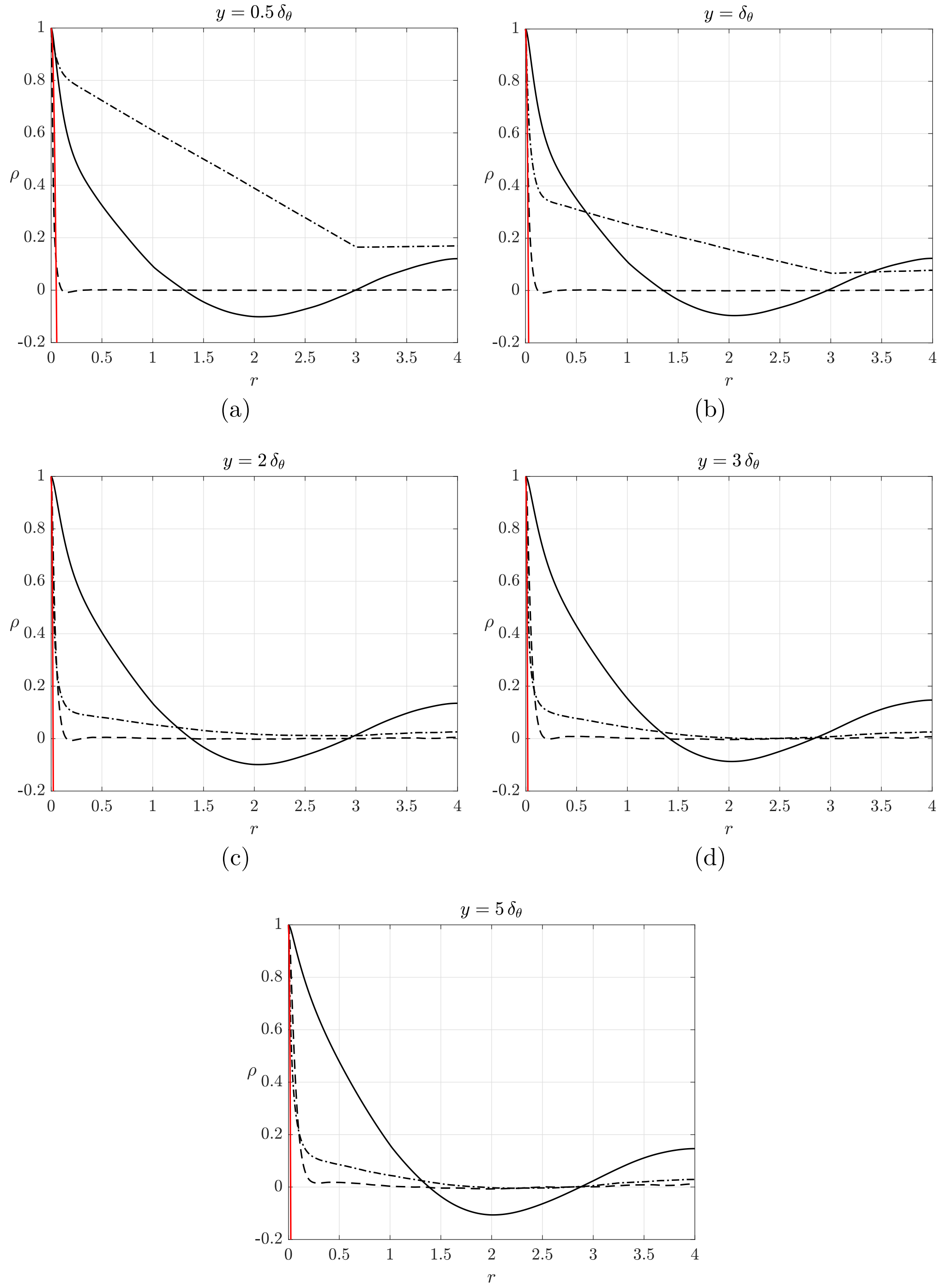

(a) (b) (c) (d) (e)

Figure 2.17: Spatial autocorrelation function of temperature fluctuations (− · −), horizontal (——) and vertical (− − −) velocity components at different vertical heights in configuration WAT. The red line indicates the parabola osculating ρ_θ at $r = 0$.

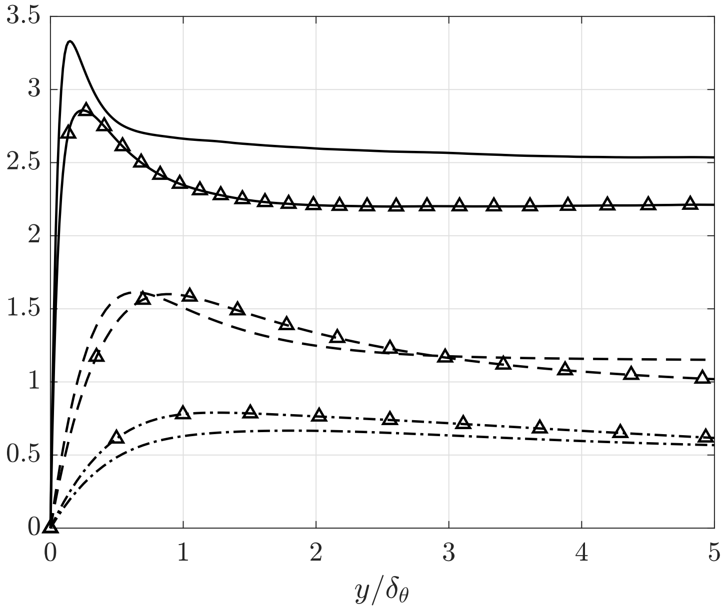

FIGURE 2.18: Profiles of the conditional statistics $\langle div_\pi \rangle^+$ (no symbols) and $\langle div_\pi \rangle^-$ (symbols △) in LME (——), AIR (− − −) and WAT (− · −) cases. Plots are presented as functions of the scaled vertical coordinate y/δ_θ and are limited to range $y/\delta_\theta \in [0, 5]$ to focus on the region close to the walls.

occurs, maximum impingement is located further from the walls with respect to maximum ejection. In addition at $Pr = 0.7$ peaks of impingement and ejection curves are almost equal. This is not verified in the other two cases, at $Pr = 0.025$ impingement is more vigorous than ejection, while at $Pr = 7$ the opposite applies.

2.5.2 Single-point statistics

The analysis of single point statistics is of fundamental importance in order to topologically describe the flow. Figure 2.19 displays the average temperature profiles together with vertical lines indicating the thermal boundary layer thicknesses. It is evident that the region where thermal diffusion dominates over turbulent heat transfer, *i.e.* the thermal boundary layer in which the gradient $d\langle\theta\rangle/dy$ is large, has a very different extension in configurations considered.

Profiles of the root-mean-square velocity fluctuations are shown in figure 2.20. The peaks of maximum fluctuations intensity for the horizontal velocity component occur almost at the same distance from the walls in configuration studied. As already mentioned in section 2.4.3 this is deemed to be due to the constant Grashof number in simulations presented. By defining the velocity boundary layer thickness as the wall distance at which these peaks are observed, as suggested by van Reeuwijk et al. (2008a), one concludes that the three cases are characterised by the same boundary layer thickness. However the intensity of velocity fluctuations scaled by the free-fall velocity is quite different. Fluctuations in LME configuration are characterised by almost twice the intensity of fluctuations in AIR, which in turn are almost two times as intense as those in WAT case. This occurs because of the different Prandtl number since, as reported also by van Reeuwijk et al. (2008a), at different Rayleigh number the intensity of the peak of horizontal velocity fluctuations is the same. Varying Ra only the wall distance of this peak changes. The higher intensities of horizontal velocity fluctuations in low-Prandtl-number conditions indicates that in such condition the “wind of turbulence” is more vigorous than at higher Pr values. Moreover the velocity boundary layer behaves like a two dimensional layer since the wall-normal fluctuations are very small close to walls, see Togni et al. (2015) for a more detailed description of the spatial redistribution of turbulent kinetic energy.

Profiles of non-dimensional temperature fluctuations are shown in figure 2.21 and are plotted as functions of the vertical coordinate scaled by the thermal boundary layer thickness. Despite the highly-diffusive temperature field (figure 2.12(a)), temperature fluctuations are more intense in configuration LME with respect to AIR and WAT. It can be concluded that in constant-Grashof-number conditions the lower is the Prandtl number the higher are temperature and velocity fluctuations intensities when scaled over conventional quantities ΔT and U_{ff}. Others and probably more appropriate scalings may modify the outcome of such comparison. In addition, as shown in the inset, fluctuations peaks are observed close to the edge of the thermal boundary layer in all configurations studied. In configuration LME maximum fluctuations occurs slightly further from the walls, while in AIR and WAT cases peaks are observed closer to the wall than δ_θ.

The behaviour of thermal plumes can be studied more in detail by means of skewness and kurtosis of the flow variables. The values of skewness S and kurtosis K allow to gain information about the shape of the Probability Density Functions (PDFs) of a random variable. These statistical quantities are the third- and fourth-order moments of fluctuating variable ϕ' normalised by its variance

$$S = \frac{\langle \phi'^3 \rangle}{\langle \phi'^2 \rangle^{3/2}} \qquad K = \frac{\langle \phi'^4 \rangle}{\langle \phi'^2 \rangle^{2}} \tag{2.33}$$

Skewness S provides information about the symmetry of PDF. Symmetric PDFs will have zero skewness (and all the other higher-order odd moments will be zero),

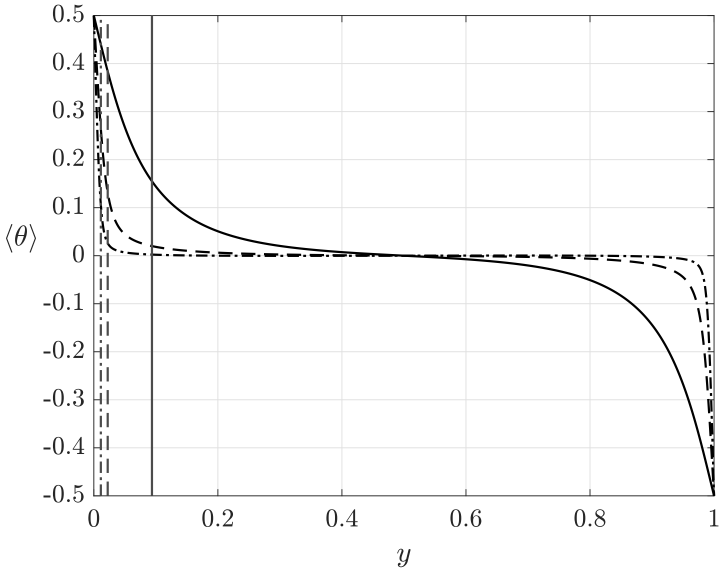

FIGURE 2.19: Average temperature profiles in configurations LME (——), AIR (− − −) and WAT (− · −). Vertical lines indicate the thickness of the thermal boundary layer on the bottom wall.

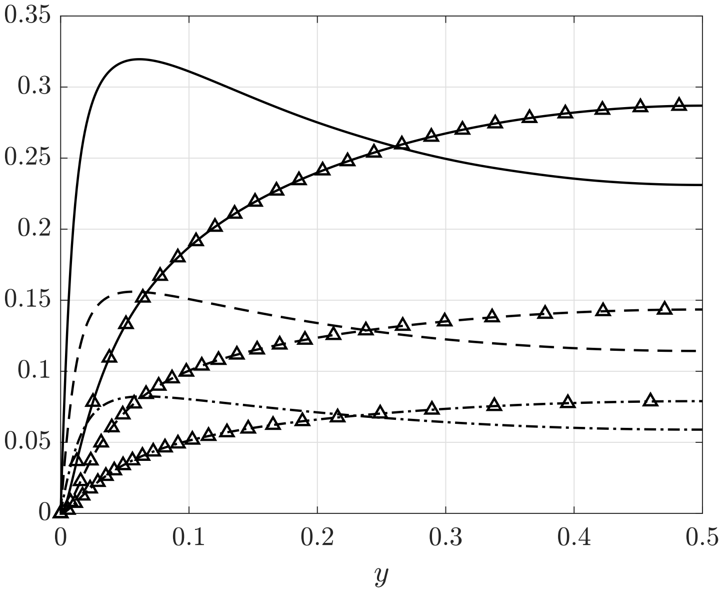

FIGURE 2.20: Standard deviations of velocity fluctuations in configurations LME (——), AIR (−−−) and WAT (−·−). Lines without symbols represent the horizontal velocity fluctuations $(u_{rms} + w_{rms})/2$, while symbols $\triangle$ indicates v_{rms}.

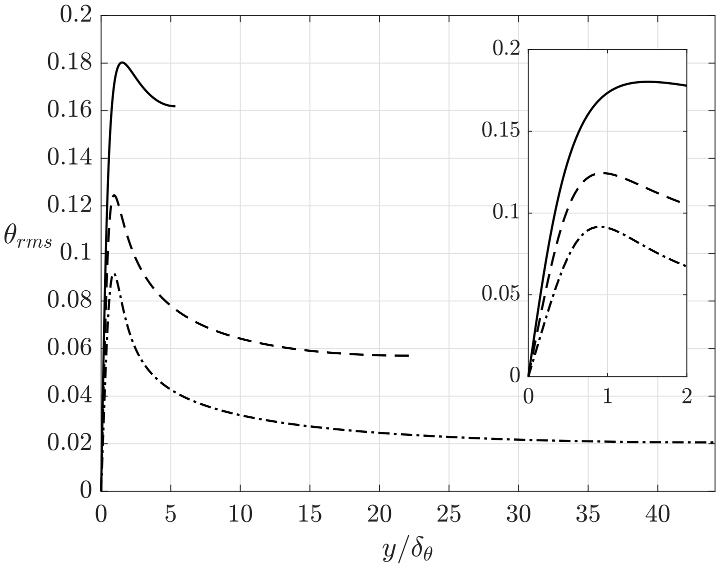

FIGURE 2.21: Standard deviation of temperature fluctuations plotted as function of y/δ_θ in configurations LME (——), AIR (− − −) and WAT (− · −). The inset focuses on the region close to the walls, $y/\delta_\theta \in [02]$

while a positive skewness indicates that ϕ' is more likely to assume values larger than the mean $\langle\phi\rangle$ with respect to values below the mean or, in other words, the PDF of ϕ is skewed towards values higher than the mean. On the other hand the kurtosis K indicates the flatness of a PDF. A PDF with high K has long tails which means that extreme and intermittent events take place. On the contrary low values of K are symptomatic of a PDF clustered around the mean value. In fluid dynamics S and K are often used to compare the PDF of flow variables with the values of the Gaussian (or "normal") distribution, which is characterised by $S = 0$ and $K = 3$.

Profiles of skewness and kurtosis of velocity components, pressure and temperature in the configurations studied are reported in figures 2.22, 2.23 and 2.24, plotted as functions of the vertical coordinate scaled by the thermal boundary layer thickness y/δ_θ. Due to statistical isotropy in horizontal planes skewness and kurtosis of velocity components along x and z directions are averaged together and hereafter they will be referred to as S_u and K_u. At mid-channel height, in each configuration, almost every variable is normally distributed as S and K approach values respectively close to 0 and 3. The only exception concerns pressure in LME and AIR cases, where S_p is negative, and temperature in WAT configuration, being $K_\theta > 3$. The PDF of the horizontal velocity component is symmetric in every configuration ($S_u = 0$) in the entire fluid layer, while close to the walls

K_u denotes that intermittent extreme events occur. This is the footprint of impingement as impinging plumes originate fluctuations which are symmetrical and far from the mean.

The PDFs of vertical velocity v and temperature θ are very different from the Gaussian distributions. Close to the walls $S_v < 0$ and $K_v >> 3$ in LME and AIR configurations indicating that v intermittently assumes large negative values by extreme events. Once again this denotes plumes impingement on the walls as negative vertical velocity fluctuations indicate the presence of cold plumes coming from the upper wall. Interestingly in WAT configuration a different situation is observed, skewness of the vertical velocity component is positive, while the kurtosis remains larger than the normal value. Hence v tends to take positive values which are statistically closer to the mean with respect to other configurations, denoting that in WAT configuration, close to the walls, plumes emission is more likely to occur with respect to impingement. The tendency of emission to prevail over impingement has been already observed in section 2.5.1, see figure 2.18.

As noted by Togni et al. (2015) skewness of temperature fluctuations is negative at walls, crosses the x-axis and assumes the Gaussian value at mid channel in every configuration. Almost at the same vertical coordinate of the sign change in S_θ, K_θ exhibits a minimum and this occurs about the edge of the thermal boundary layer, from about $0.7\delta_\theta$ in WAT configuration to $1.4\delta_\theta$ in LME case. Moreover whereas in LME and AIR configurations temperature kurtosis assume the normal value 3, indicating that the intermittent events related to the ascending and descending plumes are balanced, in WAT case a large kurtosis is observed. This indicates that symmetrical and extreme temperature fluctuations are likely to be recorded in WAT case at half channel.

Finally skewness and kurtosis of pressure are analysed. The kurtosis K_p shows a small deviation from the Gaussian value throughout the fluid layer, while the skewness S_p in LME and AIR is positive at the walls and negative at mid-channel. Such values indicates the deceleration of plumes at walls by means of positive pressure fluctuations (Wörner and Grötzbach, 1998) whereas at $y = 0.5$ they suggest that negative but not-so-extreme events take place, which may be related to plumes suction in the bulk region. On the contrary in WAT case S_p is everywhere non-negative pointing out that in these conditions plumes suction is not as vigorous as in LME and AIR.

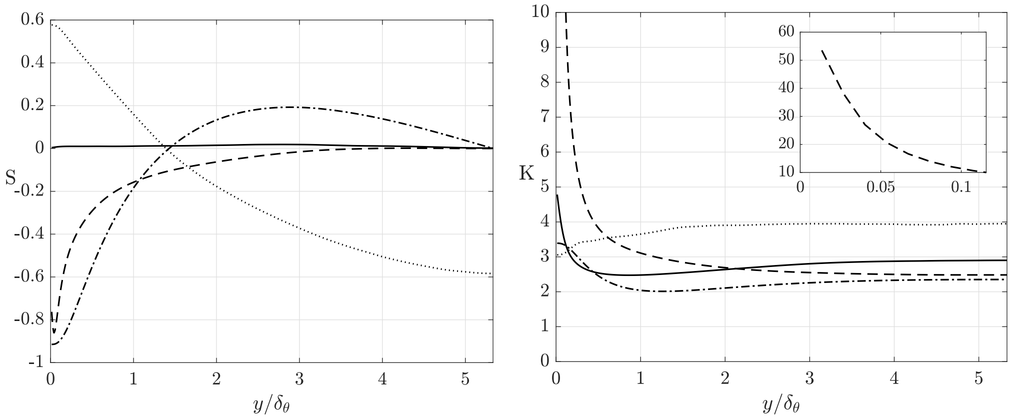

(a) (b)

FIGURE 2.22: Skewness (a) and kurtosis (b) of horizontal velocity component (——), vertical velocity (— — —), temperature (— · —) and pressure (· · ·) in LME configuration. Profiles are plotted as functions of y/δ_θ. The inset displays the values of K_v close to the walls.

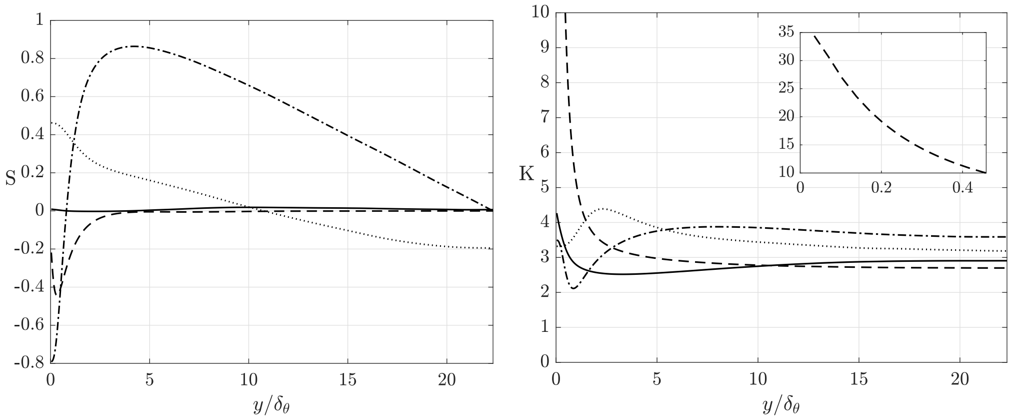

(a) (b)

FIGURE 2.23: Skewness (a) and kurtosis (b) of horizontal velocity component (——), vertical velocity (— — —), temperature (— · —) and pressure (· · ·) in AIR configuration. Profiles are plotted as functions of y/δ_θ. The inset displays the values of K_v close to the walls.

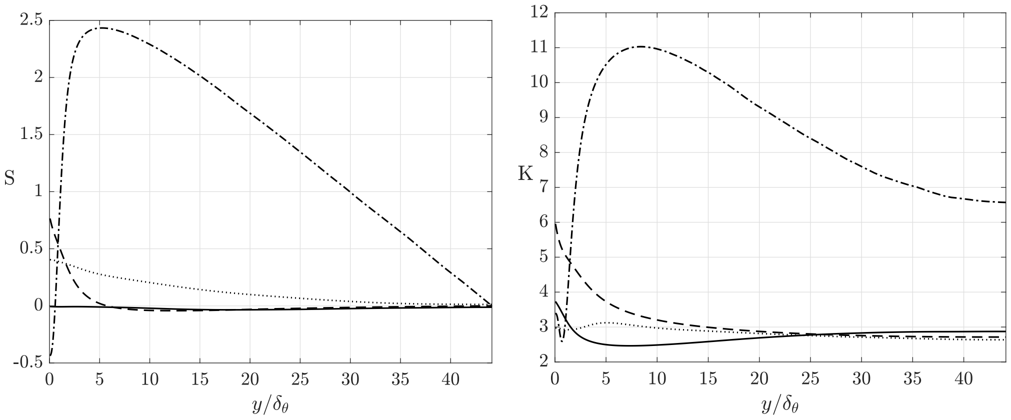

(a) (b)

FIGURE 2.24: Skewness (a) and kurtosis (b) of horizontal velocity component (——), vertical velocity (– – –), temperature (– · –) and pressure (· · ·) in WAT configuration. Profiles are plotted as functions of y/δ_θ.

2.5.3 Distribution of turbulent kinetic energy and temperature variance

To characterise the distribution of turbulent kinetic energy and temperature variance the relative balance equations are analysed. The budget equation of turbulent kinetic energy reads

$$-\frac{d\langle kv'\rangle}{dy}-\frac{d\langle v'p'\rangle}{dy}+\frac{1}{\sqrt{Gr}}\frac{d^2\langle k\rangle}{dy^2}+\langle v'\theta'\rangle-\langle\,\tilde{\varepsilon}\,\rangle=0 \tag{2.34}$$

where $k=\left(u_i'\,u_i'\right)/2$ is the local, instantaneous turbulent kinetic energy. The first three terms of equation (2.34) represent inertial, pressure and viscous transports of turbulent kinetic energy, while $\langle v'\theta'\rangle$ accounts for production due to buoyancy and $\langle\tilde{\varepsilon}\rangle$ is the average pseudo-dissipation of turbulent kinetic energy, see equation (2.27). In section 2.4.4 it has been shown that the pseudo-dissipation of turbulent kinetic energy $\tilde{\varepsilon}$ approximates well the dissipation of turbulent kinetic ε, see figure 2.6.

Figures 2.25, 2.26 and 2.27 display profiles of the terms in equation (2.34) scaled by $\langle\tilde{\varepsilon}'\rangle_V=(Nu-1)//\sqrt{Ra\,Pr}$ (see equation (2.7)) and plotted as functions of y/δ_u. The dissipation term is not reported as it is very similar in configurations studied. The values of δ_u considered are computed following Shishkina et al. (2010), see equation (2.22). In Togni et al. (2015), where convection at $Pr=0.7$ and $Ra=10^5-10^7$ is studied, three regions are identified. Close to the walls a viscous layer is observed, and this region is bounded by the vertical coordinate at which the pressure transport equals the viscous one. There a transitional layer starts and it extends towards the region at which pressure transport equals production. From this vertical position the bulk region begins. It is worth to notice that at every Prandtl number involved in the present study these three regions exist, at least at the Rayleigh numbers considered. In figure 2.28, where the budget terms of different configurations are compared, it appears that the viscous layer has almost the same thickness in all configurations, $y/\delta_u \simeq 0.2 - 0.35$. On the other hand the transitional layer extension is similar in configurations AIR and WAT, up to $y/\delta_u \simeq 2.1 - 2.4$, while it differs significantly in LME where it is bounded at $y/\delta_u \simeq 3.5$. This occurs because production at low Prandtl and Rayleigh numbers grows far from the walls when compared to the other two cases. Moreover, when scaled over $\langle \tilde{\varepsilon}' \rangle_V$, production terms as well as inertial and viscous transports are very similar in the configurations studied. Only the pressure transport assumes values which are larger in LME with respect to AIR and WAT, see figure 2.28. Such a difference is related to the very strong pressure fluctuations in the liquid mercury configuration, indicating that plumes impingement is more vigorous than in other cases, see also the discussion about skewness and kurtosis in section 2.5.2.

To complete the description of energy transfers in RBC also the budget of average temperature variance has to be considered. The balance equation for $\langle \theta'^2 \rangle$ is

$$-\frac{d\langle v'\theta'^2\rangle}{dy} + \frac{1}{\sqrt{Gr}\,Pr}\frac{d^2\langle \theta'^2\rangle}{dy^2} - 2\langle v'\theta'\rangle\frac{d\langle\theta\rangle}{dy} - 2\langle\varepsilon_\theta\rangle = 0 \qquad (2.35)$$

The first and second terms represent respectively inertial and diffusive transports, while the third and the last ones are a source and a sink, hereafter called production and dissipation. $\langle\varepsilon_\theta\rangle$ is the average rate of temperature variance dissipation

$$\langle\varepsilon_\theta\rangle = \frac{1}{\sqrt{Gr}\,Pr}\left\langle \frac{\partial\theta'}{\partial x_i}\frac{\partial\theta'}{\partial x_i}\right\rangle \qquad (2.36)$$

The terms of the temperature variance equation (2.35) in configurations LME, AIR and WAT are shown in figures 2.29, 2.30 and 2.31. The topological analysis reported in Togni et al. (2015) divides the fluid layer in a diffusive region close to the wall, a transitional layer and a bulk zone. The former extends towards the coordinate at which the production term equals diffusion, further from the wall the transitional layer starts. The separation between transitional and bulk regions is identified where production equals the inertial transport. Again, the regions described in such analysis applies also to present cases, the only exception

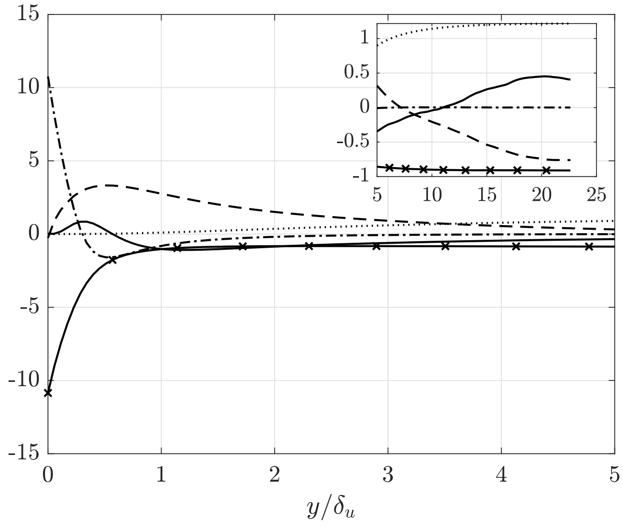

FIGURE 2.25: Budget of turbulent kinetic energy in configuration LME: inertial (——), pressure (− − −), viscous (−·−) transports; production (···) and dissipation (×). x- and y-axis are scaled respectively over the velocity boundary layer thickness δ_u and the volume averaged pseudo-dissipation rate of kinetic energy $\langle\tilde{\varepsilon}'\rangle_V$. In the inset are shown details of the central region.

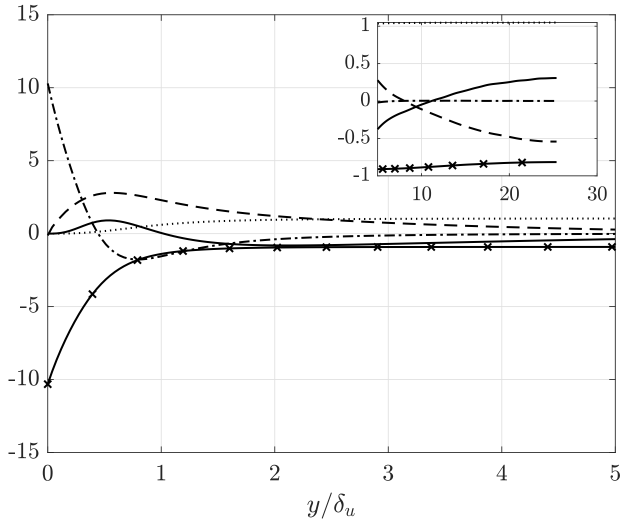

FIGURE 2.26: Budget of turbulent kinetic energy in configuration AIR: inertial (——), pressure (− − −), viscous (−·−) transports; production (···) and dissipation (×). x- and y-axis are scaled respectively over the velocity boundary layer thickness δ_u and the volume averaged pseudo-dissipation rate of kinetic energy $\langle\tilde{\varepsilon}'\rangle_V$. In the inset are shown details of the central region.

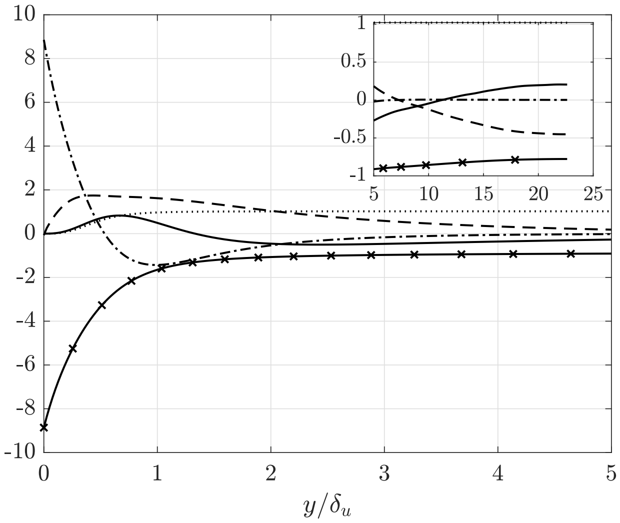

FIGURE 2.27: Budget of turbulent kinetic energy in configuration WAT: inertial (——), pressure (– – –), viscous (–·–) transports; production (···) and dissipation (×). x- and y-axis are scaled respectively over the velocity boundary layer thickness δ_u and the volume averaged pseudo-dissipation rate of kinetic energy $\langle\tilde{\varepsilon}'\rangle_V$. In the inset are shown details of the central region.

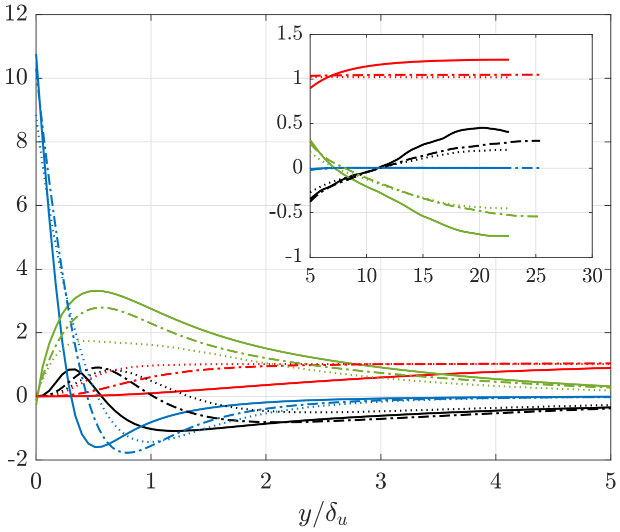

FIGURE 2.28: Comparison of terms in turbulent kinetic energy equation (2.34) between configurations studied: LME (——), AIR (– · –) and WAT (···). Red lines indicate production while green, blue and black stands for pressure, viscous and inertial transports. Axes are scaled as in figures 2.25, 2.26 and 2.27.

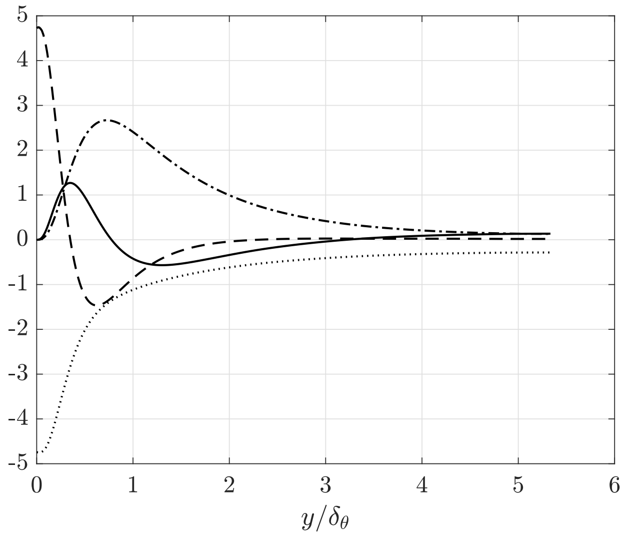

FIGURE 2.29: Budget of temperature variance in configuration LME: inertial (——) and diffusive (− − −) transports; production (− · −) and dissipation (· · ·). x- and y-axis are scaled respectively over the thermal boundary layer thickness δ_θ and the volume averaged rate of temperature dissipation $\langle \tilde{\varepsilon_\theta}' \rangle_V$.

might be represented by LME where the bulk region is confined to a very small portion around $y = 0.5$. This indicates that the topological analysis presented in Togni et al. (2015), as well as the description of the self-sustained motion cycle, might be considered relevant for a wide range of Ra and Pr.

Figure 2.32 compares profiles of terms in temperature variance equation in configurations studied. It appears that scaling the wall distance over the thermal boundary layer thickness δ_θ allows to superimpose peaks of each term in equation (2.35). For distances from the walls larger than $3\,\delta_\theta$ each term is shown to be almost constant suggesting that, just like the turbulent kinetic energy budget (figure 2.28), sufficiently far from the walls the flows display homogeneous characteristics.

In addition figure 2.32 shows that when scaled over the thermal dissipation rate $\langle \tilde{\varepsilon_\theta}' \rangle_V = Nu/\sqrt{Ra\,Pr}$ (see equation (2.7)) the magnitude of terms in LME are in general smaller than terms in AIR and WAT. In these two latter configurations diffusive transport and dissipation are very similar, while production term and inertial transport are quite different: in WAT case production and inertial terms are larger in magnitude with respect to configuration AIR. This means that in WAT configurations there is a higher surplus of temperature variance, and this is transported by inertial effects towards the bulk region.

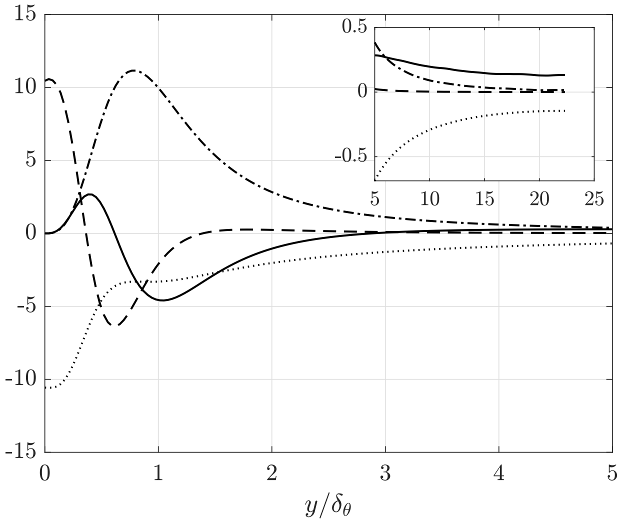

FIGURE 2.30: Budget of temperature variance in configuration AIR: inertial (——) and diffusive (— — —) transports; production (— · —) and dissipation (· · ·). x- and y-axis are scaled respectively over the thermal boundary layer thickness δ_θ and the volume averaged rate of temperature dissipation $\langle \tilde{\varepsilon_\theta}' \rangle_V$. In the inset are shown details of the central region.

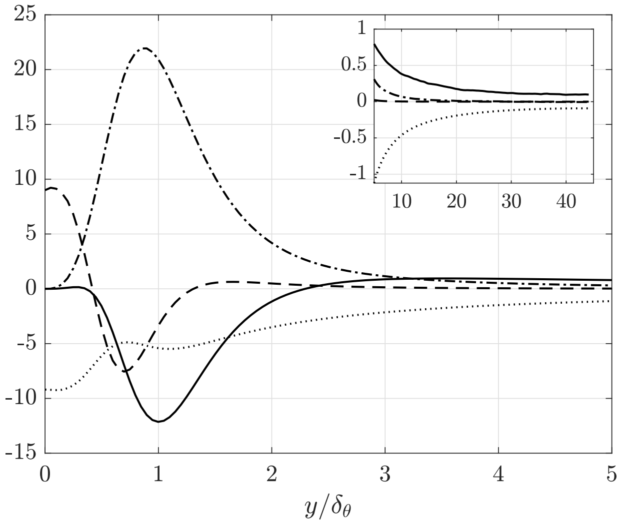

FIGURE 2.31: Budget of temperature variance in configuration WAT: inertial (——) and diffusive (— — —) transports; production (— · —) and dissipation (· · ·). x- and y-axis are scaled respectively over the thermal boundary layer thickness δ_θ and the volume averaged rate of temperature dissipation $\langle \tilde{\varepsilon_\theta}' \rangle_V$. In the inset are shown details of the central region.

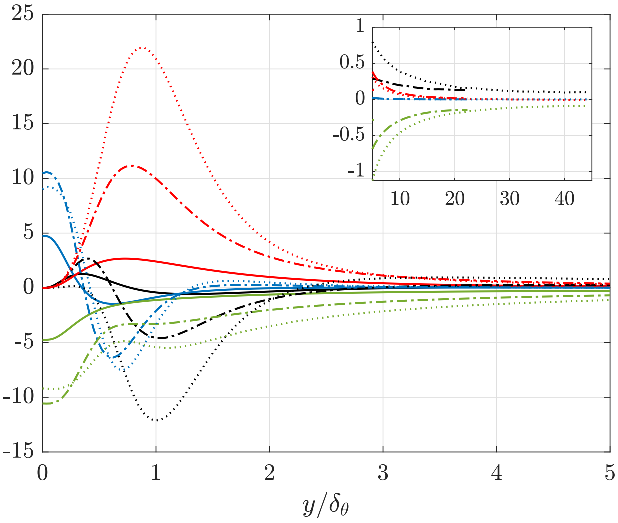

FIGURE 2.32: Comparison of terms in temperature variance equation (2.35) between configurations studied: LME (——), AIR (−·−) and WAT (···). Blue and black lines indicate diffusive and inertial transports, while red and green lines stand for production and dissipation. Axes are scaled as in figures 2.29, 2.30 and 2.31.

3 Triple jet

3.1 Introduction

Combustion chambers of gas turbines and nuclear reactors are just two examples of the role of entrainment and mixing between buoyant streams in industrial applications (Pitz et al., 2019; Shams et al., 2019a). Such phenomena are observed also in several flows of environmental interest, for example pollutant emissions in the atmosphere (Marro et al., 2014) and waste-water discharge from pipes into lakes (Bleninger and Jirka, 2008).

In nuclear reactors mixing of streams at different temperatures occurs in the upper plenum of reactors core where the heat generated within fuel assemblies by fission processes is transported to a coolant which, in the latest generation of reactors, is a liquid metal or a molten salt (Fazio et al., 2015). Reactors of this kind are named Liquid Metal Fast Reactors (LMFRs) and after the Fukushima nuclear disaster on March 2011 they have been extensively investigated as they are inherently safe in case of electric power failures. In such scenarios the large amount of liquid metal surrounding the fuel rods adsorbs the decay heat, which is exchanged by means of natural convection, and undergoes a significant expansion, causing a passive shutdown of the fission process. However, due to the high thermal diffusivity of the employed coolants, temperature fluctuations are readily transmitted to the nearby walls, leading to subsequent expansions and contractions in the containement structure, inducing thermal fatigue cycles which might cause structural failures. In reactor thermal-hydraulics this phenomenon is named thermal striping (Brunings, 1982).

Thermal striping is investigated in a reference configuration which involves three submerged jets at different temperatures, vertically entering a pool from the bottom surface. The experiments by Tokuhiro and Kimura (1999) in water and Kimura et al. (2007) in liquid sodium are the two main benchmarks; both studies aim at reproducing conditions inside LMFR. As observed by Knebel et al. (1998), results obtained with water cannot be directly extended to liquid metals, as turbulent heat transfer at $Pr \ll 1$ is characterised by essentially different features with respect to $Pr > 1$ cases (Otić et al., 2005; Scheel and Schumacher, 2016; Verzicco and Camussi, 1999). On the other hand, experiments with liquid metals suffer from difficulties in local velocity measurements due to the opacity of these fluids (Bremhorst et al., 1989; Schulenberg and Stieglitz, 2010). Besides experiments, a set of numerical simulations is reported by Nishimura and Kimura (2003) and Yu et al. (2017), which perform Unsteady RANS, and in the LES studies by Jung and Yoo (2004), Chacko et al. (2011) and Cao et al. (2012). In general, all these studies compare numerical results with the aforementioned benchmarks in order to assess models prediction of thermal striping. In this context the correct representation of turbulent fluctuations is a key issue (Bremhorst and Krebs, 1992). To the authors knowledge, the only attempt at a Direct Numerical Simulation (DNS) on this topic is reported by Kimura et al. (2002), who compare DNS results against experiments by Tokuhiro and Kimura (1999). However little information is provided on the finite-difference code employed, and on the size of the computational domain in the spanwise direction, where the adopted grid resolution (3 points) suggests that the approach is essentially two-dimensional and arguably should not be considered a DNS. As compared to the experiments, numerical results are in good agreement on the mean quantities, whereas a significant tendency to over-predict second order statistics is observed.

In this chapter results of a Direct Numerical Simulation (DNS) performed on a triple jet configuration, where the central jet is hot and the lateral ones are cold, are presented. The configuration of three planar buoyant jets at different temperatures is by one side suggested by the interest in the study of thermal striping, and on the other side it is expected to clarify the main physical pheneomena underlying entrainment and mixing between buoyant streams. The Reynolds number considered is $Re = 5000$ and Prandtl number is $Pr = 0.031$. The simulated Grashof number is $Gr = 6.25 \times 10^6$ and mixed convection regime is established at a Richardson number is $Ri = Gr/Re^2 = 0.25$. Unlike previous studies where typical values of Ri are $\mathcal{O}(10^{-2})$, buoyancy effects are non-negligible here. The low-Prandtl number has been considered in order to infer about thermal striping phenomena occurring in nuclear plants. As a matter of facts the selected Pr number represents Lead Bismuth Eutectic (LBE) at $T_{\text{ref}} = 220°C$, a liquid alloy envisaged as a coolant inside LMFRs. Beside the aim to understand the physics behind the mixing of buoyant jets, the resulting high-accuracy data allow to provide also reliable statistics on which to develop and validate numerical models for the prediction of turbulent heat transfer in low-Prandtl-number fluids.

Simulations are performed using a customised version of the highly-parallel, high-order and open source code Incompact3d. The original version of the code

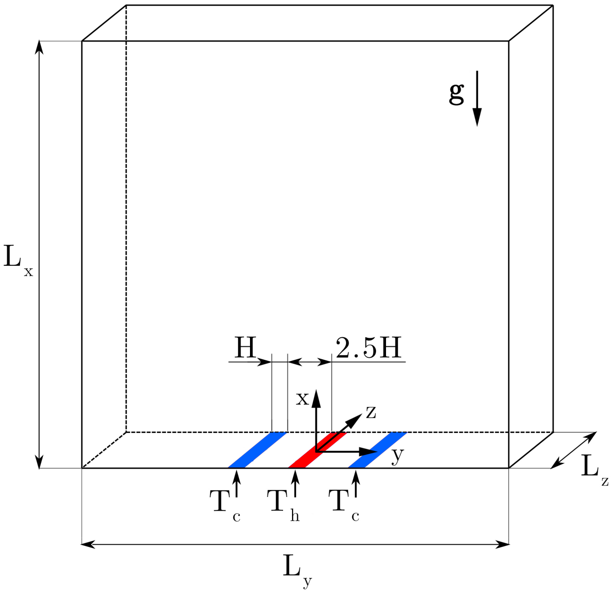

FIGURE 3.1: Three-dimensional representation of the computational domain.

is briefly presented in chapter 1 together with modifications implemented and validation tests.

The present chapter is organised as follows. Section 3.2 describe the triple jet configuration together with the mathematical formulation of the problem, while in section 3.3 are presented the numerical details of the simulation. Finally section 3.4 reports convetional and specifically-developed statistics used to characterise flow and heat transfer features.

3.2 The buoyant triple jet case

The fluid-dynamic case investigated is depicted in figure 3.1 and involves a rectangular pool of liquid metal, where three planar jets are discharged vertically upwards. The jets have the same average centreline velocity U_0 but different temperatures, the central stream is at temperature T_h, while the lateral jets are at $T_c < T_h$. Slots are spaced by 3.5 times their width H, as sketched in figure 3.1.

Mass and momentum equations are solved coupled to the energy equation through the Boussinesq approximation. The problem is made non-dimensional by the jet width H, the time-averaged centreline velocity of the jets U_0 and a reference temperature difference $\Delta T \equiv (T_h - T_{\text{ref}}) - 2\,(T_c - T_{\text{ref}})$. The latter is used in the definition of the normalised, non-dimensional temperature $\theta = \left(T - T_{\text{ref}}\right)/\Delta T$. The system of non-dimensional governing equations reads

$$\begin{gathered}
\frac{\partial u_i}{\partial x_i} = 0 \\
\frac{\partial u_i}{\partial t} + \frac{\partial\, u_i u_j}{\partial x_j} = -\frac{\partial p}{\partial x_i} + \frac{1}{Re}\,\frac{\partial^2 u_i}{\partial x_j\,\partial x_j} + \frac{Gr}{Re^2}\,\theta\,\delta_{i1} \\
\frac{\partial \theta}{\partial t} + \frac{\partial\, \theta u_j}{\partial x_j} = \frac{1}{Pr Re}\,\frac{\partial^2 \theta}{\partial x_j\,\partial x_j}
\end{gathered} \tag{3.1}$$

where $u_1 = u$, $u_2 = v$ and $u_3 = w$ are the streamwise (vertical), cross-flow and spanwise velocity components.

The Reynolds, Grashof and Prandtl numbers are defined as:

$$Re \equiv \frac{U_0\, H}{\nu}\,, \qquad Gr \equiv \frac{g\,\beta\,\Delta T\, H^3}{\nu^2}\,, \qquad Pr \equiv \frac{\nu}{\alpha} \tag{3.2a, b, c}$$

where kinematic viscosity, thermal expansion coefficient and thermal diffusivity of the operating fluid at temperature T_{ref} are indicated by ν, β and α, respectively; g is gravity. A Prandtl number $Pr = 0.031$ is assigned while the Reynolds and Grashof numbers are set to $Re = 5000$ and $Gr = 6.25 \times 10^6$. At a Richardson number $Ri = Gr/Re^2 = 0.25$, buoyancy effects become non-negligible. Notice that the present Re is five times lower than in the PLAJEST experiment (Kimura et al., 2007) and previous numerical studies (Jung and Yoo, 2004; Yu et al., 2017), while Richardson number is an order of magnitude larger than in previous works. Deviations from parameters employed in literature are motivated by the feasibility of a detailed DNS of the flow and the lack of numerical benchmarks on jets mixing in buoyant conditions.

As done in section 2.3 the accurancy of the Boussinesq's approximation has been checked by following the method described in Gray and Giorgini (1976). By considering the reference temperature $T_{\text{ref}} = 220°C$, which allows to set $Pr = 0.031$ and therefore study conditions relevant in nuclear reactor applications, and calculating the thermophysical properties of LBE through correlations available in (Sobolev, 2011), the validity map in figure 3.2 has been obtained. In calculations a 10% of properties variation has been considered allowable. The red dashed line in figure 3.2 represents actual conditions, $Gr = 6.25 \times 10^6$ and $Pr = 0.031$. It appears that Boussinesq's approximation is suited to represent present configuration as the validity region embrace a large portion of the operating curve. The most limiting conditions for the reference length and temperature

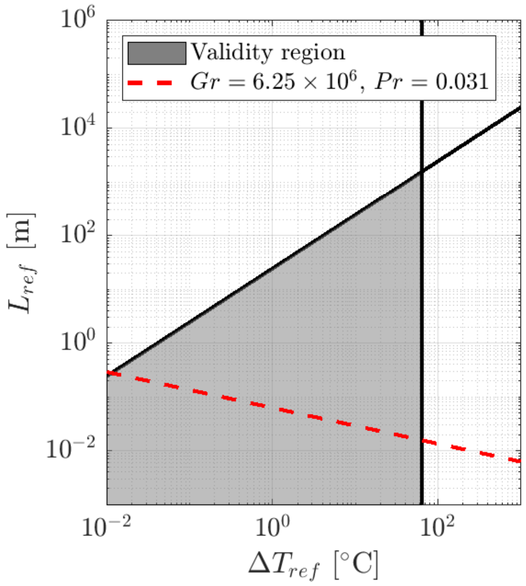

FIGURE 3.2: Validity region of the Boussinesq approximation for LBE constructed using the method by Gray and Giorgini (1976). Reference conditions are $T^0 = 220°$ C and $p^0 = 1$ atm, and a 10% relative variations of thermophysical properties around reference values is admitted.

difference are represented repectively by the condition for neglecting compression work in the energy equation and the variation of viscosity with temperature. Selecting a reference length comparable with the slot height in the experiment by Kimura et al. (2007), $H = 1.5 \times 10^{-2}$m, the selected Grashof number leads to a reference temperature difference $\Delta T = 72.7°$C, for which the Boussinesq approximation holds with a $\sim 12\%$ error related to the sensitivity of viscosity on temperature.

3.3 Numerical method

The set of governing equations (3.1) has been numerically solved using a modified version of the code *Incompact3d* . Modifications have been presented in chapter 1 and include the addition of the Boussinesq's buoyancy term in the momentum equations, a newly-implemented open outflow boundary condition and an inflow strategy to accounts for fully developed conditions at the jet inlets.

The triple buoyant jet simulation is performed on a computational domain of dimensions $L_x \times L_y \times L_z = 30 \times 30 \times 6$. Preliminary studies reported in Angeli et al. (2017) suggest that such dimensions in the vertical and cross-flow directions are suitable for the case under consideration. With particular reference to the cross-flow direction, in Angeli et al. (2017) it is also shown that the choice of periodic boundary conditions, instead of outflow or slip conditions, does not influence the mean flow significantly when a cross-flow extension $L_y = 30$ is considered.

The computational grid accounts for $2049 \times 2048 \times 512$ equally-spaced points, respectively in the streamwise x, cross-flow y and spanwise z directions. The smallest turbulence scales, which in this case are the Kolmogorov length η_K and time scales τ_K, have been computed *a posteriori* on the flow domain from the field of turbulent kinetic energy dissipation rate ε. These results $\eta_K = 3.86 \times 10^{-3}$ and $\tau_K = 7.43 \times 10^{-2}$ and are found at coordinates $(x, y) \approx (1.4, 3.9)$, where $\varepsilon = \varepsilon_{\text{max}}$, corresponding to the external shear layer of lateral, cold jets. Grid spacing along x and y directions equals $\Delta x = \Delta y = 3.8\, \eta_{\text{min}}$, while $\Delta z = 3.0\, \eta_{\text{min}}$. The non-dimensional time step is $\Delta t = 0.0005$ and has been selected on the basis of numerical considerations. Indeed it corresponds to $\Delta t \approx 6.7 \times 10^{-3}\, \tau_{\text{min}}$. According to Moin and Mahesh (1998) the spatial and temporal discretisations employed are demeed sufficient to resolve the smallest scales of motion and temperature.

Periodic boundary conditions are set along the cross-flow and the homogeneous directions, y and z. At the inflow plane ($x = 0$) velocity and temperature are set to zero $u = v = w = \theta = 0$ except for the jet slots, where flow variables are assigned using snapshots recorded from the precursor channel simulation presented in section 1.4. This method is used in order to consider realistic conditions at jet inlets rather than to reproduce turbulent fluctuations employing synthetic methods. At every time step in the precursor channel simulation snapshots are recorded on streamwise-normal sections, which are discretised by $n_y \times n_z = 129 \times 256$ grid points, and are then interpolated onto the $n_y \times n_z = 69 \times 512$ mesh of the jet slots in the triple jet case. Recorded temperature maps are also scaled in order to set the hot jet centreline temperature at $\theta_h = 0.5$, while the lateral jets have $\theta_c = -0.25$. In this way the net inflow of thermal energy is zero. In addition, to avoid the particular condition where the three jets are in phase *i.e.* the same velocity and temperature profiles are set at the three jet inlets at the same time, a phase-shift is introduced between jets. The phase-shift considered is more than twice the integral time scale of the streamwise velocity component, which has been computed using the temporal autocorrelation of such component of velocity. Figure 3.3 display the temporal correlation of u in the precursor channel simulation at different wall distances. It appears that u uncorrelates after a period equal to $\Delta\tau \simeq 12$, the phase-shift considered is $\Delta\tau' \simeq 25$.

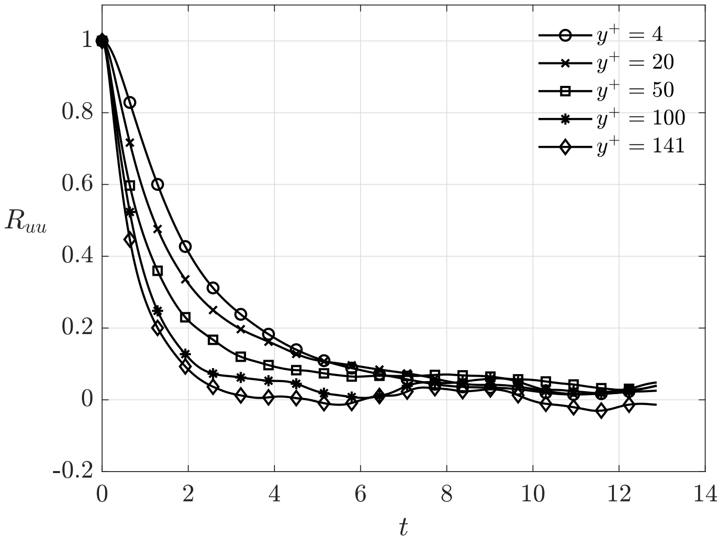

Figure 3.3: Temporal autocorrelation function of the streamwise velocity component in the precursor channel simulation at different wall distances.

Finally, at the outflow plane ($x = L_x$) the open outflow boundary condition presented in section 1.3 is enforced on both the velocity and temperature fields.

3.4 Results

3.4.1 Low-frequency oscillation

Figure 3.4 displays the instantaneous fields of vertical velocity component and temperature on a section normal to the spanwise direction z. Due to the low Prandtl number considered, temperature is mainly diffusive and characterised by large scales, conversely the velocity field exhibits a wide range of scales. For vertical coordinates $x > 8$ the fluid exiting from the three jets is observed to coalesce in a single and almost isothermal stream. In the region close to the inlets three large-scale thermal plumes derived from jet mixing are shown to oscillate in z-planes. Oscillations are associated with a low-frequency cross-flow undulation of the jets and vortex shedding.

This undulatory phenomenon experienced by the three jets can be observed in figure 3.5, where the spanwise-averaged vertical velocity and temperature fields are depicted at two different times. Averaging along the spanwise direction is known to flatten the small scale turbulent fluctuations and to retain and emphasise the main flow unsteadinesses. The cross-flow undulation of the central jet

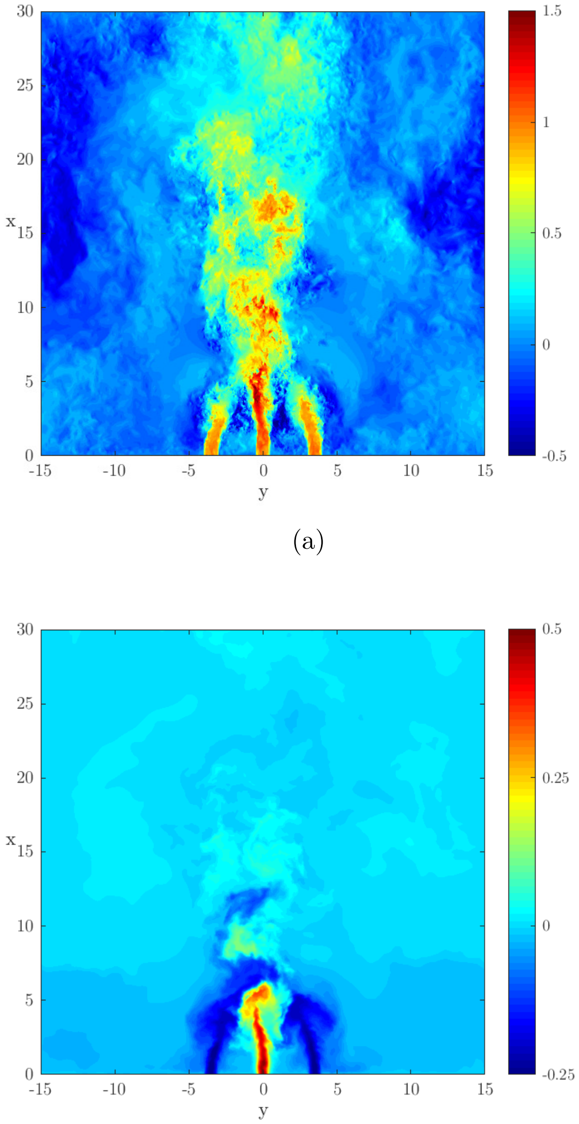

(a)

(b)

FIGURE 3.4: Instantaneous fields on a z-plane: (a) vertical velocity component u; (b) temperature θ.

exhibits two large-scale vortex sheddings per oscillation period. The shedding is systematically observed at the maximum cross-flow inclination (left and right) of the central jet. To quantitatively assess this phenomenon, figure 3.6 displays the frequency spectrum of vertical and cross-flow velocities at $(x, y) = (5.00, 1.75)$. A clear separation of scales is observed with small scale turbulent fluctuations occurring at much larger frequencies than the large-scale oscillation, characterised by a frequency $f = 0.090$ corresponding to a time interval $\Delta\tau = 11.1$. Interestingly, a second peak at an even lower frequency, $f = 0.045$, corresponding to twice the oscillation period, $\Delta\tau' = 22.2$, appears in the turbulent spectrum of figure 3.6. Its intensity is the largest for the vertical velocity component. The analysis of the time evolution of the flow reveals that this is a statistical footprint of vortex shedding also for the lateral jets. It appears that the lateral jets do not shed vortices each time the central jet is inclined towards them. This phenomenon is instead found to occur every two oscillating periods alternatively in the two lateral jets. Due to the simultaneous superposition of shedding of large scale vortices from the lateral and central jets, such a very-low frequency is also the most intense, see figure 3.6. Low frequencies are observed throughout the computational domain and the shedding of large-scale vortices affects the overall flow and heat transfer behaviour.

To characterise the structure of this large-scale unsteadiness of the flow, figure 3.7 displays the spatial correlation function along the z (spanwise) direction for the velocity and temperature fields in $(x, y) = (5.00, 1.75)$. Correlations display an initially steep decrease which is typical of turbulent flows. This decrease lasts up to $r_z \approx 0.5$ for the velocity components and up to $r_z \approx 0.75$ for temperature. Such a difference could be ascribed to the small Prandtl number considered. These spanwise scales represent the decorrelation lengths of the turbulent velocity and temperature fields. By further increasing the spanwise separation r_z, vertical and cross-flow velocities and temperature correlations approach different correlation levels. Only the spanwise velocity component is almost uncorrelated for $r_z \gtrapprox 1$. The non-zero value of the spanwise correlation function for temperature and the vertical and cross-flow velocity components is an unambiguous signature of the shedding of large-scale vortices from the undulating jets. As shown here in quantitative terms, the large-scale instability is essentially a two-dimensional phenomenon, at least for the spanwise domain extent considered in the present study. Investigating whether the low-frequency undulation and shedding of large-scale vortices remains or not a two-dimensional phenomenon over larger spanwise lengths exceeds the computational resources available and goes beyond the main

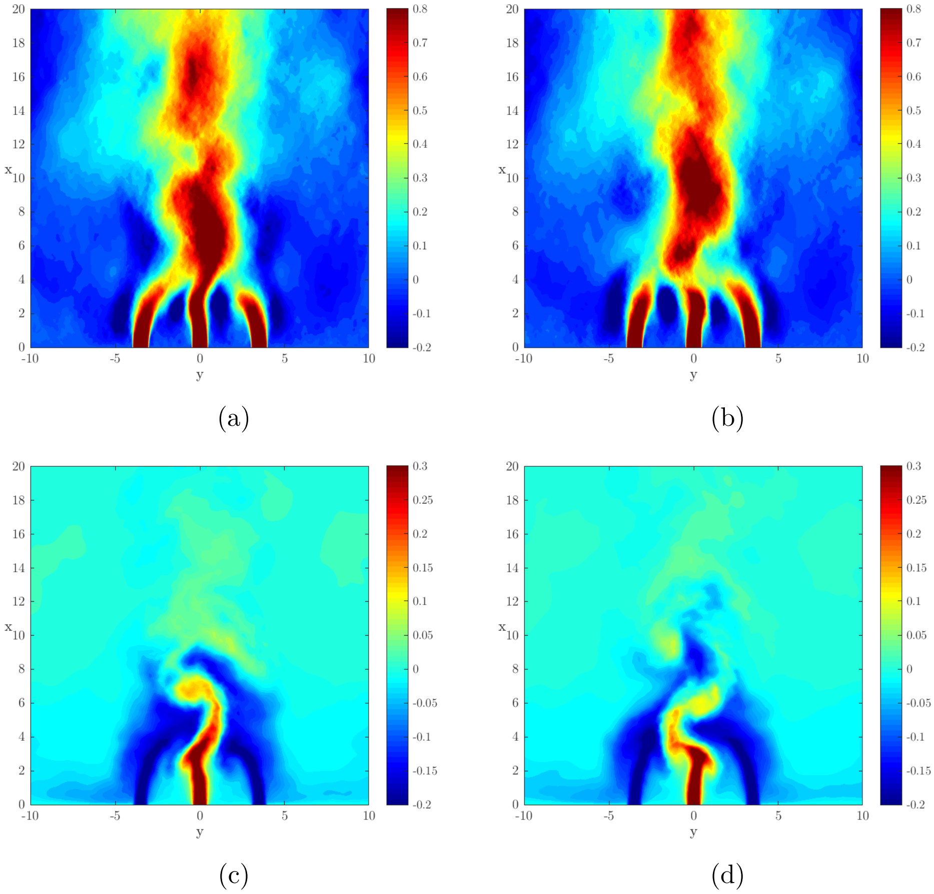

(a) (b)

(c) (d)

FIGURE 3.5: Spanwise-averaged fields at two different time instants: vertical velocity component, (a) and (b); temperature, (c) and (d).

purpose of the present work.

3.4.2 Statistics

After a statistical steady state is achieved, statistics are calculated by averaging in time for a non-dimensional time span $\Delta\tau = 110$ and along the homogeneous direction z. Also symmetry or anti-symmetry of variables about $y = 0$ plane is exploited. In order to reduce the errors due to the enforcement of the boundary condition at the outflow plane statistics are presented in the region $(x, y) \in [0, 20] \times [0, 10]$, see section 1.3.

Figure 3.8 displays the average vertical velocity component. Induced by buoyancy, the centreline vertical velocity initially increases for $0 < x < 2$ reaching a

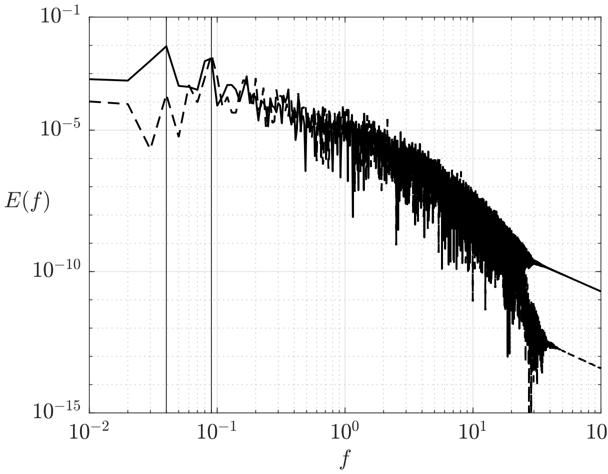

FIGURE 3.6: Frequency spectrum of vertical and cross-flow velocity components at $(x, y) = (5.00, 1.75)$. ——: u; – –: v.

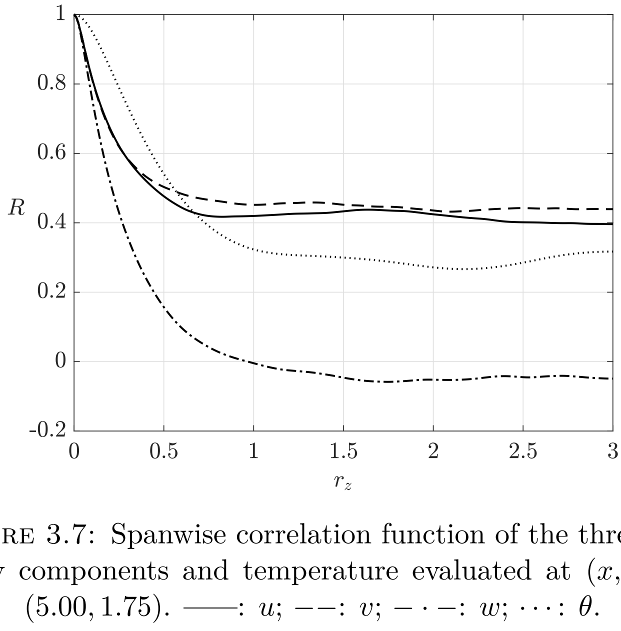

FIGURE 3.7: Spanwise correlation function of the three velocity components and temperature evaluated at $(x, y) = (5.00, 1.75)$. ——: u; – –: v; – · –: w; · · ·: θ.

maximum value larger than the inlet value. On the contrary, the vertical velocity peaks relative to the lateral jets decrease in intensity, again due to buoyancy. Together with this decrease, the shift of the lateral peaks towards the centreline indicate the bending of cold jets. As a result, for $2 < x < 8$, a region of strong interactions between the three jets is observed. Mixing finally leads to the coalescence of the three jets, which for $x > 8$ form a single stream, later shown to have self-similar characteristics.

The mean temperature field is shown in figure 3.9. Above the cold jet exits, temperature exihibits a plume-like pattern. Most of the mean temperature gradients are limited to the mixing region while for $x > 6$ temperature variations are restricted to a range $|\Delta\langle\theta\rangle| < 0.1$, thus implying that buoyancy effects are negligible beyond that vertical coordinate.

Figures 3.10 and 3.11 display the standard deviation of vertical and cross-flow velocity fluctuations (u_{rms}, v_{rms}). At the jet inlets, $x = 0$, u_{rms} and v_{rms} display the typical channel-flow distributions and thus are strongly inhomogeneous. In the pool fluctuations are found to increase in intensity along both the vertical and cross-flow directions. A spreading of the regions of high turbulent activity is also observed. The spreading is such that for $x \geq 10$, no lateral peaks of turbulent activity are observed and the flow behaves similarly to a single turbulent jet where turbulent intensities are the strongest at the centreline and decrese towards the sides. Tthe increment of turbulent fluctuations close to the jet inlets is a combined effect of the development of shear layer instabilities and buoyancy forces. This tendency is observed up to $x \simeq 6$ where the mean velocity shear becomes weaker, see figure 3.8, and hence a decrease of turbulent production by mean shear and of the turbulent intensities occurs. Also, as mentioned above, for $x > 6$ mean temperature differences are confined within $[-0.1, 0.1]$ and thus the flow behaves as essentially non-buoyant. As a consequence, the mixing region of the three jets is found to be the site of the higher turbulent activities with a peak centred at $(x, y) = (3.5, 0.6)$ for the fluctuations of the vertical velocity component and at $(x, y) = (3.8, 1.1)$ for the cross-flow.

Figure 3.12 shows the standard deviation of the temperature field. Also temperature fluctuations start from a strongly inhomogeneous distribution inherited from the inlet condition, and then undergo an increase in intensity and a spread in the cross-flow direcion, similar to the behaviour observed for the velocity fluctuations. The increase in intensity is observed up to $x = 5$, and can be ascribed to turbulence production associated with the mean temperature gradients, which are non-negligible for $x < 6$, see figure 3.9. Hence, the mixing region of the three

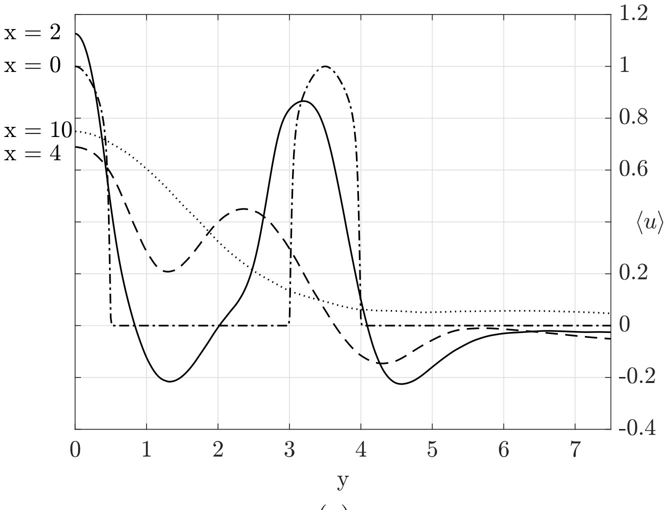

(a)

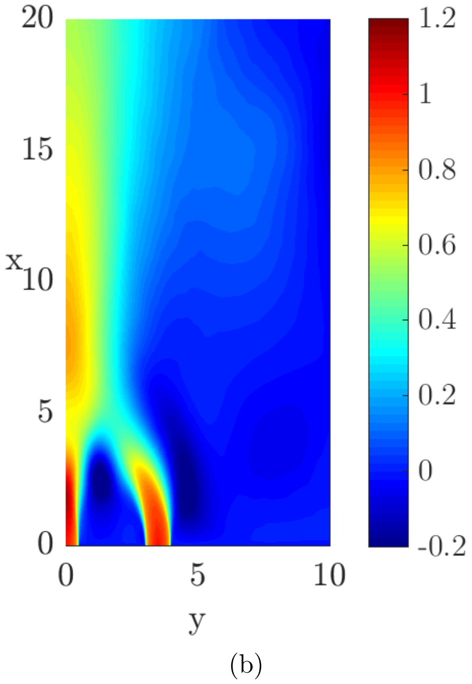

(b)

FIGURE 3.8: Mean vertical velocity component: subfigure (a) displays profiles at selected x-coordinates: $-\cdot-$: $x = 0$; ——: $x = 2$; $--$: $x = 4$; $\cdots$: $x = 10$. Subfigure (b) displays contours over interval $[0, 20] \times [0, 10]$.

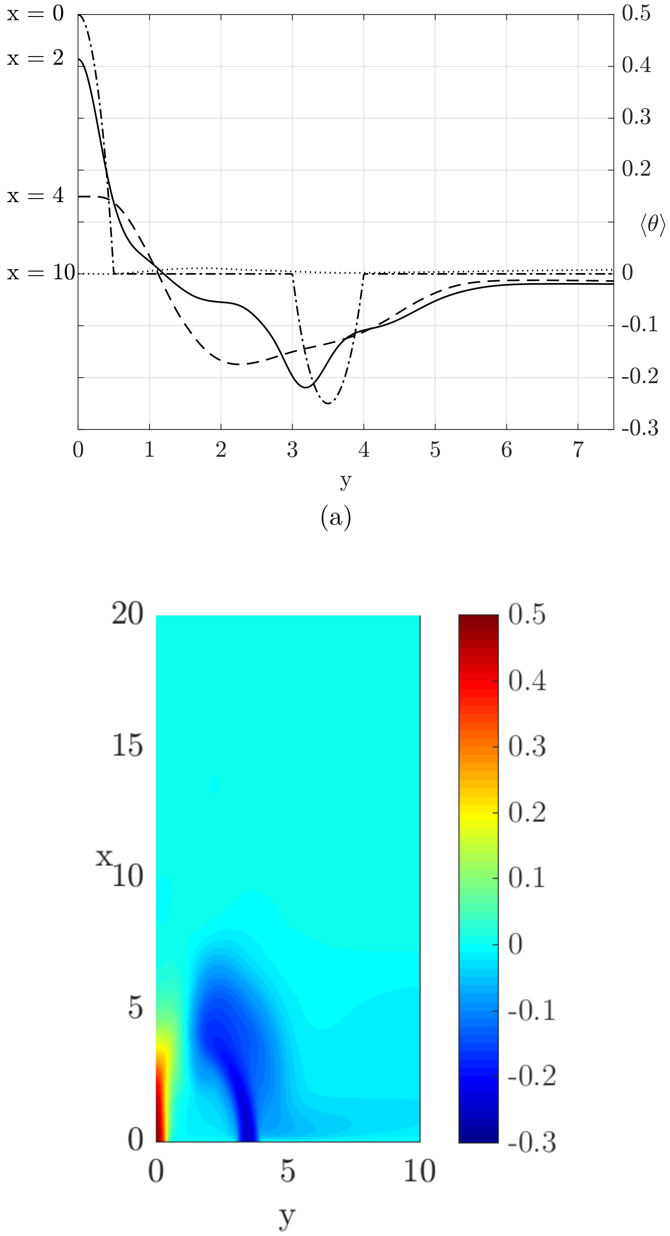

(a)

(b)

FIGURE 3.9: Mean temperature field $\langle\theta\rangle$: subfigure (a) displays profiles at selected x-coordinates: $- \cdot -$: $x = 0$; ——: $x = 2$; $--$: $x = 4$; $\cdots$: $x = 10$. Subfigure (b) displays contours over interval $[0, 20] \times [0, 10]$.

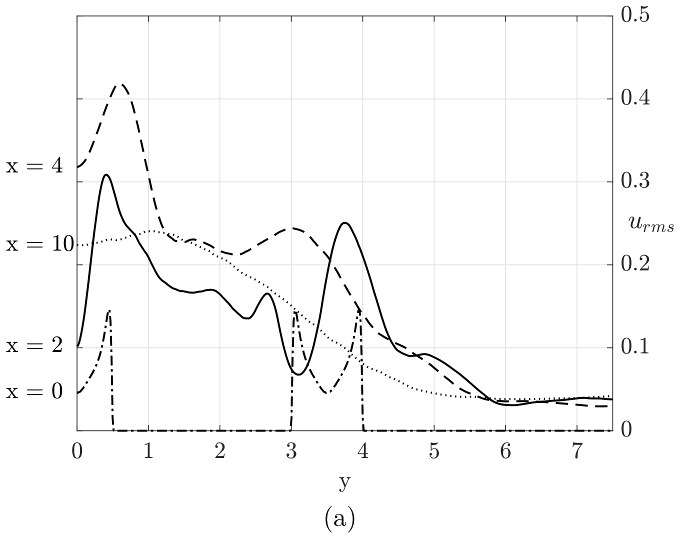

(a)

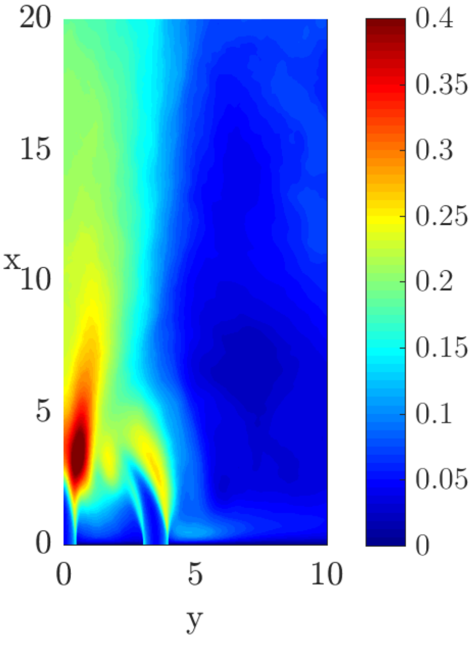

(b)

FIGURE 3.10: Velocity fluctuations in the vertical direction u_{rms}: subfigure (a) displays profiles at selected x-coordinates: $- \cdot -$: $x = 0$; ——: $x = 2$; $--$: $x = 4$; $\cdots$: $x = 10$. Subfigure (b) displays contours over interval $[0, 20] \times [0, 10]$.

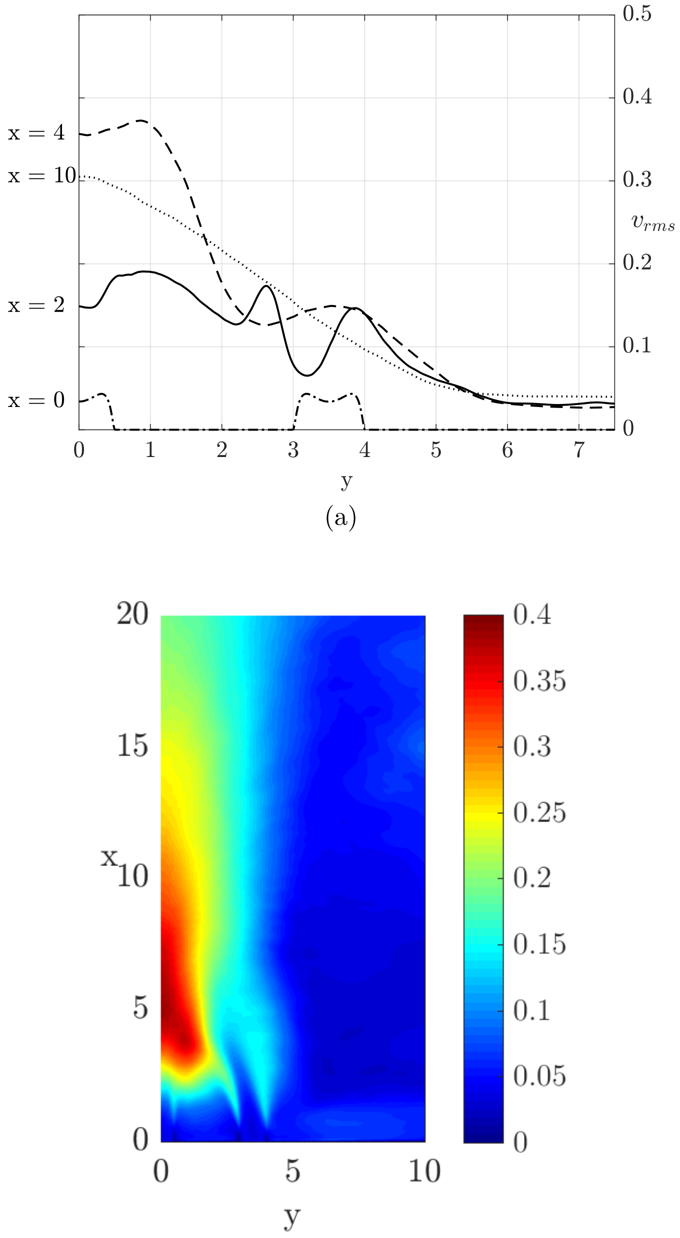

(a)

(b)

FIGURE 3.11: Velocity fluctuations in the cross-flow direction v_{rms}: subfigure (a) displays profiles at selected x-coordinates: $- \cdot -$: $x = 0$; ——: $x = 2$; $--$: $x = 4$; $\cdots$: $x = 10$. Subfigure (b) displays contours over interval $[0, 20] \times [0, 10]$.

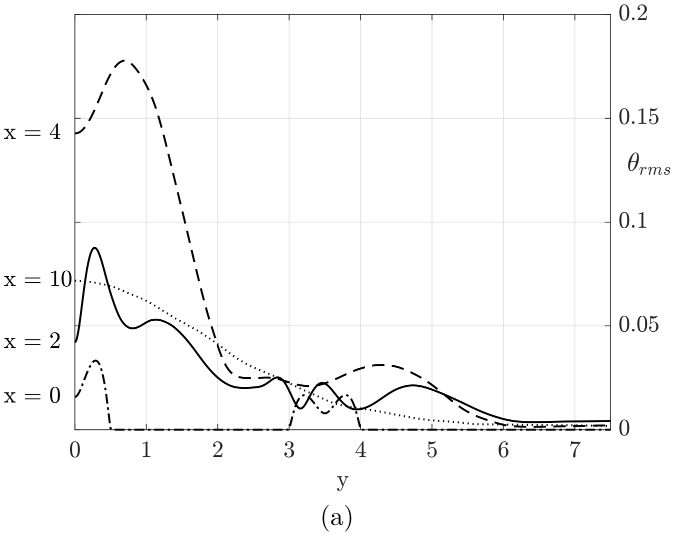

(a)

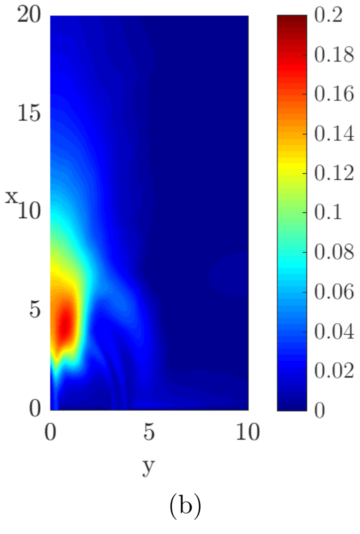

(b)

FIGURE 3.12: Temperature fluctuations θ_{rms}: subfigure (a) displays profiles at selected x-coordinates: $- \cdot -$: $x = 0$; ——: $x = 2$; $--$: $x = 4$; $\cdots$: $x = 10$. Subfigure (b)displays contours of θ_{rms} over interval $[0, 20] \times [0, 10]$.

jets is recognized to be also the site of the most intense temperature fluctuations, where a peak is measured for $(x, y) = (5.2, 1.1)$. For $x \geq 10$, the weakening combined to cross-flow spreading of temperature fluctuations recover a behaviour similar to classical single jets, as discussed in § 3.4.4.

As one may expect from the above discussion also turbulent heat transfer undergoes a substantial increase in the pool. Figures 3.13 and 3.14 display components of turbulent heat flux in vertical and cross-flow directions. Let us define $\tilde{u}$ and $\tilde{\theta}$ to be the orders of magnitude of velocity and temperature fluctuations in the highly active region $x < 10$, where velocity fluctuations share the same order of magnitude in all directions; θ_j represents the mean centreline temperature of the central jet and ℓ is the characteristic width of the jet, defined as the y-coordinate where the mean vertical velocity reaches half of its centreline value, $\langle u\rangle(x, \ell(x)) = U_c(x)/2$. Considering heat fluxes in the x direction, mean advection is much larger than the turbulent heat flux, $U_0\, \theta_j \gg \tilde{u}\, \tilde{\theta}$. In the y direction, mean and turbulent advection are of the same order of magnitude $\langle v\rangle\, \theta_j \sim \tilde{u}\, \tilde{\theta}$, where $\langle v\rangle \sim \tilde{u}$ from the results. Despite the present Péclet number ($Pe = Re\, Pr = 155$), turbulent heat fluxes are larger than diffusion along both x and y; along the x direction: $\tilde{u}\, \tilde{\theta} \gg Pe^{-1}\theta_j/x$ while in the y direction: $\tilde{u}\, \tilde{\theta} \gg Pe^{-1}\theta_j\, /\ell$. In the present case the ratio between turbulent and diffusive heat fluxes is $\mathcal{O}(10^2)$ for $x \leq 10$. Further from the inlet, $x > 10$, this ratio becomes $\mathcal{O}(10^1)$.

3.4.3 Momentum fluxes

Momentum fluxes in the x direction are introduced to provide an explaination of the physical mechanism underlying the merging of the three jets. The average momentum equation in the vertical direction x can be written in terms of momentum flux per unit volume, indicated here by $\vec{\varphi} = (\varphi_1, \varphi_2)$ in the non-dimesional formulation

$$\frac{\partial \varphi_1}{\partial x} + \frac{\partial \varphi_2}{\partial y} = \frac{Gr}{Re^2}\langle\theta\rangle \tag{3.3}$$

where the components of the averaged x-momentum flux are

$$\varphi_j = \langle u_1\rangle\langle u_j\rangle + \langle u_1' u_j'\rangle + \langle p\rangle\delta_{1j} - \frac{1}{Re}\frac{\partial\langle u_1\rangle}{\partial x_j} \tag{3.4}$$

As the viscous contribution to momentum fluxes is negligible in the flow region considered, the last term in equation (3.4) is omitted from the discussion. Figure 3.15 displays profiles of φ_1 and φ_2 at selected x coordinates. Notice that $\varphi_2 > 0$

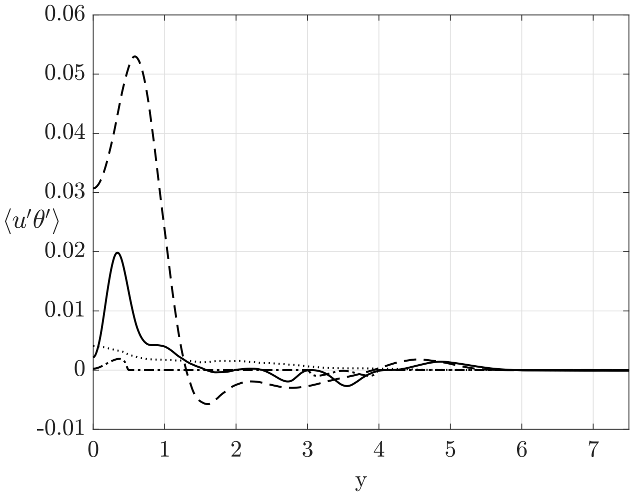

(a)

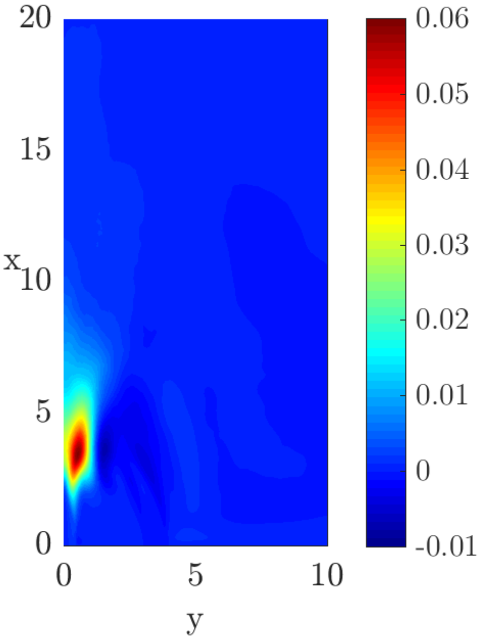

(b)

FIGURE 3.13: Turbulent heat fluxes along the x-direction $\langle u'\theta' \rangle$: subfigure (a) displays profiles at selected x-coordinates: $- \cdot -$: $x = 0$; ——: $x = 2$; $--$: $x = 4$; $\cdots$: $x = 10$. Subfigure (b)displays contours of $\langle u'\theta' \rangle$ over interval $[0, 20] \times [0, 10]$.

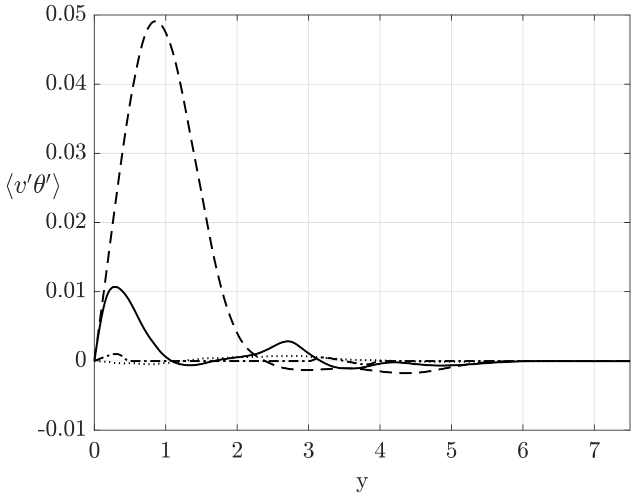

(a)

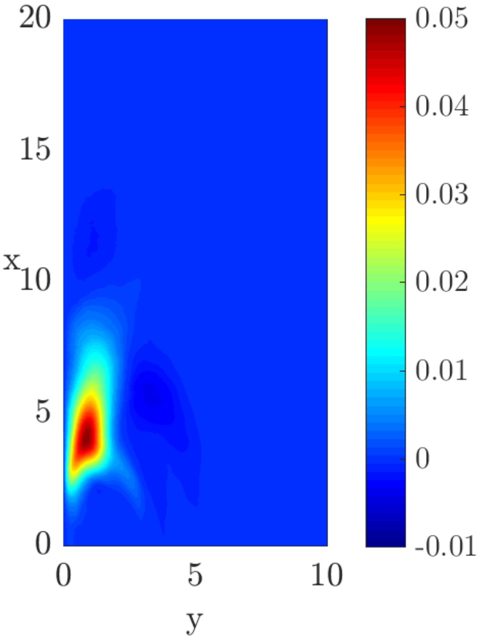

(b)

FIGURE 3.14: Turbulent heat fluxes along the y-direction $\langle v'\theta' \rangle$: subfigure (a) displays profiles at selected x-coordinates: $- \cdot -$: $x = 0$; ——: $x = 2$; $--$: $x = 4$; $\cdots$: $x = 10$. Subfigure (b)displays contours of $\langle v'\theta' \rangle$ over interval $[0, 20] \times [0, 10]$.

represents a x-momentum flux occuring across y-normal surfaces in direction $+y$, while if $\varphi_2 < 0$ the x-momentum flux is directed as $-y$. The same reasonings apply for φ_1.

At the inlet ($x = 0$) x-momentum flux occurs only along the x direction and pressure is found to be minimum at the centreline and maximum just outside the lateral jets. This pressure distribution is symptomatic of the jets convergence occuring just above the inlet plane. At $x = 2$, the profile of φ_2 indicates that the central jet ($y \approx 0.5$) transfers x-momentum in the $+y$ direction, while momentum transfer due to the jet on the right side ($y \approx 3.0$) is directed as $-y$. In addition pressure is minimum between central and lateral jets. A similar behaviour is observed at $x = 4$ where the φ_2 profile clearly indicates the mutual entrainment of the jets. The positive peak of φ_2 corresponds to the edge of the central jet ($y \approx 0.5$) while the negative peak is at $y \approx 2.1$, and this indicates that the lateral jets are bending toward the centerline. For $x = 8$, the x-momentum fluxes are typical of a purely mechanical, planar jet. Momentum production due to buoyancy is negligible (as mean temperature differences are very small) and the main momentum flux is directed in the streamwise direction. Along the cross-flow direction y the low-intensity momentum flux is responsible for the entrainment of quiescent fluid and causes the spreading of the stream. This analysis suggests that the coalescence of the three jets is associated to their mutual entrainment, *i.e.* the phenomenon known as Coandă effect.

3.4.4 Self-similarity

Fluid flow and heat transfer characteristics of the region far from the inlet are described in the following. As previously observed the flow field for $x > 10$ behaves as a single stream similar to that of a single jet and is essentially non-buoyant.

The mean vertical velocity component at the centerline $U_c(x) = \langle u \rangle(x, 0)$ is found to scale with the square-root of the distance from a virtual origin

$$U_c(x) = \frac{1}{\sqrt{0.15(x + 1.4)}} \tag{3.5}$$

as shown in figure 3.16(a). The jet width $\ell(x)$, defined in section 3.4.2, is found to scale linearly with x. As shown in figure 3.16(b), $\ell(x)$ scales as

$$\ell(x) = 0.13\,(x + 3.54) \tag{3.6}$$

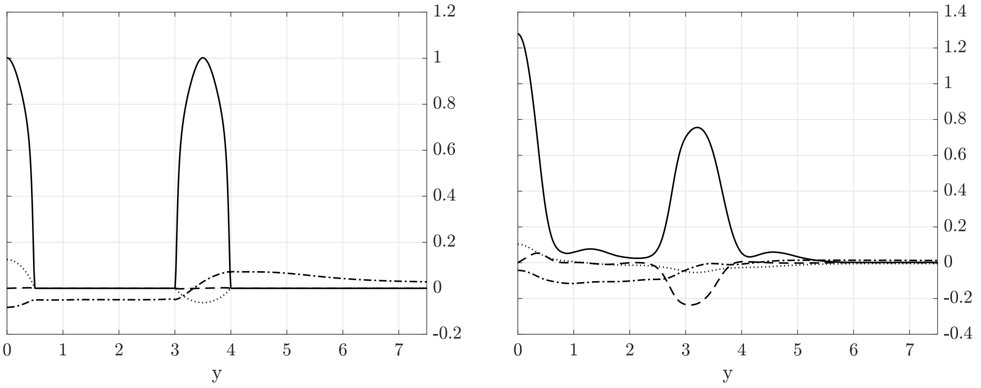

(a) $x = 0$ (b) $x = 2$

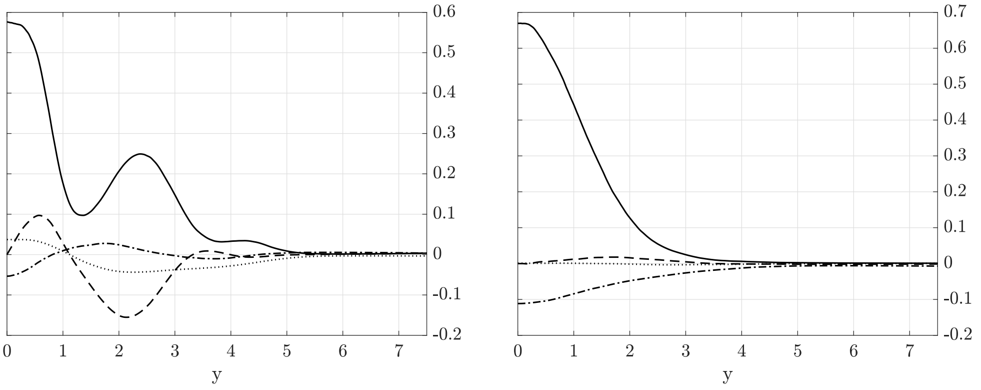

(c) $x = 4$ (d) $x = 8$

FIGURE 3.15: x-momentum fluxes and production by buoyancy at selected vertical coordinates: $x = 0, 2, 4, 8$. ——: $\varphi_1 - \langle p \rangle$; −−: φ_2; − · −: $\langle p \rangle$; · · ·: $(Gr/Re^2)\langle \theta \rangle$.

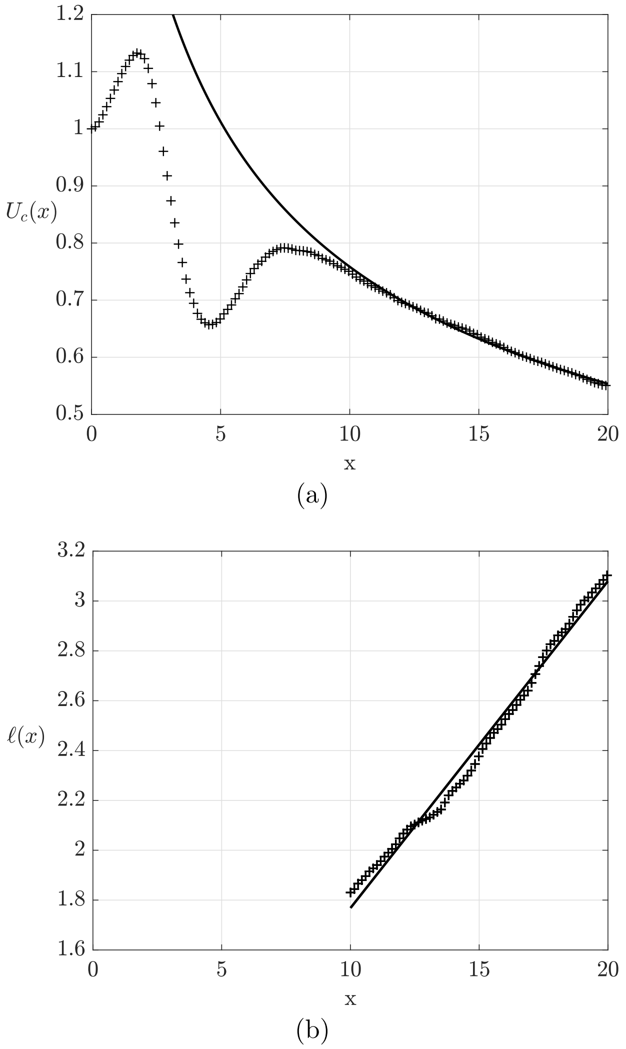

(a)

(b)

FIGURE 3.16: (a) profiles of the jet centreline velocity $U_c(x)$: ——, equation (3.5); + present results. (b) profiles of the jet width $\ell(x)$: ——, equation (3.6); + present results.

Self-similarity features for $x \geq 10$ are displayed in figures 3.17(a) and (b) where velocities are scaled by the centreline velocity $U_c(x)$ and lengths are scaled using $\ell(x)$ as the length scale. Similarity laws hold true for $y/\ell < 2$. Conversely, the flow for $y/\ell > 2$ exhibits a different behaviour due to the complex inlet configuration.

Some observables follow the well-established similiarity laws reported by Tennekes and Lumley (1972) for single, purely mechanical jets and wakes. It can be concluded that in this region the flow recovers universal properties *i.e.* is largely independent of the inlet conditions.

3.4.5 Data for turbulence modelling

Figure 3.18 displays the turbulent kinetic energy distribution. The typical channel-flow distribution of k at the inlet rapidly evolves in the mixing region, and its intensity increases by one order of magnitude due to the production term

$$\langle u_i' u_j' \rangle \frac{\partial \langle u_j \rangle}{\partial x_i} \tag{3.7}$$

which accounts for the transfer of mechanical energy to the fluctuating part of the flow (Pope, 2001). Further from the inlet, $x \geq 10$, the classical bell-shaped profile observed in planar jets is recovered.

Figures 3.19 and 3.20 show the dissipation rate of turbulent kinetic energy $\langle \varepsilon \rangle$ (equation (2.17)) and temperature variance $\langle \varepsilon_\theta \rangle$ (equation (2.36)). Profiles of ε in the $x < 10$ region are shown to have several peaks, each of them corresponds to one of the two shear layers at the sides of each jet. A similar behaviour is observed for the temperature variance dissipation, where ε_θ at the central jet is more intense. Moreover profiles of ε and ε_θ at $x = 0$ show non-zero values outside the jets region as a result of the interaction of negatively-buoyant fluid fallen onto the inflow plane, which is maintained at constant temperature ($\theta = 0$) and no slip conditions applies. Profiles of $\langle \varepsilon \rangle$ and $\langle \varepsilon_\theta \rangle$ for $x \geq 10$ are typical of a mechanical, planar jet.

In the present configuration, the behaviour of turbulent viscosity is very irregular. It undergoes sudden increases (and decreases) by orders of magnitude. Figure 3.21 displays y-profiles of ν_t/ν calculated as

$$\frac{\nu_t}{\nu} = -Re \, \langle u'v' \rangle \left(\frac{\partial \langle u \rangle}{\partial y} + \frac{\partial \langle v \rangle}{\partial x} \right)^{-1} \tag{3.8}$$

Only far from the inlets ($x \geq 10$) the distribution in y direction becomes more regular. In the self-similar region ($x \geq 10$) the viscosity ratio ν_t/ν is observed to

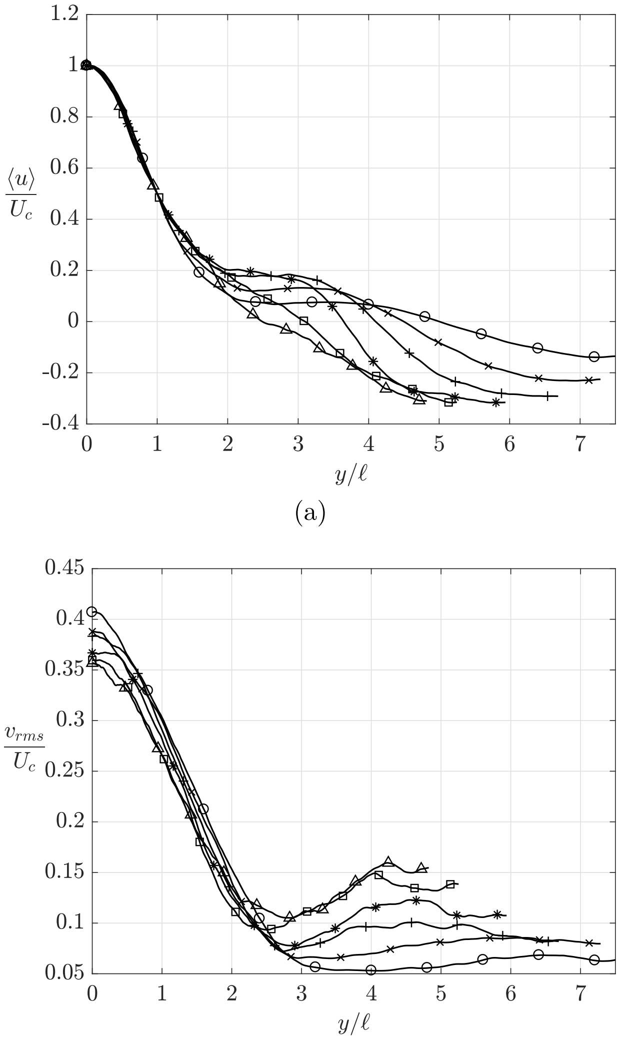

(a)

(b)

FIGURE 3.17: Profiles of (a) mean and (b) fluctuating velocities scaled with the centerline velocity as functions of y/ℓ. ◯: $x = 10$; ×: $x = 12$; +: $x = 14$; ∗: $x = 16$; □: $x = 18$; △: $x = 20$.

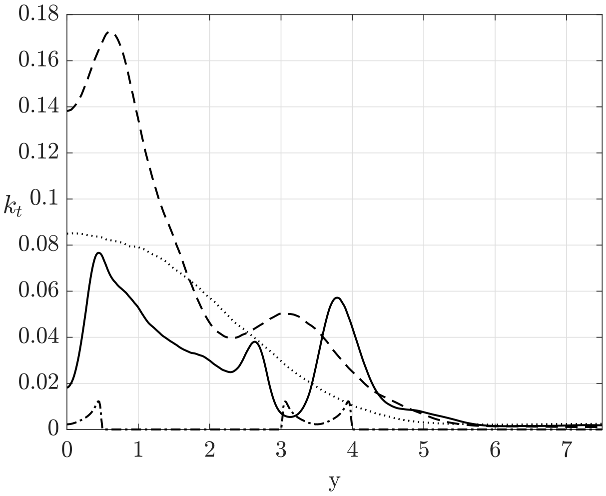

(a)

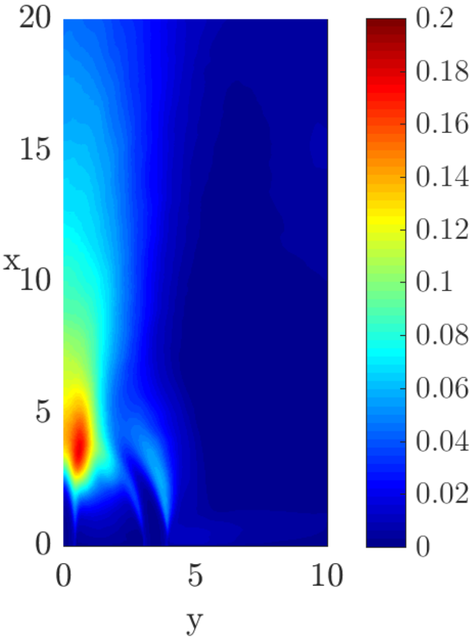

(b)

FIGURE 3.18: Turbulent kinetic energy distribution: $-\cdot-$: $x = 0$; —: $x = 2$; $--$: $x = 4$; $\cdots$: $x = 10$.

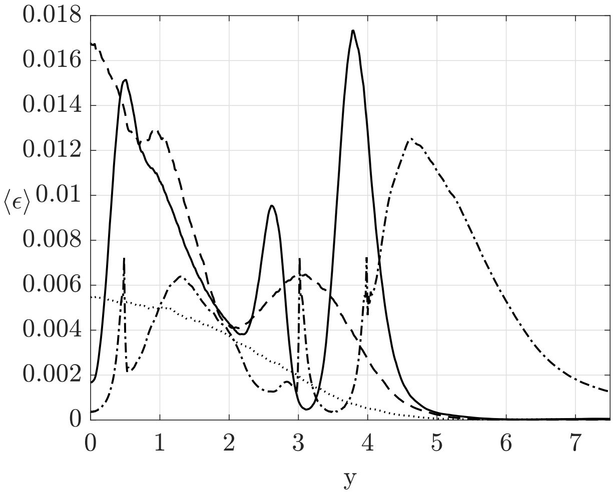

(a)

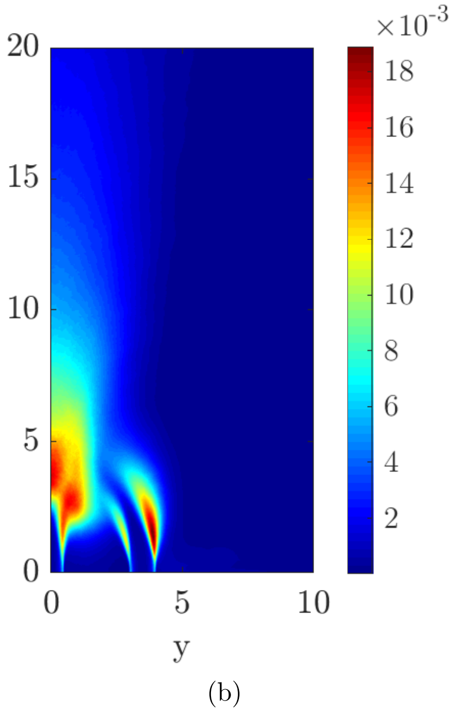

(b)

FIGURE 3.19: (a) dissipation of the turbulent kinetic energy computed at different x-coordinates: $-\cdot-$: $x = 0$; —: $x = 2$; $--$: $x = 4$; $\cdots$: $x = 10$. (b) contours of ε over interval $[0, 20] \times [0, 10]$.

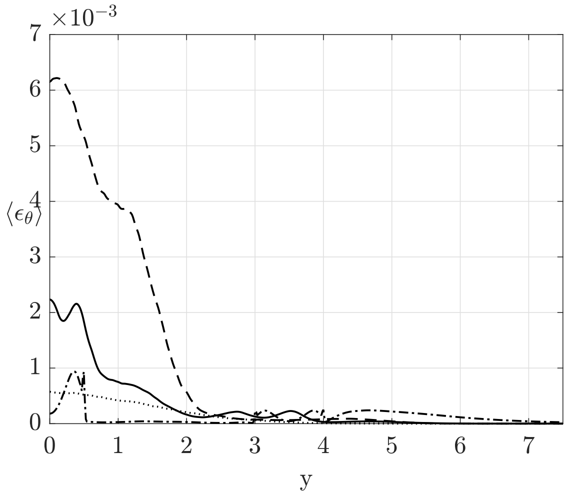

(a)

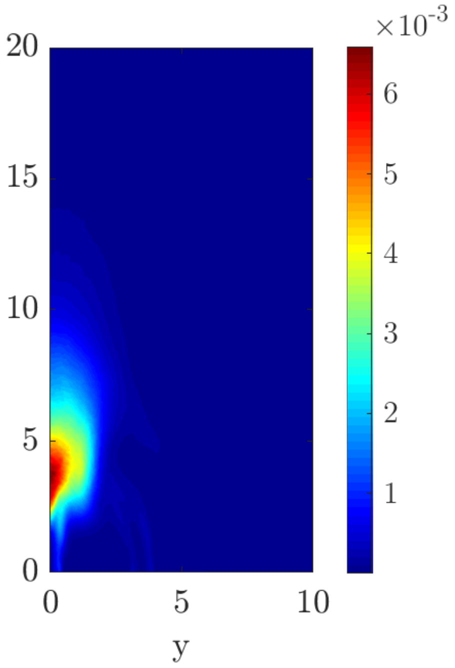

(b)

FIGURE 3.20: (a) temperature variance dissipation rate computed at different x-coordinates: $-\cdot-$: $x = 0$; —: $x = 2$; $--$: $x = 4$; $\cdots$: $x = 10$. (b) contours of ε_θ over interval $[0, 20] \times [0, 10]$.

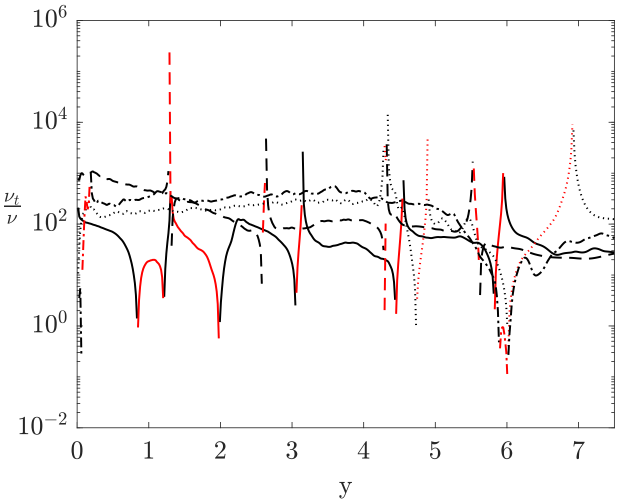

FIGURE 3.21: Distribution of turbulent viscosity: —: $x = 2$; – –: $x = 4$; $\cdots$: $x = 10$ $- \cdot -$: $x = 20$. Black and red lines respectively indicate positive and negative values.

increase in the x direction. A simple order of magnitude analysis suggests that far from the inlet the turbulent viscosity is of order $\nu_t^* \sim \ell^* u^{*2}/U_c^*$, where the asterisks indicate dimensional quantities. In non-dimensional form

$$\frac{\nu_t}{\nu} \sim Re\, U_c\, \ell \left(\frac{u_{\mathrm{rms}}}{U_c}\right)^2 \tag{3.9}$$

Subtitution of approximations given above for U_c and ℓ (see equations (3.5) and (3.6)) and the value of $u_{\mathrm{rms}}/U_c \sim 0.3$ observed in the self-similar region, leads to conclude that ν_t/ν increases like $0.03\, Re\, \sqrt{x}$. This is approximately verified by our results in the single planar jet region for $x \gtrapprox 10$, see figure 3.22.

Similar to turbulent viscosity, the behaviour of turbulent thermal diffusivity is very irregular. This is shown in figure 3.23, where the ratio between turbulent and molecular diffusivities in the x and the y directions is displayed, for three x stations in the region $x \leq 10$. This suggests that in very complex flow configurations like the one considered here, turbulence modelling is not an easy task and the gradient diffusion hypothesis is expected to provide inaccurate results; see Errico and Stalio (2014) for a more extensive discussion on these topics. Figure 3.24 displays contour lines of the cosine of β, the angle between average temperature gradient and turbulent heat fluxes. The gradient diffusion hypothesis requires that the gradient of the temperature field is aligned with the turbulent heat flux vector *i.e.* $\cos\beta = 1$ throughout the flow domain. As displayed in figure 3.24, the two vectors are approximately aligned $0.9 < \cos\beta \leq 1$ only in very

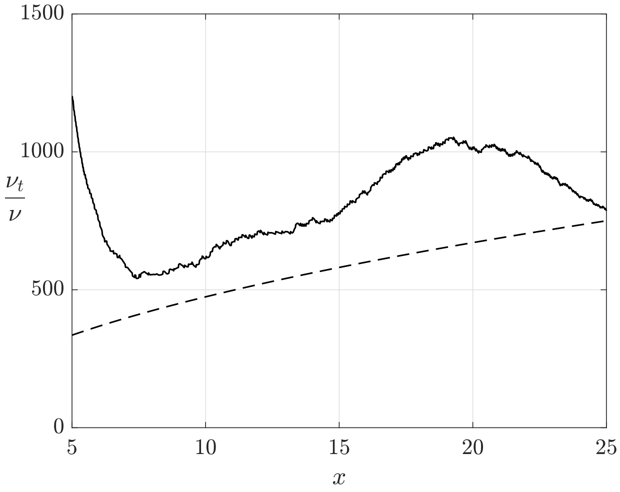

FIGURE 3.22: Ratio between turbulent and molecular viscosity along the centreline in the range $x \in [5, 25]$. ——: equation (3.9), – –: $0.03\,Re\,\sqrt{x}$.

limited regions of the flow computed, for example in the shear layer of the single mechanical jet, $x > 10$. Most of the flow domain is instead characterized by $\cos\beta < 0$ *i.e.* the two vectors point in opposite directions and turbulence models relying on turbulent diffusivity are expected to fail in this context.

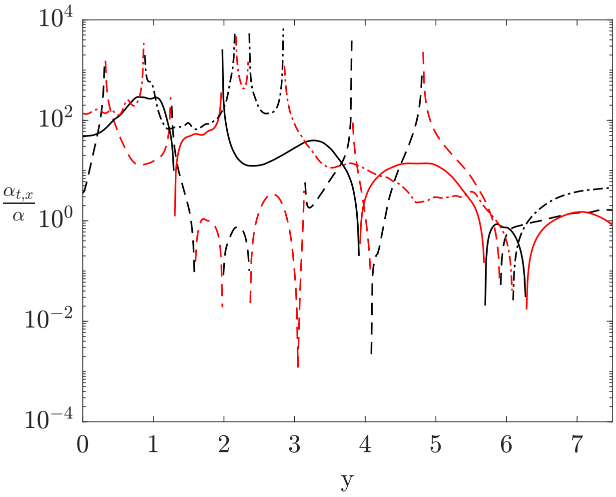

(a)

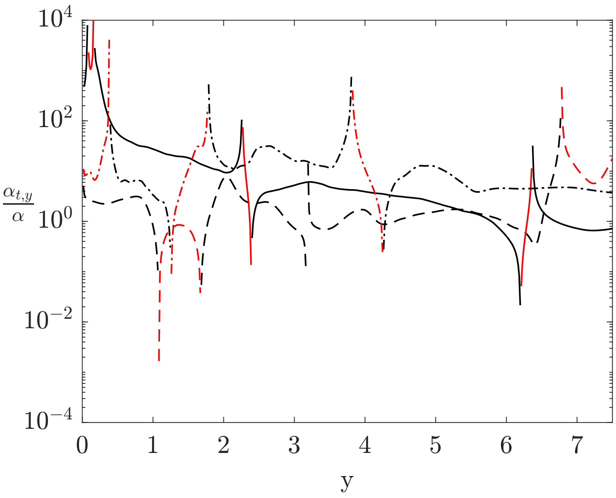

(b)

FIGURE 3.23: Ratio between turbulent and molecular diffusivity along the x (a) and y (b) directions for different x-coordinates: —: $x = 2$; −−: $x = 4$; ···: $x = 10$. Black and red lines respectively indicate positive and negative values.

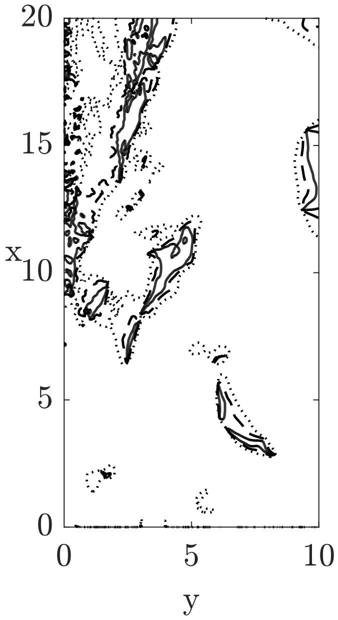

FIGURE 3.24: Contour lines of $\cos\beta$, where β is the angle between temperature gradient and turbulent heat flux vectors: $\cdots$: $\cos\beta = 0.0$; $--$: $\cos\beta = 0.5$; —: $\cos\beta = 0.9$.

Concluding remarks

In this thesis turbulent flows and heat transfer in natural and mixed convection regimes have been studied by means of Direct Numerical Simulations. Buoyancy-driven flows are investigated in a laterally unbounded Rayleigh-Bénard cell with aspect ratio $\Gamma = 8$, for different operating fluids: liquid mercury ($Pr = 0.025$), air ($Pr = 0.7$) and water ($Pr = 7$). By following a recently-introduced approach (Schumacher et al., 2015) Rayleigh number is varied along with Pr in order to maintain a constant Grashof number, thus leaving the momentum equations unchanged. In second place mixed convection in low-Prandtl-number fluids is analysed in a rectangular pool of Lead-Bismuth Eutectic ($Pr = 0.031$) where three jets are vertically discharged upwards and enter with the same average velocity but different temperature. The central jet is hot while the lateral ones are cold. Both configurations are deemed to be of interest for environmental flows and technological applications. Although RBC has been extensively studied in the past and nowadays, simulations at constant Grashof number in such large computational domains have not been presented yet, at least to the author's knowledge. On the other hand several numerical works about the triple jet configuration have been published but none of them have been performed without turbulence models. The DNS presented in this thesis might be the first one.

Simulations are performed using a customised version of the code *Incompact3d* , where in-house modifications involve the addition of the Boussinesq's buoyancy term in the momentum equations, the implementation of an open outflow boundary condition suitable for buoyant flows and the development of an inflow strategy, which allows to specify at jet inlets velocity and temperature profiles recorded from a precursor channel DNS. All the modifications implemented have been validated and validation test are presented in chapter 1. In addition the validity of the Boussinesq's approximation has been assessed in every configuration studied by using the well-know method by Gray and Giorgini (1976). Computational resources required for calculations have been granted through the PRACE (Partnership for Advanced Computing in Europe) and ISCRA (Italian SuperComputing Resource Allocation) programmes on CINECA's (Consorzio Interuniversitario per il calcolo automatico) "Marconi" cluster, accounting for more than 70 million core hours overall.

Results in RBC configurations show that thermal plumes behave very differently in the three cases considered. At low Prandtl number data show that plumes width is comparable to the cell height and no clear distinction exists between the large scale circulation and plumes themselves. In addition, thermal plumes in liquid mercury are found to travel across the fluid layer while increasing their width, impingement is very vigorous and occurs inside the thermal boundary layer on the opposite wall. Instead, in configurations employing water and air, thermal plumes are much thinner with respect to the liquid mercury case and respectively have a decreasing and constant width. Plumes penetration is also reduced, causing impingement to create a less intense positive divergence in these two configurations. Both $\langle k \rangle$ and $\langle \theta'^2 \rangle$ budget equations show that the fluid layer can be divided in a viscous (or diffusive, when temperature variance is considered) layer close to the walls, a transitional layer and a bulk region, according to the topological analysis reported in Togni et al. (2015). Therefore the applicability of such subdivision, which has been developed for $Ra = 10^5 - 10^7$ and $Pr = 0.7$, should be considered extended at least to configurations investigated here.

The statistical analysis of the triple jet configuration reveals that the three jets undergo an intense mixing close to the inlet, while for $x > 8H$ a single and isothermal stream is observed. In the mixing region the intensities of velocity and temperature fluctuations are much larger than the inlet values as a result of the combined effect of buoyancy forces and shear-layer instabilities. Superimposed to the development of turbulence, low-frequency undulations and shedding of large-scale vortices arise. Such phenomena are an unambiguous signature of the entanglement of the three jets dynamics and affect flow behaviour throughout the domain. The analysis of momentum fluxes suggests that the three jets coalesce as a result of their mutual entrainment, *i.e.* the phenomenon commonly known as Coandă effect. Consequently the analysis reported provides an original interpretation of this effect commonly known for its outcomes but yet scarcely investigated in its origins, at least to the author's knowledge. For $x > 10H$ the coalesced single stream is found to recover some of the self-similar characteristics of classical, purely mechanical jets and hence behaves in a more universal way. Moreover, relevant quantities for turbulence modelling such as turbulent viscosity and diffusivity, as well as dissipation of turbulent kinetic energy and temperature variance, show very irregular behaviours suggesting that turbulence modelling is a difficult task in this configuration. Contour lines of the angle between temperature gradient and turbulent heat flux vector indicate that typical turbulent viscosity models are prone to fail.

In summary, results presented are aimed to shed light on heat transfer mechanisms in buoyant turbulent flows, in particular when operating fluids have a non-unitary Prandtl number. Statistics reported might also serve as numerical benchmarks on which validate turbulent models to be employed for the design of applications involving buoyant flows.

Results of the triple jet simulation have been presented in a couple of international conferences (Angeli et al., 2017; Fregni et al., 2019c) and in a workshop (Fregni et al., 2019b). These have been finally published in an international journal (Fregni et al., 2019a). Collaborative efforts with other members of the European project named "SESAME" are published or have been recommended for publication in Nuclear Engineering and Design (Angeli et al., 2019; Shams et al., 2019a,b). Different kind of investigations, concerning numerical studies of techniques for heat transfer enhancement in race-car power modules, have been presented in an international conference (Baraldi et al., 2019) and are published in a recently-issued international journal (Sabato et al., 2019).

Bibliography

Ahlers, G., Grossmann, S., Lohse, D., 2009. Heat transfer and large scale dynamics in turbulent Rayleigh-Bénard convection. Reviews of modern physics 81 (2), 503.

Angeli, D., Cimarelli, A., Fregni, A., Stalio, E., Shams, A., Roelofs, F., 2017. Numerical simulation of mixing buoyant jets: preliminary studies. In: 17th International Topical Meeting on Nuclear Reactor Thermal Hydraulics, NURETH 2017. Vol. 2017. Association for Computing Machinery, Inc.

Angeli, D., Fregni, A., Stalio, E., 2019. Direct Numerical Simulation of turbulent forced and mixed convection of LBE in a bundle of heated rods with P/D= 1.4. Nuclear Engineering and Design 355, 110320.

Baraldi, N., Fregni, A., Sabato, M., Stalio, E., Brusiani, F., Tranchero, M., Baritaud, T., 2019. Comparison between cooling strategies for power electronic devices: fractal mini-channels and arrays of impinging submerged jets. In: Journal of Physics: Conference Series. Vol. 1224. IOP Publishing, p. 012014.

Batchelor, G. K., 1959. Small-scale variation of convected quantities like temperature in turbulent fluid Part 1. General discussion and the case of small conductivity. Journal of Fluid Mechanics 5 (1), 113–133.

Bleninger, T., Jirka, G. H., 2008. Modelling and environmentally sound management of brine discharges from desalination plants. Desalination 221 (1-3), 585–597.

Bolgiano, R., 1959. Turbulent spectra in a stably stratified atmosphere. Journal of Geophysical Research 64 (12), 2226–2229.

Boussinesq, J., 1903. Theorie analytique de la chaleur vol. 2. Gauthier-Villars, Paris.

Bremhorst, K., Krebs, L., 1992. Experimentally determined turbulent Prandtl numbers in liquid sodium at low Reynolds numbers. International Journal of Heat and Mass Transfer 35 (2), 351–359.

Bremhorst, K., Krebs, L., Müller, U., Listijono, J., 1989. Application of a gradient diffusion and dissipation time scale ratio model for prediction of mean and fluctuating temperature fields in liquid sodium downstream of a multi-bore jet block. International Journal of Heat and Mass Transfer 32 (11), 2037–2046.

Brunings, J., 1982. Lmfbr thermal-striping evaluation. Tech. rep., Rockwell International Corp.

Calkins, M. A., Aurnou, J. M., Eldredge, J. D., Julien, K., 2012. The influence of fluid properties on the morphology of core turbulence and the geomagnetic field. Earth and Planetary Science Letters 359, 55–60.

Calzavarini, E., Toschi, F., Tripiccione, R., 2002. Evidences of Bolgiano-Obhukhov scaling in three-dimensional Rayleigh-Bénard convection. Physical Review E 66 (1), 016304.

Cao, Q., Lu, D., Lv, J., 2012. Numerical investigation on temperature fluctuation of the parallel triple-jet. Nuclear Engineering and Design 249, 82–89.

Chacko, S., Chung, Y., Choi, S., Nam, H., Jeong, H., 2011. Large-eddy simulation of thermal striping in unsteady non-isothermal triple jet. International Journal of Heat and Mass Transfer 54 (19-20), 4400–4409.

Chillà, F., Schumacher, J., 2012. New perspectives in turbulent Rayleigh-Bénard convection. The European Physical Journal E 35 (7), 58.

Corrsin, S., 1951. On the spectrum of isotropic temperature fluctuations in an isotropic turbulence. Journal of Applied Physics 22 (4), 469–473.

Eckert, E. R. G., Drake, R. M., 1987. Analysis of heat and mass transfer. Hemisphere Publishing, New York.

Engineering ToolBox, 2005. Liquid mercury properties. `https://www.engineeringtoolbox.com/mercury-d_1002.html`, accessed: 25-11-2019.

Errico, O., Stalio, E., 2014. Direct Numerical Simulation of turbulent forced convection in a wavy channel at low and order one Prandtl number. International Journal of Thermal Sciences 86, 374–386.

Fazio, C., Sobolev, V., Aerts, A., Gavrilov, S., Lambrinou, K., Schuurmans, P., Gessi, A., Agostini, P., Ciampichetti, A., Martinelli, L., et al., 2015. Handbook on lead-bismuth eutectic alloy and lead properties, materials compatibility, thermal-hydraulics and technologies-2015 edition. Tech. rep., Organisation for Economic Co-Operation and Development.

Flageul, C., Benhamadouche, S., Lamballais, É., Laurence, D., 2015. DNS of turbulent channel flow with conjugate heat transfer: Effect of thermal boundary conditions on the second moments and budgets. International Journal of Heat and Fluid Flow 55, 34–44.

Fregni, A., Angeli, D., Cimarelli, A., Stalio, E., 2019a. Direct Numerical Simulation of a buoyant triple jet at low-Prandtl number. International Journal of Heat and Mass Transfer 143, 118466.

Fregni, A., Angeli, D., Cimarelli, A., Stalio, E., 2019b. Direct Numerical Simulation of low-Prandtl number jets in mixed convection regime. In: Proceedings of the SESAME International Workshop. Petten, The Netherlands.

Fregni, A., Angeli, D., Cimarelli, A., Stalio, E., 2019c. Direct Numerical Simulation of three interacting low-Prandtl-number jets in mixed convection regime. In: Proceedings of the 37th UIT Heat Transfer Conference. Catania, Italy.

Gautier, R., Laizet, S., Lamballais, E., 2014. A DNS study of jet control with microjets using an immersed boundary method. International Journal of Computational Fluid Dynamics 28 (6-10), 393–410.

Gray, D. D., Giorgini, A., 1976. The validity of the Boussinesq approximation for liquids and gases. International Journal of Heat and Mass Transfer 19 (5), 545–551.

Grossmann, S., Lohse, D., 2000. Scaling in thermal convection: a unifying theory. Journal of Fluid Mechanics 407, 27–56.

Grossmann, S., Lohse, D., 2001. Thermal convection for large Prandtl numbers. Physical review letters 86 (15), 3316.

Grossmann, S., Lohse, D., 2002. Prandtl and Rayleigh number dependence of the Reynolds number in turbulent thermal convection. Physical Review E 66 (1), 016305.

Grossmann, S., Lohse, D., 2004. Fluctuations in turbulent Rayleigh–Bénard convection: the role of plumes. Physics of fluids 16 (12), 4462–4472.

Grötzbach, G., 1983. Spatial resolution requirements for direct numerical simulation of the Rayleigh-Bénard convection. Journal of computational physics 49 (2), 241–264.

Grötzbach, G., 2013. Challenges in low-Prandtl number heat transfer simulation and modelling. Nuclear engineering and design 264, 41–55.

Hartmann, D. L., Moy, L. A., Fu, Q., 2001. Tropical convection and the energy balance at the top of the atmosphere. Journal of Climate 14 (24), 4495–4511.

Hattori, T., Norris, S., Kirkpatrick, M., Armfield, S., 2013. Comparison of non-reflective boundary conditions for a free-rising turbulent axisymmetric plume. International Journal for Numerical Methods in Fluids 72 (12), 1307–1320.

Holmgren, M., 2006. X steam for matlab. `https://www.x-eng.com`. Accessed: 25-11-2019.

Jung, J. H., Yoo, G. J., 2004. Analysis of unsteady turbulent triple jet flow with temperature difference. Journal of Nuclear Science and Technology 41 (9), 931–942.

Kadanoff, L. P., 2001. Turbulent heat flow: structures and scaling. Physics today 54 (8), 34–39.

Kawamura, H., Abe, H., Matsuo, Y., 1999. DNS of turbulent heat transfer in channel flow with respect to Reynolds and Prandtl number effects. International Journal of Heat and Fluid Flow 20 (3), 196–207.

Kelley, D. H., Sadoway, D. R., 2014. Mixing in a liquid metal electrode. Physics of Fluids 26 (5), 057102.

Kimura, N., Igarashi, M., Kamide, H., 2002. Investigation on convective mixing of triple-jet-evaluation of turbulent quantities using particle image velocimetry and direct numerical simulation. In: Advances In Fluid Modeling And Turbulence Measurements. World Scientific, pp. 651–658.

Kimura, N., Miyakoshi, H., Kamide, H., 2007. Experimental investigation on transfer characteristics of temperature fluctuation from liquid sodium to wall in parallel triple-jet. International Journal of Heat and Mass Transfer 50 (9-10), 2024–2036.

Knebel, J., Krebs, L., Müller, U., Axcell, B., 1998. Experimental investigation of a confined heated sodium jet in a co-flow. Journal of Fluid Mechanics 368, 51–79.

Kolmogorov, A. N., 1941. The local structure of turbulence in incompressible viscous fluid for very large Reynolds numbers. Cr Acad. Sci. URSS 30, 301–305.

Krishnamurti, R., Howard, L. N., 1981. Large-scale flow generation in turbulent convection. Proceedings of the National Academy of Sciences 78 (4).

Kunnen, R., Clercx, H., Geurts, B., Van Bokhoven, L., Akkermans, R., Verzicco, R., 2008. Numerical and experimental investigation of structure-function scaling in turbulent Rayleigh-Bénard convection. Physical Review E 77 (1), 016302.

Laizet, S., Lamballais, E., 2009. High-order compact schemes for incompressible flows: a simple and efficient method with quasi-spectral accuracy. Journal of Computational Physics 228 (16), 5989–6015.

Laizet, S., Lardeau, S., Lamballais, E., 2010. Direct Numerical Simulation of a mixing layer downstream a thick splitter plate. Physics of Fluids 22 (1), 015104.

Laizet, S., Li, N., 2011. Incompact3d: a powerful tool to tackle turbulence problems with up to $\mathcal{O}(10^5)$ computational cores. International Journal for Numerical Methods in Fluids 67 (11), 1735–1757.

Lamballais, E., Silvestrini, J., Laizet, S., 2010. Direct Numerical Simulation of flow separation behind a rounded leading edge: study of curvature effects. International Journal of Heat and Fluid Flow 31 (3), 295–306.

Landau, L. D., Lifshitz, E. M., 1987. Fluid mechanics. Fluid Mechanics. Second Edition. 1987. Pergamon, Oxford.

Larson, R. L., 1991. Geological consequences of superplumes. Geology 19 (10), 963–966.

Lele, S. K., 1992. Compact finite difference schemes with spectral-like resolution. Journal of computational physics 103 (1), 16–42.

Lohse, D., Xia, K.-Q., 2010. Small-scale properties of turbulent Rayleigh-Bénard convection. Annual Review of Fluid Mechanics 42.

Marro, M., Salizzoni, P., Cierco, F.-X., Korsakissok, I., Danzi, E., Soulhac, L., 2014. Plume rise and spread in buoyant releases from elevated sources in the lower atmosphere. Environmental Fluid Mechanics 14 (1), 201–219.

Marshall, J., Schott, F., 1999. Open-ocean convection: Observations, theory, and models. Reviews of Geophysics 37 (1), 1–64.

Michel, E., Baglin, A., Auvergne, M., Catala, C., Samadi, R., Baudin, F., Appourchaux, T., Barban, C., Weiss, W. W., Berthomieu, G., et al., 2008. CoRoT measures solar-like oscillations and granulation in stars hotter than the Sun. Science 322 (5901), 558–560.

Moin, P., Mahesh, K., 1998. Direct numerical simulation: a tool in turbulence research. Annual review of fluid mechanics 30 (1), 539–578.

Moser, R. D., Kim, J., Mansour, N. N., 1999. Direct Numerical Simulation of turbulent channel flow up to Re= 590. Physics Fluids 11 (4), 943–945.

Niemela, J., Skrbek, L., Sreenivasan, K., Donnelly, R., 2001. The wind in confined thermal convection. Journal of Fluid Mechanics 449, 169–178.

Nishimura, M., Kimura, N., 2003. URANS computations for an oscillatory non-isothermal triple-jet using the k–ε and second moment closure turbulence models. International Journal for Numerical Methods in Fluids 43 (9), 1019–1044.

Nordlund, Å., Stein, R. F., Asplund, M., 2009. Solar surface convection. Living Reviews in Solar Physics 6 (1), 2.

Normand, C., Pomeau, Y., Velarde, M. G., 1977. Convective instability: a physicist's approach. Reviews of Modern Physics 49 (3), 581.

Oberbeck, A., 1879. Über die Wärmeleitung der Flüssigkeiten bei Berücksichtigung der Strömungen infolge von Temperaturdifferenzen. Annalen der Physik 243 (6), 271–292.

Obukhov, A., 1949. Temperature field structure in a turbulent flow. Izv. Acad. Nauk SSSR Ser. Geog. Geofiz 13, 58–69.

Obukhov, A., 1959. Effect of Archimedean forces on the structure of the temperature field in a turbulent flow. In: Dokl. Akad. Nauk SSSR. Vol. 125. pp. 1246–1248.

Ortiz, A. V., Koloszar, L., Planquart, P., 2019. Large Eddy Simulations on a natural convection boundary layer at Pr= 0.71 and 0.025. Nuclear Engineering and Design 353, 110231.

Otić, I., Grötzbach, G., Wörner, M., 2005. Analysis and modelling of the temperature variance equation in turbulent natural convection for low-Prandtl-number fluids. Journal of Fluid Mechanics 525, 237–261.

Pitz, D. B., Chew, J. W., Marxen, O., 2019. Effect of an axial throughflow on buoyancy-induced flow in a rotating cavity. International Journal of Heat and Fluid Flow 80, 108468.

Pope, S. B., 2001. Turbulent flows.

Sabato, M., Fregni, A., Stalio, E., Brusiani, F., Tranchero, M., Baritaud, T., 2019. Numerical study of submerged impinging jets for power electronics cooling. International Journal of Heat and Mass Transfer 141, 707–718.

Sani, R. L., Gresho, P. M., 1994. Résumé and remarks on the open boundary condition minisymposium. International Journal for Numerical Methods in Fluids 18 (10), 983–1008.

Scheel, J. D., Emran, M. S., Schumacher, J., 2013. Resolving the fine-scale structure in turbulent Rayleigh–Bénard convection. New Journal of Physics 15 (11), 113063.

Scheel, J. D., Schumacher, J., 2016. Global and local statistics in turbulent convection at low Prandtl numbers. Journal of Fluid Mechanics 802, 147–173.

Schulenberg, T., Stieglitz, R., 2010. Flow measurement techniques in heavy liquid metals. Nuclear Engineering and Design 240 (9), 2077–2087.

Schumacher, J., Götzfried, P., Scheel, J. D., 2015. Enhanced enstrophy generation for turbulent convection in low-Prandtl-number fluids. Proceedings of the National Academy of Sciences 112 (31), 9530–9535.

Shams, A., Roelofs, F., Niceno, B., Guo, W., Angeli, D., Stalio, E., Fregni, A., Duponcheel, M., Bartosiewicz, Y., Tiselj, I., et al., 2019a. Reference numerical database for turbulent flow and heat transfer in liquid metals. Nuclear Engineering and Design 353, 110274.

Shams, A., Roelofs, F., Tiselj, I., Oder, J., Bartosiewicz, Y., Duponcheel, M., Niceno, B., Guo, W., Stalio, E., Angeli, D., et al., 2019b. A collaborative effort towards the accurate prediction of flow and heat transfer in low-Prandtl fluids. In: 18th International Topical Meeting on Nuclear Reactor Thermal-Hydraulics, NURETH-18, Portland, Oregon, USA.

Shishkina, O., Stevens, R. J., Grossmann, S., Lohse, D., 2010. Boundary layer structure in turbulent thermal convection and its consequences for the required numerical resolution. New journal of Physics 12 (7), 075022.

Shraiman, B. I., Siggia, E. D., 1990. Heat transport in high-Rayleigh-number convection. Physical Review A 42 (6), 3650.

Siggia, E. D., 1994. High Rayleigh number convection. Annual review of fluid mechanics 26 (1), 137–168.

Sobolev, V., 2011. Database of thermophysical properties of liquid metal coolants for GEN-IV. Tech. Rep. BLG-1069, SCK-CEN, Belgium.

Stanley, S., Sarkar, S., Mellado, J., 2002. A study of the flow-field evolution and mixing in a planar turbulent jet using Direct Numerical Simulation. Journal of Fluid Mechanics 450, 377–407.

Stevens, D. P., 1990. On open boundary conditions for three dimensional primitive equation ocean circulation models. Geophysical & Astrophysical Fluid Dynamics 51 (1-4), 103–133.

Stevens, R. J., Verzicco, R., Lohse, D., 2010. Radial boundary layer structure and Nusselt number in Rayleigh–Bénard convection. Journal of fluid mechanics 643, 495–507.

Sun, C., Cheung, Y.-H., Xia, K.-Q., 2008. Experimental studies of the viscous boundary layer properties in turbulent rayleigh–bénard convection. Journal of Fluid Mechanics 605, 79–113.

Sun, C., Xia, K.-Q., Tong, P., 2005. Three-dimensional flow structures and dynamics of turbulent thermal convection in a cylindrical cell. Physical Review E 72 (2), 026302.

Sun, C., Zhou, Q., Xia, K.-Q., 2006. Cascades of velocity and temperature fluctuations in buoyancy-driven thermal turbulence. Physical review letters 97 (14), 144504.

Tennekes, H., Lumley, J. L., 1972. A first course in turbulence. MIT Press, Boston.

Togni, R., Cimarelli, A., De Angelis, E., 2015. Physical and scale-by-scale analysis of Rayleigh–Bénard convection. Journal of Fluid Mechanics 782, 380–404.

Tokuhiro, A., Kimura, N., 1999. An experimental investigation on thermal striping: Mixing phenomena of a vertical non-buoyant jet with two adjacent buoyant jets as measured by ultrasound doppler velocimetry. Nuclear Engineering and Design 188 (1), 49–73.

Tritton, D. J., 1988. Physical fluid dynamics. Oxford Science Publications.

van Reeuwijk, M., Jonker, H. J., Hanjalić, K., 2008a. Wind and boundary layers in Rayleigh-Bénard convection. I. Analysis and modeling. Physical Review E 77 (3), 036311.

van Reeuwijk, M., Jonker, H. J., Hanjalić, K., 2008b. Wind and boundary layers in Rayleigh-Bénard convection. II. Boundary layer character and scaling. Physical Review E 77 (3), 036312.

Verzicco, R., Camussi, R., 1999. Prandtl number effects in convective turbulence. Journal of Fluid Mechanics 383, 55–73.

Wang, Y., Zhao, F.-Y., Kuckelkorn, J., Liu, D., Liu, L.-Q., Pan, X.-C., 2014. Cooling energy efficiency and classroom air environment of a school building operated by the heat recovery air conditioning unit. Energy 64, 991–1001.

Wörner, M., Grötzbach, G., 1998. Pressure transport in Direct Numerical Simulations of turbulent natural convection in horizontal fluid layers. International journal of heat and fluid flow 19 (2), 150–158.

Xia, K.-Q., 2013. Current trends and future directions in turbulent thermal convection. Theoretical and Applied Mechanics Letters 3 (5), 052001.

Yu, Y., Merzari, E., Thomas, J. W., Obabko, A., Aithal, S., 2017. Steady and unsteady calculations on thermal striping phenomena in triple-parallel jet. Nuclear Engineering and Design 312, 429–437.

Zhou, Q., Sun, C., Xia, K.-Q., 2007. Morphological evolution of thermal plumes in turbulent Rayleigh-Bénard convection. Physical review letters 98 (7), 074501.